UNIVERSITY OF WEST ATTICA
SCHOOL OF ENGINEERING
DEPARTMENT OF MECHANICAL ENGINEERING

MODELLING AND QUANTIFICATION OF UNCERTAINTY IN NACA WING FLOWS

Danai Konstantatou
Registration number: 19392077
Supervisor: Dr. I. Sarris

Athens, 2024

ΠΑΝΕΠΙΣΤΗΜΙΟ ΔΥΤΙΚΗΣ ΑΤΤΙΚΗΣ
ΣΧΟΛΗ ΜΗΧΑΝΙΚΩΝ
ΤΜΗΜΑ ΜΗΧΑΝΟΛΟΓΩΝ ΜΗΧΑΝΙΚΩΝ

ΜΟΝΤΕΛΟΠΟΙΗΣΗ ΚΑΙ ΠΟΣΟΤΙΚΟΠΟΙΗΣΗ ΑΒΕΒΑΙΟΤΗΤΑΣ ΣΕ ΡΟΕΣ ΠΤΕΡΥΓΩΝ NACA

Δανάη Κωνσταντάτου
Αριθμός Μητρώου: 19392077
Επιβλέπων: Δρ. Ι. Σαρρής

Αθήνα, 2024

The Three-Member Examination Committee

The thesis was successfully examined by the following Examination Committee:

Name	Signature
Ioannis Sarris	Ioannis Sarris Digitally signed by Ioannis Sarris Date: 2024.10.04 23:30:02 +03'00'
Evangelos Karvelas	Evangelos Karvelas Digitally signed by Evangelos Karvelas Date: 2024.10.06 13:13:27 +03'00'
Georgios Sofiadis	GEORGIOS SOFIADIS Digitally signed by GEORGIOS SOFIADIS Date: 2024.10.06 11:33:15 +03'00'

ΔΗΛΩΣΗ ΣΥΓΓΡΑΦΕΑ ΠΤΥΧΙΑΚΗΣ ΕΡΓΑΣΙΑΣ

Η κάτωθι υπογεγραμμένη ΔΑΝΑΗ ΚΩΝΣΤΑΝΤΑΤΟΥ του ΠΑΝΑΓΙΩΤΗ, με αριθμό μητρώου 19392077 φοιτήτρια του Πανεπιστημίου Δυτικής Αττικής της Σχολής Μηχανικών του Τμήματος Μηχανολόγων Μηχανικών, δηλώνω υπεύθυνα ότι: «Είμαι συγγραφέας αυτής της πτυχιακής εργασίας και ότι κάθε βοήθεια την οποία είχα για την προετοιμασία της είναι πλήρως αναγνωρισμένη και αναφέρεται στην εργασία. Επίσης, οι όποιες πηγές από τις οποίες έκανα χρήση δεδομένων, ιδεών ή λέξεων, είτε ακριβώς είτε παραφρασμένες, αναφέρονται στο σύνολό τους, με πλήρη αναφορά στους συγγραφείς, τον εκδοτικό οίκο ή το περιοδικό, συμπεριλαμβανομένων και των πηγών που ενδεχομένως χρησιμοποιήθηκαν από το διαδίκτυο. Επίσης, βεβαιώνω ότι αυτή η εργασία έχει συγγραφεί από μένα αποκλειστικά και αποτελεί προϊόν πνευματικής ιδιοκτησίας τόσο δικής μου, όσο και του Ιδρύματος. Παράβαση της ανωτέρω ακαδημαϊκής μου ευθύνης αποτελεί ουσιώδη λόγο για την ανάκληση του πτυχίου μου».

Η Δηλούσα

Δανάη Κωνσταντάτου

Acnowledgments

This thesis was carried out at the University of West Attica, Department of Mechanical Engineering, in the year 2024.

The completion of my thesis would have been impossible without the valuable support of my professor and supervisor, professor at the University of West Attica, Dr. Ioannis Sarris. I would like to express my sincere thanks for the opportunity to work with him and the support he provided me with care and patience, not only during the writing of this thesis but also as my professor during my undergraduate studies.

I would also like to thank my fellow students and friends, who helped me both in practice and psychologically throughout our shared academic and personal journey.

Finally, I deeply thank my family, my mother, Nana, my brother, Christos-Andreas, and my chosen father, Dimitris. I thank them for the countless support they have offered me under adverse (or not) circumstances, and for the unconditional love they show me every day. I owe them my life and the opportunities that have come my way so far, and for that, I dedicate every success I have had to them.

Ευχαριστίες

Η παρούσα διπλωματική εργασία πραγματοποιήθηκε στο Πανεπιστήμιο Δυτικής Αττικής, στο τμήμα Μηχανολόγων Μηχανικών, το έτος 2024.

Η ολοκλήρωση της διπλωματικής μουυ εργασίας θα ήταν αδύνατη χωρίς την πολύτιμη υποστήριξη του καθηγητή μου και επιβλέποντα, καθηγητή στο Πανεπιστήμιο Δυτικής Αττικής, δρ. Ιωάννη Σαρρή. Θα ήθελα να εκφράσω ένα ειλικρινές ευχαριστώ για την ευκαιρία που μου προσέφερε να συνεργαστώ μαζί του και την στήριξη που μου παρείχε, με φροντίδα και υπομονή, όχι μόνο κατά την συγγραφή αυτής της διπλωματικής, αλλά και ως καθηγητής μου κατά την διάρκεια των πρωπτυχιακών μου σπουδών.

Επίσης, θα ήθελα να ευχαριστήσω τους συμφοιτητές και τους φίλους μου, που με βοήθησαν τόσο πρακτικά, όσο και ψυχολογικά καθ'όλη τη διάρκεια της ακαδημαϊκής και της κοινής προσωπικής μας πορείας.

Τέλος, ευχαριστώ βαθιά την οικογένεια μου, τη μητέρα μου, Νανά, τον αδερφό μου, Χρήστο-Ανδρέα, και τον πατέρα που με επέλεξε, Δημήτρη. Τους ευχαριστώ για την αμέτρητη συμπαράσταση που μου προσέφεραν υπό αντίξοες (ή και μη) συνθήκες, και για την ανιοδιοτελή αγάπη που μου δείχνουν καθημερινά. Τους οφείλω τη ζωή και τις ευκαιρίες που παρουσιάστηκαν στο δρόμο μου μέχρι σήμερα, και για αυτό τους αφιερώνω κάθε επιτυχία μου.

Abstract

In the field of aerospace engineering, the optimization of airfoil design plays a critical role in enhancing aircraft performance. This thesis proposes a novel algorithm for Uncertainty Quantification, which facilitates the solution of Navier - Stokes through an iterative process. UQ is carried out by employing Monte Carlo and Polynomial Chaos methods. This methodology aims to improve computational efficiency while accurately assessing the impact of various parameters, such as Reynolds number and airfoil camber, on aerodynamic characteristics.

The study emphasizes the UQ results, revealing how variations in Reynolds number and airfoil camber significantly influence aerodynamic characteristics. The findings highlight critical areas of uncertainty, particularly around the leading and trailing edges of the airfoil and the wake region, where variations in flow conditions introduce significant fluctuations.

While the research demonstrates the algorithm's effectiveness, limitations are acknowledged, particularly in handling unsteady flows and complex geometries, as well as the need for improvements in directly computing lift and drag forces. Future work may involve integrating the developed algorithm with machine learning models for design optimization and extending its capabilities to accommodate more intricate flow conditions.

Περίληψη

Στον τομέα της αεροδιαστημικής μηχανικής, η βελτιστοποίηση του σχεδιασμού της αεροτομής διαδραματίζει κρίσιμο ρόλο στην ενίσχυση των επιδόσεων των αεροσκαφών. Στην παρούσα διατριβή προτείνεται ένας νέος αλγόριθμος για την ποσοτικοποίηση της αβεβαιότητας, ο οποίος διευκολύνει την επίλυση των Navier - Stokes μέσω μιας επαναληπτικής διαδικασίας. Η UQ πραγματοποιείται με τη χρήση μεθόδων Monte Carlo και πολυωνυμικού χάους. Η μεθοδολογία αυτή αποσκοπεί στη βελτίωση της υπολογιστικής αποτελεσματικότητας, ενώ παράλληλα αξιολογεί με ακρίβεια την επίδραση διαφόρων παραμέτρων, όπως ο αριθμός Reynolds και η κύρτωση της αεροτομής, στα αεροδυναμικά χαρακτηριστικά.

Η μελέτη δίνει έμφαση στα αποτελέσματα της UQ, αποκαλύπτοντας πώς οι μεταβολές του αριθμού Reynolds και της κύρτωσης της αεροτομής επηρεάζουν σημαντικά τα αεροδυναμικά χαρακτηριστικά. Τα ευρήματα αναδεικνύουν κρίσιμες περιοχές αβεβαιότητας, ιδιαίτερα γύρω από τα μπροστινά και πίσω άκρα της αεροτομής και την περιοχή του απόνερα, όπου οι μεταβολές στις συνθήκες ροής εισάγουν σημαντικές διακυμάνσεις.

Αν και η έρευνα καταδεικνύει την αποτελεσματικότητα του αλγορίθμου, αναγνωρίζονται οι περιορισμοί, ιδίως στο χειρισμό ασταθών ροών και πολύπλοκων γεωμετριών, καθώς και η ανάγκη για βελτιώσεις στον άμεσο υπολογισμό των δυνάμεων άνωσης και αντίστασης. Η μελλοντική εργασία μπορεί να περιλαμβάνει την ενσωμάτωση του αλγορίθμου που αναπτύχθηκε με μοντέλα μηχανικής μάθησης για τη βελτιστοποίηση του σχεδιασμού και την επέκταση των δυνατοτήτων του για την αντιμετώπιση πιο περίπλοκων συνθηκών ροής.

Λέξεις - κλειδιά: Uncertainty Quantification, Aerodynamic Design, Navier-Stokes Equations, Reynolds Number, Airfoil Optimization

List of Figures

List of Tables

Contents

Chapter 1

Introduction

Within the fields of aerospace and aeronautical engineering, the continuous pursuit for optimal performance drives the refinement of aerodynamic structures. Airfoil design is a crucial element influencing aircraft performance. A well-designed airfoil significantly impacts the lift, drag, and overall aircraft efficiency [50], laying the groundwork for ongoing advancements and innovation in the industry.

The origins of aeronautical engineering can be traced back several centuries. There are examples of human experimentation with flight, from antiquity and mythology, notably the myth of Icarus [81]. An early approach to the design of flying machines was made by Leonardo da Vinci in the 1500s who, among others, he designed the ornithopter [50], [82]. A few centuries later, substantial progress in the science of aeronautics was made by the "father of aerial navigation", Sir George Cayley [39]. Cayley introduced several pioneering concepts for aircraft, including gliders, various types of airplanes, and even a primary helicopter. However, one of his fundamental works was the formulation of the four basic aerodynamic forces that affect flight: lift, weight, thrust, and drag. In the early 1900s, the first documented powered flight was achieved by the Wright brothers [30]. Following this pivotal accomplishment, the demand for efficient and safe aircraft for both military and civilian purposes drove researchers and manufacturers to develop new tools and methodologies for the study and design of such systems. It is also noteworthy to mention the significant advancements in wing design with the development of the NACA airfoil series (4-digit, 5-digit, 6-digit, etc.) in 1933. This type of airfoil was designed and named after the National Advisory Committee for Aeronautics (NACA). In order to simulate flight conditions more accurately, the committee conducted extensive testing in a variable-density wind tunnel for large Reynolds number values. Through this research, a technical report was published in 1933 containing 78 wings with different characteristics [51], and the generated data enabled researchers and manufacturers to choose the most appropriate wing for a given application and is used to this day.

Over time, the advancement of aeronautics has increasingly relied on computational methods [52]. Prior to 1960, the use of such methods was not common in aerodynamic studies. Instead, manual calculations and extensive wind tunnel testing were the norm. However, from 1960 onwards, researchers used digital computers for simple calculations and the analysis of individual aircraft components.

One of the most fundamental computational and modelling techniques is the Finite Element Method (FEM). The basic theory of FEM for structural analysis was published in 1943 by mathematician R. Courant [92], [29]. Nevertheless, the concept of finite elements was first described by M. J. Turner in 1953 as part of an internal research program at Boeing. From the mid-1960s to the early 1990s, FEM was rapidly developed and gradually became an indispensable tool for researchers and scientists [92], and in the following decades, its applications expanded in areas such as industrial application and material modelling [63]. Today, FEM is used for solving a variety of problems associated with structural, thermal, and fluid dynamics analysis, and can be implemented through software such as ANSYS[1].

One of the most common CFD problems that has captured the interest of researchers through the years, is Uncertainty Quantification (UQ). Initially neglected by researchers [56], the impact of uncertainty and randomness was eventually recognized after the end of the 19th century, and its study began to be included in the development of more robust and reliable models. In the early stages of uncertainty analysis, up until the late 20th century, probability theory played a central role. A notable contribution was made by Lotfi Zadeh, who introduced the theory of fuzzy sets in 1965 [107]. Another significant method is Polynomial Chaos Expansion, developed to mathematically characterize data and numerical errors consistently [37]. Finally, in the mid-20th century, one of the most widely adopted methods, the Monte Carlo simulation, was developed. The principal developers of the Monte Carlo method were

Stanislaw Ulam and John von Neumann. The method was conceived by Ulam, who based its fundamental theory on the principles of gambling.

The focus of the present Research is the uncertainties present in aerodynamic simulations. These uncertainties pose significant obstacles that must be managed to achieve robust design and optimization methodologies regarding airfoil structures. While extensive research has been conducted on the aerodynamics of NACA airfoils, this thesis proposes a new algorithm developed to calculate steady-state flows under uncertainty. This algorithm employs a Newton-type iterative method for solving the coupled Navier-Stokes equations describing the problem and aims to address the uncertainties in flow calculation by conducting faster and less computationally expensive simulations. The ultimate goal is to apply this knowledge to optimize aircraft design, resulting in more durable and efficient structures.

The thesis is organized as follows:

- Chapter 2: Theoretical Background
- Chapter 3: Methodology
- Chapter 4: Results
- Chapter 5: Discussion
- Chapter 6: Conclusions

Chapter 2

Theoretical Background

2.1 Basic aerodynamics principles

The science of aeronautical and aerospace engineering has not only impacted science and technology but also everyday life. The modernization of air transport, the development of geolocation systems, and space exploration are just a few examples of their importance to humanity. However, as the focus of this thesis lies in the optimization of airfoils, some theoretical background must be established, like the basic principles of aerodynamics, which allowed the design and construction of the various types of aircraft as we know them today.

2.1.1 Air properties

As this thesis focuses on aerospace applications, the fluid medium considered is atmospheric air. The air is characterized by properties such as mass, specific volume, density, viscosity, and temperature. The two most relevant ones for this study are density and viscosity.

- **Density (ρ)**: is defined as the fluid mass per unit volume, as indicated by its formula

$$\rho = \frac{m}{V} \tag{2.1}$$

- **Viscosity**: can be classified as,
  - **Dynamic viscosity (μ)**: the measure of its resistance to flow when an external force is applied [18]
  - **Kinematic viscosity (ν)**: the ratio of the dynamic viscosity to the fluid density

$$\nu = \frac{\mu}{\rho} \tag{2.2}$$

The following table (Table 2.1) shows the main properties of atmospheric air at 20°C, at sea level:

Quantity	Symbol	Value	Measurement Unit
Density	ρ	1.204	kg/m^3
Viscosity	μ	1.8×10^{-5}	$Pa \cdot s$

Table 2.1: Air properties

2.1.2 Aerodynamic forces

In J. Anderson's book, *Fundamentals of Aerodynamics* [17], the aerodynamic forces exerted on a body, e.g. a wing, are defined as the result of the pressure distribution and the shear stresses, acting vertically and tangentially on the surface, respectively. The shear stress is a result of the "pull" exerted on the

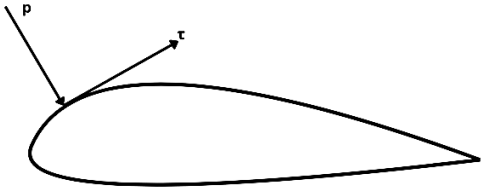

Figure 2.1: Pressure and shear stress on the surface of an airfoil [17]

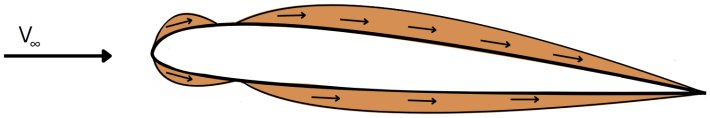

Figure 2.2: Shear stress distribution on airfoil surface [50]

surface of the airfoil due to the friction between the airfoil and the air stream. This force acts tangentially to the surface. Similarly, the pressure acts perpendicular to the surface, as indicated in Figure 2.1. The resulting shear stress distribution is shown in Figure 2.2.

Often used when studying the aerodynamic behavior of bodies, the *free-flow velocity*, denoted as V_∞, is considered as the air's velocity measured at an 'infinite' distance from the body, such that it is affected by neither the geometry of the body nor the boundaries of the domain.

The four fundamental aerodynamic forces developed are (Figure 2.3) [17], [49]:

1. **Thrust (T)**: The primary propulsive force responsible for the forward movement of a body, such as an aircraft.
2. **Drag (D)**: The resistive force that opposes thrust, thereby hindering the forward motion of the body.
3. **Lift (L)**: The force that enables the elevation of the body, contributing significantly to flight.
4. **Weight (W)**: The force resulting from the gravitational attraction of the Earth.

The aforementioned forces' values are set depending on the application. For example, during flight, the lift and thrust of the aircraft require overcoming the forces of weight and drag that are developed. Therefore, with proper aircraft design, the desired values of these forces can be achieved.

2.1.3 Dimensionless numbers

To study the 2D flow around a NACA airfoil, in addition to the basic aerodynamic forces, it is essential to understand several key dimensionless numbers. These numbers are crucial for analyzing and predicting the aerodynamic performance of the airfoil. The most important dimensionless numbers include:

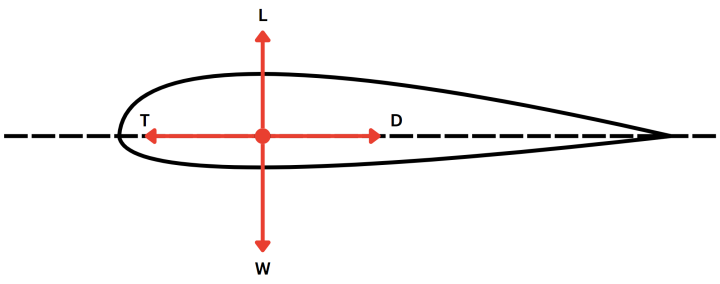

Figure 2.3: Aerodynamic forces on an airfoil

- The Reynolds number is defined as the inertia forces over the viscous forces. It provides a measure of comparison among the different types of flow. For low Reynolds numbers, the viscous forces dominate, resulting in a smooth and steady flow, known as laminar flow. On the other hand, as the Reynolds number increases, the inertia forces prevail, causing the flow to become turbulent. Viscous (or laminar) flows become turbulent after a 'threshold' Reynolds number value, named critical Reynolds number, $Re = Re_c$. Its value changes depending on the application, e.g. in pipeline flow applications, the critical Reynolds number has a value of $Re_c = 2000$.
  As previously stated, the Reynolds number is a key factor in determining the flow regime. Table 2.2 illustrates the various flow regimes based on the Reynolds number [88].

Reynolds number (critical)	$< 10^5$	$10^5 < Re < 10^6$	$> 10^6$
Flow regime	Laminar	Transition	Turbulent

Table 2.2: Flow regimes based on Reynolds number

Laminar flow is defined as a fluid motion in which the layers of the fluid move in a smooth and parallel manner, with minimal mixing between the layers. The transition flow regime, as indicated by its name, represents a transition from laminar to turbulent behavior. The flow gradually becomes less predictable, with intermittent turbulence and fluctuations. Last, on the turbulent flow regime, the fluid exhibits a high degree of unpredictability, with eddies varying in size superimposed upon the main flow. Turbulent flow is a complex process which is much more probable in practical applications than the laminar flow [58].

It is defined by the formula:

$$Re = \frac{\rho \cdot v \cdot L}{\mu} = \frac{v \cdot L}{\nu} \tag{2.3}$$

where: v: the velocity of the fluid relative to the object, L: a characteristic length (such as the diameter of a pipe or the chord length of an airfoil), μ: the dynamic viscosity of the fluid.

- **Mach number (Ma)**: The Mach number is the ratio of the velocity of a fluid to the velocity of sound in that fluid [11].

$$Ma = \frac{v}{v_s} \tag{2.4}$$

The speed of sound in air at 20°C is:

$$v_s = 343\,\mathrm{m/s}$$

The Mach number is a crucial concept in the study of fluid flows, as it allows us to distinguish between different types of flow regimes. Fluid flows can be distinguished according to their velocity as: *Subsonic*, *Transonic*, *Sonic*, *Supersonic*, *Hypersonic* and *Hypervelocity*. The Mach number values corresponding to the specific flow types are presented in the following table (Table 2.3) [59]:

Regime	**Subsonic**	**Transonic**	**Sonic**	**Supersonic**	**Hypersonic**	**Hypervelocity**
Mach	<0.8	0.8 - 1.2	1.0	1.2 - 5.0	5.0 - 10.0	>10.0

Table 2.3: Flow regimes categorized by Mach number at standard conditions

2.1.4 Boundary layer

The boundary layer is a crucial concept of fluid mechanics, which describes a small area between the bulk flow, characterized by the outer (or free-stream as mentioned above) velocity U_∞, and the solid wall. The thickness of the boundary layer is not constant, but it develops in the direction of the flow.

Figure 2.4 illustrates a well-known example of fluid flow over a horizontal plate. The fluid flows at a velocity of $u_\infty (= V_\infty)$. The surface of the plate is not smooth, consequently, it exhibits frictional forces when in contact with the mass of the fluid. This results in zero fluid velocity at the surface of the plate. However, as we move vertically away from the surface of the plate, the effect of the plate on the flow, namely the frictional forces, decreases, resulting in a gradual increase in velocity. Finally, the thickness of the boundary layer, δx, is formed at the point where the fluid velocity reaches $0.99 u_\infty$.

The boundary layer thickness can be computed by the following formula [70]:

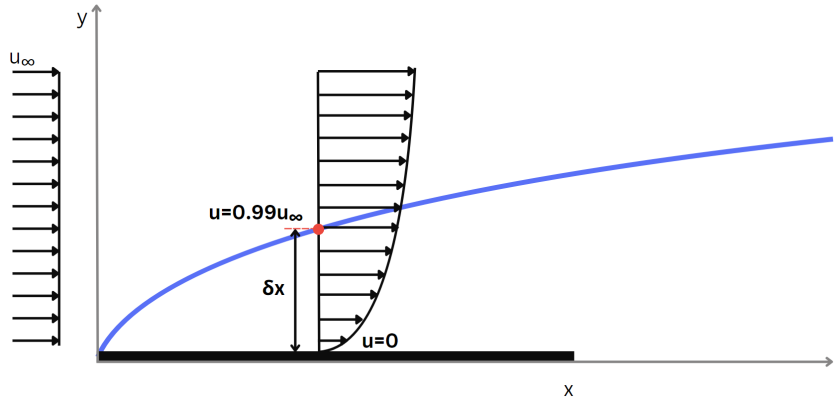

Figure 2.4: Boundary layer on flat plate

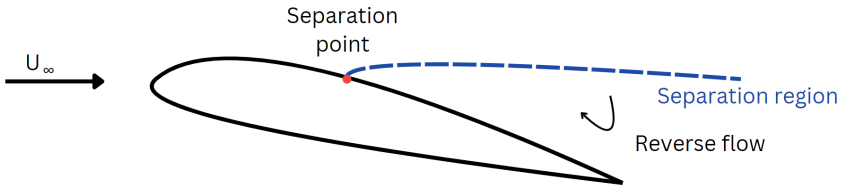

Figure 2.5: Visualisation of the flow separation [97]

$$\frac{\delta_{99}}{x} = \eta_{99} Re_x^{\frac{1}{2}} \tag{2.5}$$

where: Re is the Reynolds number and η_{99} is a constant with a value of 0.49 for equilibrium flows, and for non-equilibrium flows its value may vary up to 0.99.

2.1.5 Flow separation

A key factor affecting the performance of the airfoil is the *flow separation*. This phenomenon consists of the separation of the flow from the airfoil surface. It can be caused either by a severe adverse pressure gradient or by geometric deflection of the airfoil (increase in angle of attack). Flow separation initiates within the boundary layer when the shear stress in the wall reaches a zero value due to flow deceleration (White, 2009). This phenomenon results in the formation of an unstable region characterized by elevated turbulence levels and recirculation zones. Flow recirculations may potentially form instabilities such as *von Karman* and *Kelvin-Helmholtz* [97]. A schematic illustration of the separation phenomenon is provided in Figure 2.5.

It is widely acknowledged that separation is almost always associated with a decrease in lift, a drag increase, and pressure recovery losses. Furthermore, as discussed in the section on angle of attack, separation of the flow from the airfoil surface is the primary cause of the *stall* effect, which results in a significant reduction in lift and drag due to the dominance of the aircraft's weight. Factors such as lift and drag contribute to wing efficiency, and the occurrence of separation has a detrimental effect on it [41].

2.2 Fundamental Equations

The basic equations that govern the dynamics of fluids form the foundation upon which the study of the behavior of fluids under various conditions is based. These equations integrate fundamental principles such as the conservation of mass, flow, and energy. The application of these equations enables the prediction of flow patterns, pressure distributions, and velocity fields, thereby facilitating the optimization of the design, construction, and operation of aircraft and their components. The aforementioned equations

include the *Conservation of Mass*, *Momentum*, and *Energy*, as well as the *Navier Stokes Equations* [100].

2.2.1 Conservation of Mass, Energy and Momentum

Conservation of Mass

The conservation of mass describes that mass cannot be created or destroyed, i.e. that mass remains constant within a control volume. It is also known as the continuity equation. In summary, the time rate of change of mass in a control volume at a given time is equal to the net rate of mass flow in the control volume at that time [100].

The conservation of mass for a compressible fluid in three-dimensional Cartesian coordinates can be described by the following equation:

$$\frac{\partial \rho}{\partial t} + \frac{\partial (\rho u)}{\partial x} + \frac{\partial (\rho v)}{\partial y} + \frac{\partial (\rho w)}{\partial z} = 0 \implies \frac{\partial \rho}{\partial t} + \nabla \cdot (\rho \mathbf{u}) = 0 \tag{2.6}$$

The first term from the left side of the equation is the rate of change in time of the density (mass per unit volume), while the remaining three partial derivatives describe the pure mass flow out of the element through its boundaries, which is referred to as the *convection term*.

In the case of an incompressible fluid, which is of particular relevance to the present research, the density ρ is assumed to be constant. Consequently, equation 2.6 becomes:

$$\frac{\partial u}{\partial x} + \frac{\partial v}{\partial y} + \frac{\partial w}{\partial z} = 0 \implies \nabla \cdot (\mathbf{u}) = 0 \tag{2.7}$$

where: ρ is the fluid density, u is the velocity component in the x-direction, v is the velocity component in the y-direction, and w is the velocity component in the z-direction

Conservation of Momentum

Newton's second law of motion concerns the momentum of a body. Specifically, it states that the component of the forces applied to a body is equal to the rate of change of the body's momentum. Conservation of momentum, therefore, means that the momentum of a system remains constant, it is not created or destroyed.

The conservation of form equation in three dimensions is given by the following three equations:

- **x-component**:

$$\frac{\partial (\rho u)}{\partial t} + \frac{\partial (\rho u u)}{\partial x} + \frac{\partial (\rho u v)}{\partial y} + \frac{\partial (\rho u w)}{\partial z} = \frac{\partial \sigma_{xx}}{\partial x} + \frac{\partial \sigma_{xy}}{\partial y} + \frac{\partial \sigma_{xz}}{\partial z} + \rho f_x \tag{2.8}$$

  where: σ_{xx}, σ_{xy}, and σ_{xz} are the components of the stress tensor, and f_x is the body force per unit mass in the x-direction.

- **y-component**:

$$\frac{\partial (\rho v)}{\partial t} + \frac{\partial (\rho v u)}{\partial x} + \frac{\partial (\rho v v)}{\partial y} + \frac{\partial (\rho v w)}{\partial z} = \frac{\partial \sigma_{yx}}{\partial x} + \frac{\partial \sigma_{yy}}{\partial y} + \frac{\partial \sigma_{yz}}{\partial z} + \rho f_y \tag{2.9}$$

  where: σ_{yx}, σ_{yy}, and σ_{yz} are the components of the stress tensor, and f_y is the body force per unit mass in the y-direction.

- **z-component**:

$$\frac{\partial (\rho w)}{\partial t} + \frac{\partial (\rho w u)}{\partial x} + \frac{\partial (\rho w v)}{\partial y} + \frac{\partial (\rho w w)}{\partial z} = \frac{\partial \sigma_{zx}}{\partial x} + \frac{\partial \sigma_{zy}}{\partial y} + \frac{\partial \sigma_{zz}}{\partial z} + \rho f_z \tag{2.10}$$

  where: σ_{zx}, σ_{zy}, and σ_{zz} are the components of the stress tensor, and f_z is the body force per unit mass in the z-direction.

Conservation of Energy

The energy equation is derived from the 1st thermodynamic law which expresses the conservation of energy within a system. It is described by the general equation [23]:

$$\frac{\partial(\rho C_p T)}{\partial t} + (\vec{U} \cdot \nabla)(\rho C_p T) = \dot{T}_G + [\nabla \cdot \alpha \nabla(\rho C_p T)] - (\rho C_p T)(\nabla \cdot \vec{U}) \tag{2.11}$$

and for an incompressible medium, in Cartesian coordinates:

$$\frac{\partial T}{\partial t} + U_x \frac{\partial T}{\partial x} + U_y \frac{\partial T}{\partial y} + U_z \frac{\partial T}{\partial z} = \frac{\dot{T}_G}{\rho C_p} + \left[\frac{\partial}{\partial x}\left(\alpha \frac{\partial T}{\partial x}\right) + \frac{\partial}{\partial y}\left(\alpha \frac{\partial T}{\partial y}\right) + \frac{\partial}{\partial z}\left(\alpha \frac{\partial T}{\partial z}\right) \right] \tag{2.12}$$

where: C_p is the specific heat capacity at constant pressure, T is the temperature, U_x, U_y, U_z are the components of the velocity vector $\vec{U}$ in the x, y, z directions respectively, $\dot{T}_G$ is the volumetric heat source term, α is the thermal diffusivity.

2.2.2 Navier-Stokes Equations

The Navier-Stokes equations are a system of partial differential equations that play a crucial role in the study of fluid flows. They were first conceptualized by Claude-Louis Navier and further developed by George Gabriel Stokes. These equations are based on three important physical principles [**?**] [48]:

1. **Newton's law of viscosity:**
   It defines the relationship between the shear stress and the shear rate in a fluid subjected to mechanical stress, as shown in the following equation [35]:

$$\frac{\text{Shear stress}}{\text{Shear rate}} = \text{constant} = \text{viscosity or coefficient of viscosity} \tag{2.13}$$

2. **The conservation of mass** (see Eqs. 2.8 through 2.10)

3. **Newton's second law:**
   It defines the relationship between force, mass, and acceleration, expressed as:

$$\text{Force} = \text{mass} \times \text{acceleration} \tag{2.14}$$

In this manner, the Navier-Stokes equations are defined in a region Ω, for $0 < t \leq T$ as follows:

$$\rho\left(\frac{\partial \mathbf{u}}{\partial t} + \mathbf{u} \cdot \nabla \mathbf{u}\right) - \mu \Delta \mathbf{u} + \nabla p = \mathbf{f} \tag{2.15}$$

$$\nabla \cdot \mathbf{u} = 0 \tag{2.16}$$

2.3 Airfoils

2.3.1 Definition of an airfoil

The airfoil is arguably the most crucial component of an aircraft, as it serves as the primary source of lift and thrust. The airfoil has a significant effect on the cruising speed, takeoff, landing distances, stalling speed, handling qualities (particularly in proximity to the stall), and overall aerodynamic efficiency throughout the entirety of the flight. An airfoil constitutes the shape of a wing, designed specifically to generate an aerodynamic force containing both drag and lift as it traverses through a fluid medium [84], or as per John D. Anderson's definition in *Basic Principles of Aerodynamics*, an airfoil refers to any cross-section of the wing in a plane parallel to the xz plane if we assume that the wing span extends along the y-axis. A more detailed comprehension of this definition can be obtained from Figure 2.6.

Airfoils are used in a variety of applications, including aeronautics, the automotive industry, and energy applications such as the construction of wind turbine blades. The specific application of an airfoil is determined by its shape and geometric design characteristics.

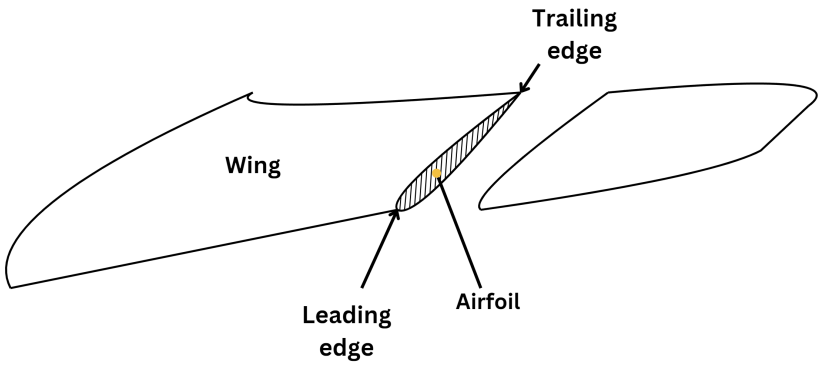

Figure 2.6: Airfoil section [84]

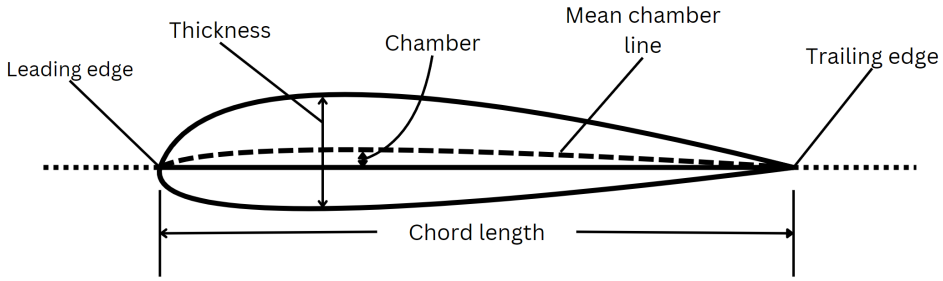

Figure 2.7: Characteristics of airfoil [19]

2.3.2 Airfoil geometry

Basic geometric characteristics

All airfoils, regardless of their specific type, are characterized a set of common geometric parameters. Figure 2.7 illustrates the most important geometrical dimensions of an airfoil.

- The **mean camber line** which represents the average distance between the upper and lower surface,
- The extreme points at the front and rear of the airfoil, the **leading edge** and **trailing edge**, respectively,
- The characteristic length of the airfoil or otherwise **chord** (c), which is the line joining the leading and trailing edge,
- The **camber** (m), i.e. the maximum distance between the mean camber line and the chord, measured perpendicular to the chord, and
- The **thickness** (t) of an airfoil, which is the distance between its upper and lower surfaces, measured perpendicular to the chord.

Furthermore, in the context of three-dimensional wings, there is another geometrical component, the wing's *span* (b or s). However, the span is a parameter that will not be considered in this thesis, as it is not applicable to two-dimensional airfoils.

Angle of attack

Another important variable for the study of the flow around airfoils is the *angle of attack*, denoted as α, which is the angle between the wind velocity vector representing the relative motion between the aircraft and the atmosphere and the chord line [67], as depicted in Figure 2.8 [17]. The angle of attack affects significantly the generation of the lift on the airfoil. As illustrated in Figure 2.9, there is a nearly linear

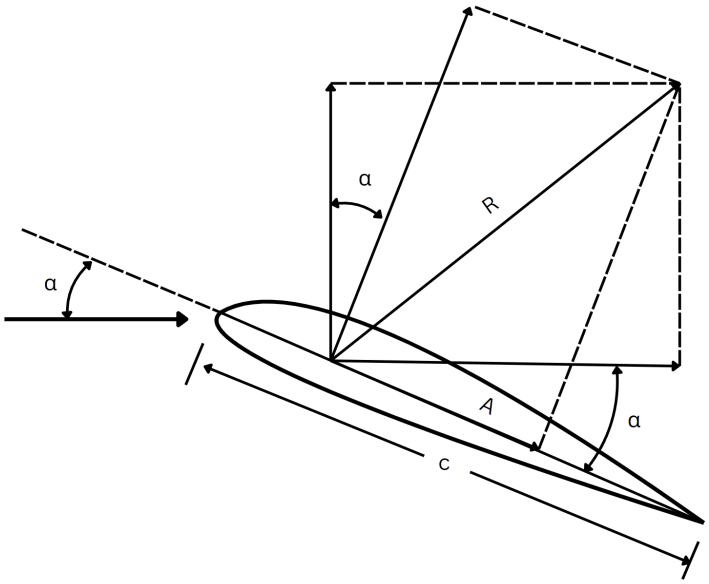

Figure 2.8: Graphical representation of the angle of attack versus the forces exerted on the airfoil surface

increase in lift as the angle of attack increases. However, at high values of attack, as depicted in Figure 2.9, the generation of the lift ceases abruptly. That point is referred to as *stall*, and in such conditions, the boundary layer separates from the airfoil's surface [93].

The *stall angle*, i.e. the angle of attack at which stall occurs may vary, but a good approximation is considered to be around $8° - 10°$. Figure 2.10 depicts the summary of the lift characteristics of NACA64A006, a thin airfoil computed by numerous RANS models.

Center of pressure and aerodynamic center

As previously stated in Section 2.1.2, when fluid flows around a body, such as air, a pressure field is created which produces a force and moment. The *center of pressure* is defined as the point where the magnitude of the said moment is equal to zero [87].

The direction in which the airfoil rotates depends on the position of the center of pressure. With that said, clockwise and counterclockwise rotation occurs, respectively, in the positive and negative pressure zones (see Figure 2.11).

Consequently, the center of pressure is the point situated on the chord line (between the leading and trailing edge), which cannot be rotated. As the center of pressure is dependent on the pressure distribution along the airfoil, it varies with the angle of attack.

Finally, the *aerodynamic center* of an airfoil can be defined as the point on the chord line where the pitching moment coefficient remains constant with changes in the angle of attack [87]. It is assumed that the aerodynamic forces are only applied at this point, thus simplifying the analysis. In the case of symmetric airfoils, according to the *thin airfoil theory* [54], the aerodynamic center is typically at 25% of the chord length from the leading edge. However, in the case of cambered airfoils, this position may vary slightly. Nevertheless, in most cases, it is presumed to be fixed at the 25% chord position.

2.3.3 Aerodynamic behavior of airfoils

The aerodynamic behavior of an airfoil depends on several key factors, each playing a critical role in the generation of lift and drag. Some of them are the geometry of the airfoil, the angle of attack, the smoothness of the surface, and the flow characteristics.

The geometry of an airfoil depends on several factors. One of them is the *thickness ratio*, an important parameter for the generation of lift and drag. Increased maximum thickness results in enhanced maximum lift and lift-to-drag ratio. However, there is a threshold, beyond which, drag is significantly increased due to potential laminar separation. Furthermore, increasing the thickness ratio typically improves aerodynamic performance by increasing maximum lift, zero lift angle of attack, lift/drag ratio, and pitching moment, while simultaneously decreasing drag [14].

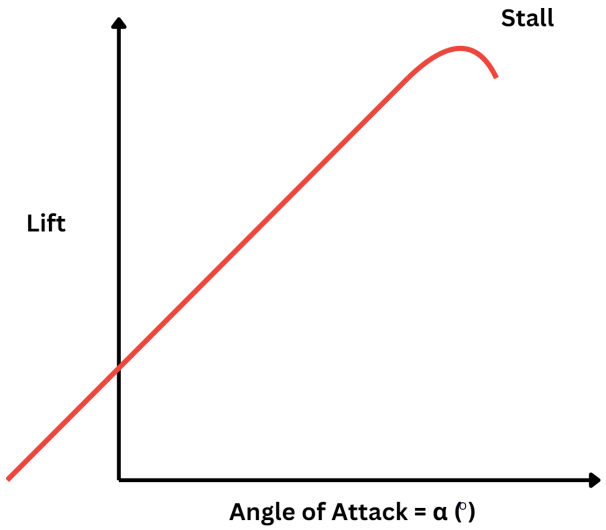

Figure 2.9: Variation of lift as a function of angle of attack [93]

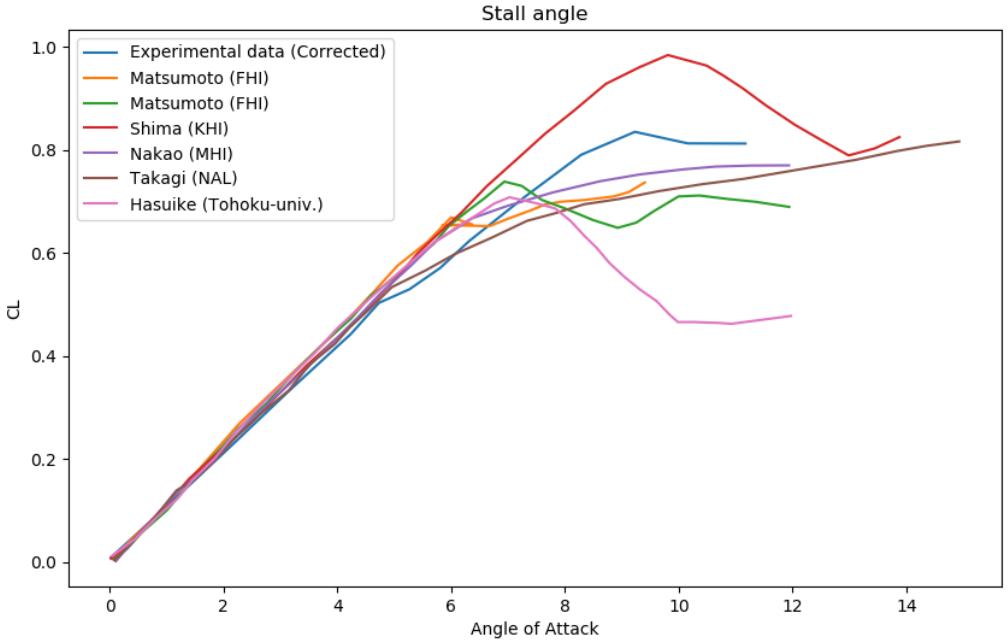

Figure 2.10: Stall angles[57]

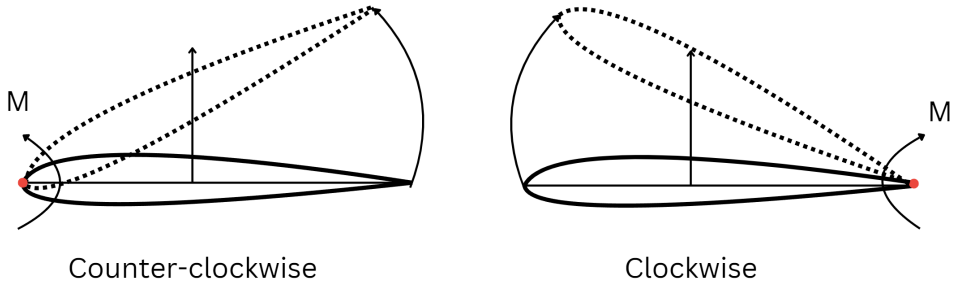

Figure 2.11: Rotation of airfoil according to the location of the center of pressure [87]

As previously stated in Sub-Section 2.3.2, the angle of attack influences the aerodynamic performance of an airfoil, by causing variations in velocity and pressure along the upper and lower surfaces of the airfoil. The difference in pressure values results in the generation of lift force, until a point where the airfoil stalls and the lift force is suddenly decreased. The *stall point* indicates the optimal angle of attack, on which maximum lift is achieved before the stalling phenomenon occurs. This point has been computed to correspond to approximately $a = 10°$ [13].

Another parameter that impacts lift and drag characteristics, as well as stall attributes, is *surface roughness*. Specifically, the surface roughness not only influences flow transition, but also boundary layer separation, resulting in increased drag, and a delay in stall separation [106].

Finally, the flow characteristics are considered a critical parameter affecting the airfoil's overall aerodynamic behavior. As previously stated, the type of flow (laminar to turbulent) is determined by calculating the Reynolds number. A higher Reynolds number indicates a more turbulent flow, which means higher drag, and a delay of flow separation from the airfoil surface [25].

2.4 NACA airfoils

The NACA airfoil series was developed by the *Langley Research Center* of the *National Advisory Committee for Aeronautics* in 1929 [12], following a comprehensive investigation of a family of airfoils within the Langley variable-density tunnel. The NACA airfoils are defined by a set of mathematical equations that describe their shape. According to the specific characteristics of each type, such as thickness, camber, and the position of maximum thickness and maximum camber, they are assigned a sequence of digits that distinguishes them. The resulting airfoil profiles that were presented in a technical report by NACA in 1933 [51], represent a benchmark in the design, analysis, and optimization of aircraft wings, propellers, and other similar aerodynamic structures. In this section, the fundamental design characteristics and underlying theory of NACA airfoils are explored in detail.

2.4.1 The 4-digit NACA airfoil

The design of NACA airfoils was based on an extensive methodology with the objective of optimizing the aerodynamic performance. The shape and geometrical characteristics of NACA airfoils are determined by a series of mathematical equations. Through these equations specify key parameters including thickness, camber, and their respective positions along the chord.

However, two are the critical parameters identified in the aforementioned NACA report: the thickness form, and the shape of the mean line, which determine the airfoil's shape and impact its aerodynamic characteristics.

The Commission studied and recorded the various types of airfoils, while also assigning names to them. Thus, the first type of NACA airfoil was the *4 - digit NACA airfoil*, denoted by the code NACA xxxx, which will also be the main focus of this thesis. By understanding the meaning of each digit separately researchers and manufacturers are able to select the appropriate airfoil for their specific needs.

For example, a NACA 2315 has:

- Maximum camber of 2 % of the chord

- At a position of 0.3 of the chord from the leading edge
- Maximum thickness of 15 % of the chord

Note that symmetrical airfoils are denoted as NACA 00xx.

The specific characteristics of the NACA airfoils which determine their shape can be calculated by a set of certain equations and assumptions established by the Committee, which will be presented in Section 3.3.1 of the *Methodology* chapter.

2.5 Computational Fluid Dynamics

2.5.1 The Finite Element Method

The Finite Element Method (FEM) is a powerful numerical technique widely used by engineers and scientists to solve partial differential equations (PDEs) in complex systems [31]. It offers flexibility and efficiency in approximating the solutions of differential equations when their analytical computation is difficult [40].

FEM represents a continuous geometry as a set of discrete shapes called *finite elements*, which are connected by points called *nodes*. These points are situated at the boundaries of the elements and are the site of any interaction with neighboring elements. Furthermore, at the nodes, the values of the field variables are known, although the variation in the continuous field is not known due to its complexity. Therefore, through the nodes and simple functions called *interpolation models*, the specific variation is approximated. The resulting system of equations (*field equations*), which is in the form of matrix equations, is solved for the values at the nodes, providing the final approximate solutions to the entirety of elements.

General Description of the Method

Solving any continuous problem using the finite element method always involves following a clear, step-by-step process, which can be described as follows [80] [101] [43] [65]:

Step 1: Discretization and Element Type Selection

In the initial step of the Finite Element Method, the computational domain is divided into discrete, non-overlapping sub-regions, called *elements*. The solution is calculated at points situated at the vertices of each element, within them, or on their edges. These points are called *nodes*.

There are various types of elements, shown in Figure 2.12. The choice of the appropriate element type depends on the specific requirements of the problem. One crucial parameter is the size of the elements. The use of smaller elements is often preferred, as it enhances the accuracy of the solution. However, this approach increases the computational approach. Therefore, it is necessary to take into consideration both the accuracy of the results and the computational resources available. Additionally, the element shape must be determined at this stage as it affects the solution of the problem. For example, for one-dimensional problems consisting of a curve, the elements are in the form of straight segments that form the original curve. Similarly, for two-dimensional arrays, the elements are triangular or quadrilateral, and as the complexity of the array increases in three dimensions, the shapes become more complex. So tetrahedra, triangular prisms, or orthogonal bricks are chosen to represent three-dimensional structures.

Step 2: Interpolation Functions

Once the field has been discretized, the finite elements and their nodes have been formed. Knowing the form of the unknown function governing the problem, it is calculated at the nodes. Therefore, for each of the elements, so-called interpolation functions are defined using the node values, which have the form of a polynomial. The interpolation functions are also called shape functions.

In nonlinear CFD problems, particularly when using iterative methods like Newton-Raphson, a linear system of equations is defined. Specifically, starting from an initial guess u_0 one iteration step of the Newton-Raphson scheme is given by:

$$\frac{\partial F(u^k)}{\partial u} \cdot 1u^{k+1} = -F(u^k) \tag{2.17}$$

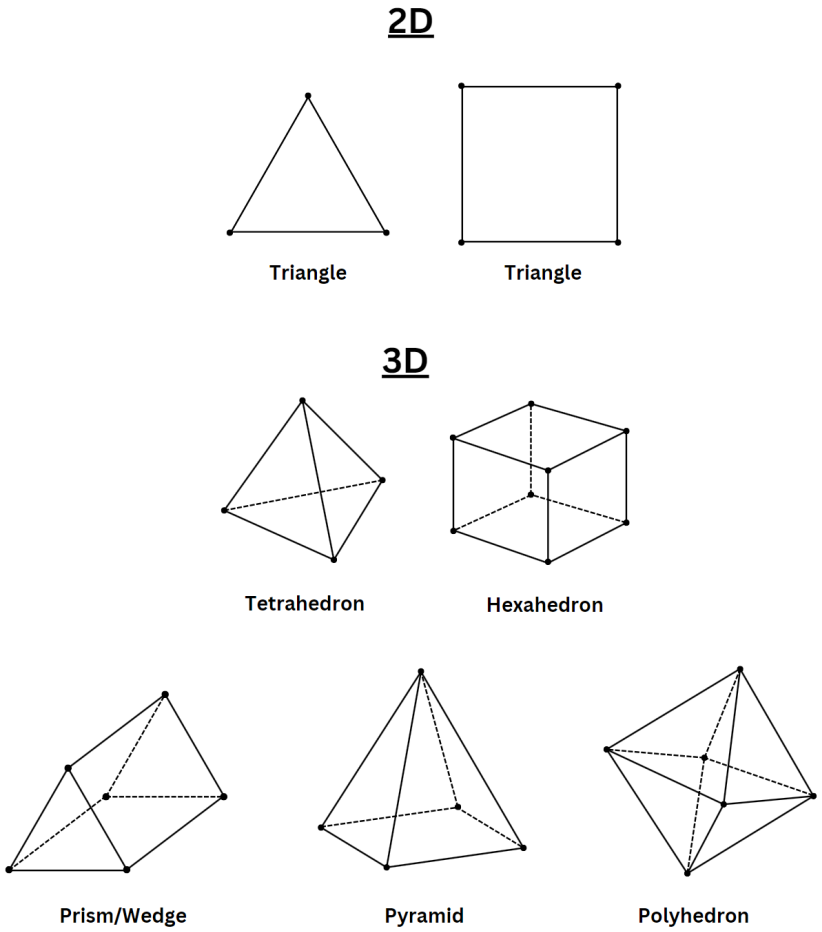

Figure 2.12: Different types of mesh cells [2]

where u is a vector of unknown values, and the nonlinear system equations for u given by:

$$F(u) = 0 \tag{2.18}$$

A popular approach for the solution of said equation systems is the use of a Jacobian matrix $\frac{\partial F(u^k)}{\partial u}$ [110].

Step 3: Governing Equations and Boundary Conditions

The governing equations are related to the physics of the problem to be solved. As discussed in subsection 2.2, these equations are the *continuity*, *momentum*, and *energy* equations [16]. These equations are integrated over each element, by converting their strong form into their weak form using methods like the Galerkin method. Consequently, the shape functions are applied. At this stage, essential boundary conditions describing the physical problem should be enforced.

Step 4: Global System of Equations and Solution

The equations and boundary conditions resulting from the previous step of the methodology are assembled into a system in which the problem as a whole is included [6]. This system is then solved using straightforward or iterative approaches.

It should be noted that FEM is applied to the convection part of the transport equations. This causes stabilization problems, which is addressed by applying stabilization techniques such as Streamline Upwinding Petrov-Galerkin (SUPG), and Taylor-Galerkin (TG) [78] [27].

The final step in the FEM process is post-processing and analysis of the results. Once primary variables such as velocity and pressure are determined, derived quantities such as vorticity, streamlines, or heat flux can be calculated. Additionally, post-processing tools are used to visualize the flow field, to better understand the flow behavior, and to verify the accuracy of the solution.

Advantages and Disadvantages

The finite element method offers a number of advantages and disadvantages when employed in the study of fluid mechanics systems. These are presented in Table 2.4

Advantages	Disadvantages
Modelling of complex geometries	The construction of an appropriate mesh, especially for complex geometries, is challenging. The quality of the mesh affects the accuracy of the solution.
Adaptability and reduced computational costs as designers can quickly model different designs and materials, saving time and money	Detailed parameter tuning is required to achieve convergence, which can be time-consuming.
High accuracy, especially in denser meshes with larger numbers of elements	Despite its accuracy, as the method assumes linear behavior within cells, the presence of error, especially in more sophisticated nonlinear problems, must be taken into account.
Useful for time-dependent simulations, where deformations in one region depend on changes in other regions	The choice of the appropriate data type affects the accuracy. Poorly shaped elements can introduce errors.
Easy boundary condition integration	While efficient for simpler one- and two-dimensional problems, the method can be computationally expensive for complex three-dimensional geometries.

Table 2.4: Advantages and Disadvantages of the Finite Element Method

2.5.2 CFD meshing

In the previous subsection the basic principles of the Finite Element Method were discussed, including discretization. Based on this concept, the numerical solution of complex problems is approached within the context of CFD through the process of discretization, whereby the computational domain of interest

into elements or cells. The discrete collection of elements is referred to as *mesh*. The process of generating the mesh is called "meshing" and its purpose is to simplify the resolution of the partial differential equations that govern the behavior of fluids in CFD simulations.

Types of meshes

In general, meshes can be classified into two main categories: structured and unstructured. Each type has its own distinct characteristics, advantages, and challenges and their use depends on the complexity of the flow problem in question. [100]

In a *structured* mesh, points are positioned at the junctions of coordinate lines. Furthermore, the number of neighboring mesh points for internal mesh points is fixed. A structured mesh is characterized by its ability to be represented in an $I \times J$ matrix of tetrahedra for two-dimensional geometries or an $I \times J \times K$ matrix of hexahedra for three-dimensional geometries. As their use can be applicable to simpler shapes, the visualization of the geometries examined can become challenging as their complexity increases. In this instance, the computational domain is divided into subdomains containing structured mesh, which facilitates denser meshing in areas that require enhanced resolution.

In an *unstructured* mesh, each cell is treated as a building block. The "unstructured" characterization refers to meshes in which no particular cell shape is used. In the majority of cases, combinations of triangular and quadrilateral elements are employed for two-dimensional flow calculations, whereas tetrahedral and hexahedral elements are used in three-dimensional flows. One advantage of an unstructured mesh is that it can be used to analyze more complex geometric shapes while maintaining a low computational cost for mesh generation. Additionally, automated techniques have been developed and used in industry to facilitate the generation of unstructured meshes. Finally, mesh density can be increased for more detailed analysis in specific regions is more in a more straightforward way with unstructured meshes compared to structured meshes.

Meshing parameters

In the process of generating a mesh, there are two fundamental properties to consider [26]:

1. **Mesh density**: how fine or coarse a mesh will highly depend on the accuracy requirements of the domain or geometry under consideration. For example, regions exhibiting greater velocity gradients, or are situated in proximity to geometry or boundary layer surfaces typically necessitate the use of a more refined mesh to effectively capture the more intense floe phenomena occurring therein.

2. **Mesh geometry**: as mentioned above, some of the cell shapes that can be used depending on the dimensions of the domain are: triangles, tetrahedra, hexahedra etc.

2.5.3 Meshing techniques

There are multiple methods for the generation of the mesh. The main ones are as follows [91]:

- **Automatic meshing**:As the name suggests, automatic meshing enables the user to create the mesh and its components (elements connected by nodes) in an automated manner. This kind of method can be appealing to users who may not have experience with modelling and CFD simulations, as it offers a way of conducting accurate mathematical modelling, without requiring deep knowledge of such simulations. Automated methods are also employed for industrial applications because they help conserve time and effort and allow a shift in focus toward innovation and design improvement. However, a significant disadvantage of automatic meshing is the fact that it lacks complete control over the mesh configuration, as certain parameters can only be defined through manual approaches.

- **Manual meshing**: In this approach, the user discretizes the computational domain rather than automatically by a software algorithm. In contrast to automatic meshing, the manual mesh offers the user complete control of the mesh generation process, enabling real-time adjustments that align with the simulation requirements. However, the manual mesh configuration is dependent on user input, thus it is susceptible to human error. Additionally, modelling with manual meshes can be time-consuming and overly complicated for inexperienced users. Consequently, achieving high accuracy of simulation results requires expertise.

2.6 Uncertainty Quantification

This thesis examines the problem of Uncertainty Quantification (UQ), with a particular focus on two-dimensional NACA airfoils. As outlined by Ghanem in his book *Handbook of Uncertainty Quantification* [36], *"Uncertainty quantification is the rational process by which proximity between predictions and observations is characterized. It can be thought of as the task of determining appropriate uncertainties associated with model-based predictions.*

UQ is used for the optimization of the design and control of NACA aifoils. It helps account for uncertainties in airfoil geometry, operating conditions, and material properties. This allows for adjustments to airfoil parameters to improve performance. UQ also plays a key role in validating numerical models through comparison of simulation results with experimental data.

2.6.1 Types of Uncertainty

The term "uncertainty" refers to situations where important information about the requisite data, like their quantity, type, or distribution are unknown, or insufficient. Uncertainty can be encountered throughout the simulation process, from the generation to the evaluation of the data.

When it comes to uncertainty, there are two principal categories associated with data: *aleatoric* and *epistemic* [76].

Aleatoric uncertainty is also known as *irreducible uncertainty* [98] because of its objective character [61]. This means that such uncertainties cannot be contained, as they are linked to the physical variability of a system, such as changes in material properties, manufacturing tolerances, and so forth. They are handled through variable modelling, as well as the use of probabilistic approaches.

Epistemic uncertainty can also be found as *ignorance uncertainty* [83] and it is more subjective [61], as it is a result of the lack of familiarity with the physical model under study. Such discrepancies are attributed to assumptions or simplifications made while formulating the physical problem and can be reduced by obtaining additional data regarding the physical model.

In the context of the study of airfoils, the uncertainties that arise can also be of a *geometric* and *operational* nature [69].

Geometric uncertainties arise because of small differences in the shape of the airfoil caused by manufacturing limits or unexpected changes the geometry has undergone during operation, like bending or deformation. For example, the structure may be deformed under loading. However, it is possible to consider that the geometric uncertainty is associated with the variation of airfoil shape parameters, such as thickness, maximum camber, or even the radius of the leading edge [64].

Similarly, operational uncertainties are associated with the flow and operational conditions of the airfoil. Such uncertainties may relate to Mach number, Reynolds number, or angle of attack. Modifications to these parameters have the potential to influence the performance and stability of the airfoil [90].

In conclusion, it is clear that both geometric and operational uncertainties affect the performace of the airfoils. By addressing them, the reliability of the airfoil's design is improved, making it possible for researchers to create more accurate models of airfoil behavior.

2.6.2 Theoretical Framework

Depicted in figure 2.13 [108], are the main components of the UQ process. Following the experimental design, the characterization of the input parameters is one of the initial steps of the *forward UQ*. This process includes the *sensitivity analysis* (global or local), or the *uncertainty propagation*.

It is possible that the input uncertainties may not be available at the time of the research, which could result in the "lack of input uncertainty information" issue. In such instances, the *backward* or *inverse UQ* process [74] [96] is employed, including *model calibration* and *Bayesian Inference*. The inverse process is based on comparisons between computations and experiments, in order to reduce output uncertainty [74].

Simulation-based uncertainty quantification is a common method, but it has significant disadvantages such as slow convergence rates, especially in applications with a high computational cost of each sample [103]. A decreased number of samples can be achieved by the method of *experimental design* while ensuring the same effect of full factorial design [79]. An alternative approach to handling computationally expensive simulations is the *surrogate model* or *response surface method* [103]. With this approach, an approximate functional model mapping $\hat{\mathscr{M}}$ is provided, in place of the true mapping $\mathscr{M}$.

Furthermore, the model uncertainty is a parameter that requires attention. In general, it is crucial to account for the inherent uncertainty due to the geometrical characteristics of the model, the numerical

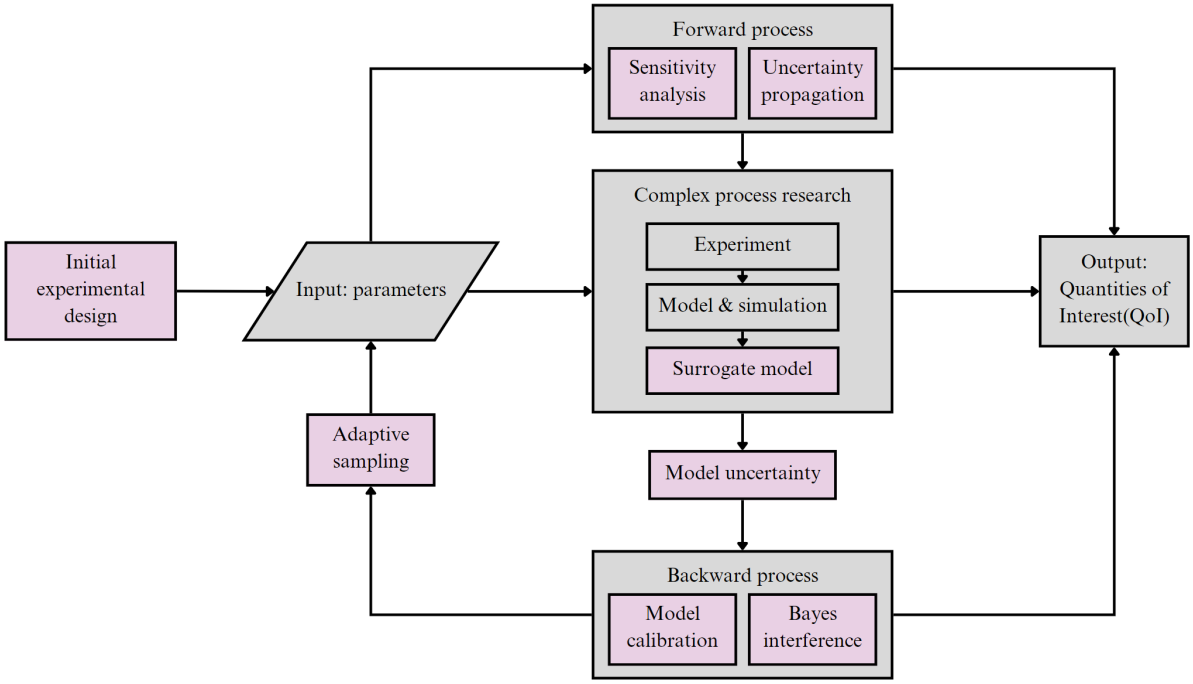

Figure 2.13: The framework and main process of UQ (pink boxes) [108]

methods employed, and the parameters involved. Techniques such as model averaging, model selection, and parameter optimization assist in managing this uncertainty, thereby leading to more reliable predictions.

2.6.3 UQ Methods

Uncertainty Quantification (UQ) is a process of quantifying uncertainties related to the calculation of Quantities Of Interest (QOIs), with the aim of taking into account all sources of uncertainty and quantifying the contribution of these sources to the overall uncertainty of the system [71]. It is a key step when it comes to aerodynamic analysis and is often used to validate methods and models constructed for aerospace applications, thus ensuring safety and risk management.

By identifying, recognizing, and quantifying the uncertainty that occurs in complex geometries and aerodynamic phenomena, we are able to develop more efficient and reliable solutions with applications in both aerospace and air transport.

As previously mentioned in subsection 2.6.1, the uncertainties investigated in any application fall into two broad categories: aleatoric and epistemic. Given the nature of each type of uncertainty, it is possible to constrain them using various techniques. Aleatoric uncertainties are typically irreducible and essentially stochastic as they are primarily due to the variability of the system [32], but also to input values (initial and boundary conditions). Usually, such uncertainties can be reduced by reconstructing the stochastic terms to achieve greater accuracy in the initial and boundary conditions. The variance in aleatory uncertainties can be propagated in the simulation. Conversely, epistemic uncertainties can be reduced by addressing the source of the uncertainty, which is often model inadequacy. Therefore, it is the researcher's responsibility to reduce them. To mitigate such uncertainties, high-fidelity models are employed, which entails an increased computational cost.

In the field of computational fluid dynamics, a number of techniques are employed to quantify uncertainty in the output of quantities of interest. These include interval analysis, propagation of uncertainty using sensitivity derivatives, Monte Carlo simulations, moment methods, and polynomial chaos. This subsection examines the fundamental techniques employed in the present thesis to fulfill the uncertainty quantification (UQ) methodology: the Monte Carlo and Polynomial Chaos methods.

Monte Carlo Methods

Monte Carlo is a widely used computational technique based on carrying out computational tests corresponding to N random samples which follow a prescribed probability distribution. In the context of uncertainty quantification, MC methods are used to propagate uncertainties through a model and assess their impact on the output.

As per its definition, this method draws, randomly, samples from the input probability space, in this case the joint probability density function (PDF) of the input random variables. Then, these samples are evaluated to estimate the mean and standard deviation of the output, characterized as Quantities of Interest (QoIs).

For a general stochastic problem, the mean $E[v(x,t,w)]$ and variance $V[v(x,t,w)]$ of the output v can be approximated using the MC method as follows:

$$E[v(x,t,\omega)] \approx \frac{1}{N}\sum_{i=1}^{N} v(x,t,\xi_i(\omega)), \tag{2.19}$$

$$V[v(x,t,\omega)] \approx \frac{1}{N-1}\sum_{i=1}^{N} \left(v(x,t,\xi_i(\omega)) - E[v(x,t,\omega)]\right)^2, \tag{2.20}$$

where N represents the number of samples, $\xi_i(\omega)$ is the i-th Monte Carlo sample of the vector of d independent random variables $\xi = \{\xi_1, \ldots, \xi_d\}$ associated with d uncertain parameters, and $v(x,t,\xi_i(\omega))$ is the output at $\xi_i(\omega)$.

The Monte Carlo method has significant advantages, such as simplicity of implementation, non-intrusiveness, and insensitivity to the number of random variables. However, it typically requires a large number of samples to achieve accurate results, therefore increasing the computational cost.

In computational fluid dynamics (CFD), the computational cost of running such a large number of simulations is often prohibitive, necessitating the exploration of more efficient yet accurate alternatives [75].

Polynomial Chaos Methods

Polynomial Chaos (PC) is a mathematical technique used in uncertainty quantification (UQ) to represent and propagate uncertainties through computational models. The general idea behind Polynomial Chaos is to express uncertain model inputs (e.g., parameters, initial conditions) as random variables and then represent the model outputs as a series of orthogonal polynomials in terms of these random variables.

Polynomial Chaos Expansion

A more recent numerical method for estimating uncertainty is that of *Polynomial Chaos Expansions*, which was introduced by Wiener [102] [55] in 1938, in the form of *Homogenous Chaos Expansion* [72]. In PCE, every uncertain parameter in a system is represented by a random variable, denoted as ξ, with the total number of these variables indicated by n_v. For practical purposes, the number of polynomial terms is finite, represented by n_p.

When dealing with multiple uncertain parameters, the expansion must use multi-variable polynomials, not just single-variable ones. The number of multi-variable polynomials, P, depends on n_v and n_p as shown in Equation 2.21:

$$P = \frac{(n_v + n_p)!}{n_v! \cdot n_p!} - 1 \tag{2.21}$$

The system variable $Y(t)$ can be expanded using a multi-variable polynomial basis Ψ as shown in Equation 2.22:

$$Y(t) = \sum_{i=0}^{P} y_i(t)\Psi_i \tag{2.22}$$

A general second-order random process $X(\theta)$ can be described as a series expansion in terms of these polynomials, as shown in Equation 2.23 [104]:

$$X(\theta) = a_0\Psi_0 + a_1\Psi_1(\xi_1(\theta)) + a_2\Psi_2(\xi_2(\theta)) + \cdots = \sum_{i=0}^{\infty} a_i\Psi_i(\xi_i(\theta)) \tag{2.23}$$

This can be simplified as in Equation 2.24:

$$X(\theta) = \sum_{i=0}^{P} \alpha_i\Psi_i(\xi(\theta)) \tag{2.24}$$

In PCE, the polynomials can be extended to Hermite or to other types of polynomials, like Legendre and Laguerre polynomials, which correspond to uniform and exponential distributions, respectively [104].

Once variables are expanded using the chosen polynomial basis, a Galerkin projection is applied by integrating each component of the system with the polynomial basis over its valid region (denoted as Ω).

The inner product of the polynomials is computed as shown in Equation (10):

$$\langle\Psi_i, \Psi_j, \Psi_k\rangle = \int_{\Omega} \Psi_i(\xi)\Psi_j(\xi)\Psi_k(\xi)w(\xi)d\xi \tag{2.25}$$

Where $w(\xi)$ is a weighting function specific to the polynomial basis, given by Equation (11):

$$w(\xi) = \frac{1}{\sqrt{2\pi}}e^{-\frac{\xi^2}{2}} \tag{2.26}$$

Finally, the number of inner products that need to be calculated can be substantial, especially for systems with many variables and higher-order polynomials, as indicated by Equation 2.27:

$$\text{Number of inner products} = (\text{number of polynomial inner products})^{\text{number of uncertain variables}} \tag{2.27}$$

The PCE allows for direct computation of the statistical properties of the model output, such as mean, variance, and higher moments.

Methods that make use of polynomial chaos have significant advantages that make them particularly attractive in uncertainty quantification studies. However, they are also characterized by limitations that may complicate some procedures or even preclude the use of such methods in some applications. PCE has been proven to be an appealing choice for handling uncertainty quantification problems. While using this kind of method, uncertainties can be measured accurately by matching random input values to their corresponding outputs using orthogonal polynomials. Additionally, PCE is useful when it comes to solving problems that contain multiple random variables. It is usually more effective than other methods, which are sensitive to large numbers of variables. Nevertheless, in some cases that require higher-order polynomials, the use of PCE methods is not recommended. Techniques like the *Stochastic Galerkin Method (SGM)* achieve high accuracy by efficiently minimizing error. However, great care should be taken with the information feeding into the PCE sampling, as if the data are different from those contained in the initial assumptions, there is a risk that a significant error will be produced. Lastly, athough PCE methods are often less computationally expensive than Monte Carlo sampling, we have to be cautious of the computational resources available, as they can also be computationally demanding [62] [66].

2.7 Iterative Methods

An important class of methods for solving linear systems consists of approximating solutions using *iterative methods*. Iterative methods are essential in CFD for solving large, complex systems of equations derived from discretized fluid flow equations. Another approach for solving such systems is the use of *direct methods* -like the Gauss elimination- which is based on algebraic elimination. Unlike direct methods, iterative methods obtain the solution by an iterative process, in which an initial assumption of the solution is substituted into the system of equations, to compute the error, resulting in successive approximations until convergence is achieved. Examples of iterative methods used in CFD include the Gauss-Seidel method, the Successive Over-Relaxation (SOR) method, and the Newton Method [15] [45].

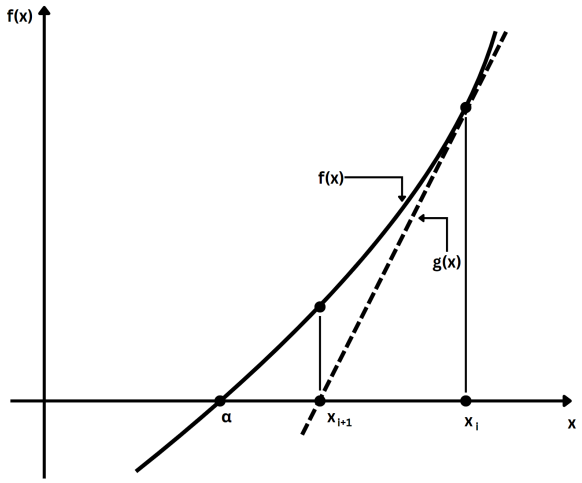

Figure 2.14: Graphical representation of the Newton's method [45]

2.7.1 Newton Method

In this thesis, an iterative *Newton's method* is employed to solve the uncoupled Navier Stokes equations system. Newton's method is characterized by its quadratic convergence, meaning it converges when the initial guess is sufficiently close to the actual root. The primary limitation of this method is that it is required to calculate the derivative $f'(x)$ of the nonlinear function $f(x)$.

Newton's method can be graphically presented in Figure 2.14. The function $f(x)$ is nonlinear, and its derivative $g(x)$ is tangent to $f(x)$.The function $g(x)$ is used to locally approximate the $f(x)$. The root of $g(x) = 0$ is then used as the next approximation for the root of $f(x) = 0$. This process is iteratively repeated until convergence is achieved, which can be mathematically represented as [45]:

$$f'(x_i) = \text{slope of } f(x) = \frac{x_{i+1} - x_i}{f'(x_i)} \tag{2.28}$$

Solving this equation for x_{i+1}, under the condition that $f(x_{i+1}) = 0$, gives:

$$x_{i+1} = x_i - \frac{f(x_i)}{f'(x_i)} \tag{2.29}$$

This equation is applied iteratively until one or both of the following convergence criteria are met:

$$|x_{i+1} - x_i| \leq \epsilon_1 \quad \text{and/or} \quad |f(x_{i+1})| \leq \epsilon_2 \tag{2.30}$$

The Newton's method, also known as Newton-Rhapson (N-R), is a widely used optimization technique, known for its robustness and reliability. Consequently, it is a preferred choice for many optimization problems. Nevertheless, in practice, obtaining the second derivative can be challenging, which limits the method's applicability in certain situations [77]. Another limitation of the method is the possibility of failure to converge when applied to polynomials with only complex roots if the initial guess is a real number [95]. This potential for divergence emphasizes the necessity of considering the method's limitations in specific applications.

In general, the N-R method remains a powerful and versatile optimization tool, offering significant advantages. However, its limitations, particularly in cases where the second derivative is difficult to obtain or when dealing with certain types of polynomials, must be carefully evaluated in the context of the specific problem at hand.

Chapter 3

Methodology

To address the issue at hand, an algorithm employing an approximate iterative Newton method is employed to solve each of the equations comprising the Navier-Stokes system of equations under steady-state conditions. The Monte Carlo method is used to generate samples of the uncertain parameters associated with the research problem, applying the Hammersley pseudo-random method. Polynomial chaos is used in the context of uncertainty quantification to express the field variables associated with the flow.

3.1 Methodology Overview

The methodology employed to address the research question is outlined in the logic diagram presented in Figure 3.1.

Firstly, the initial conditions are established and the samples are generated utilizing a Monte Carlo method. Subsequently, the uncertain parameters of the problem are defined. A joint probability density function (PDF) is generated to estimate the total uncertainty resulting from the combined effect of both uncertain parameters. Subsequently, the samples for the uncertain variables are generated and stored for utilization in the following stages of the methodology.

A pivotal stage is the determination of the coordinates that constitute each NACA airfoil. In this step, the perimeter of any NACA airfoil is created, according to the designer's preference. This is achieved through the application of equations and principles established in the 1933 NACA report [6], which will be presented in detail below.

The third step is the creation of a grid to discretize the problem domain, thereby simplifying the problem and facilitating its solution. A suitable mesh generation function is defined, which accepts as input the desired angle of attack and mesh density. The function allows for the rotation of the wing, which enables the angle of attack to be adjusted while assuming a constant horizontal flow.

A polygon is constructed within the rectangle, comprising all points of the rotated (or unrotated) coordinates of the airfoil. The aforementioned polygon will be excluded from the construction of the mesh, as it represents solid geometry. The position of the field should be such that the center is located at a sufficient distance from the walls to ensure that the flow conditions are properly represented. Finally, an unstructured, two-dimensional mesh is created in an automated manner using an appropriate library and functions, with the geometry of the airfoil in question excluded as previously mentioned.

Eventually, the mesh generation function is employed, whereby the input parameters (angle of attack, mesh density) and boundary conditions are defined.

In order to define the boundary conditions, it is necessary to utilize function spaces to determine the type of the basic quantities, namely velocity as a vector and pressure as a gradient.

Next, the solution of the Navier-Stokes equations is carried out, and the aforementioned boundary conditions are defined. In addition, the uncertain variables that have been set are also taken into account.

In the final stage of the methodology, the flow function is calculated for a given two-dimensional velocity vector u, that is to say, a scalar field that describes the flow patterns in a two-dimensional fluid field. The flow vorticity, which represents the local rotation of the fluid, is calculated. Based on these values and the data obtained following the solution of the model, the mean and standard deviation are calculated. The data must be stored in appropriate files for subsequent analysis.

The code used to solve the problem in question in this thesis was developed in the *Python* programming language. The main Software used to solve the Navier-Stokes equations and, more generally,

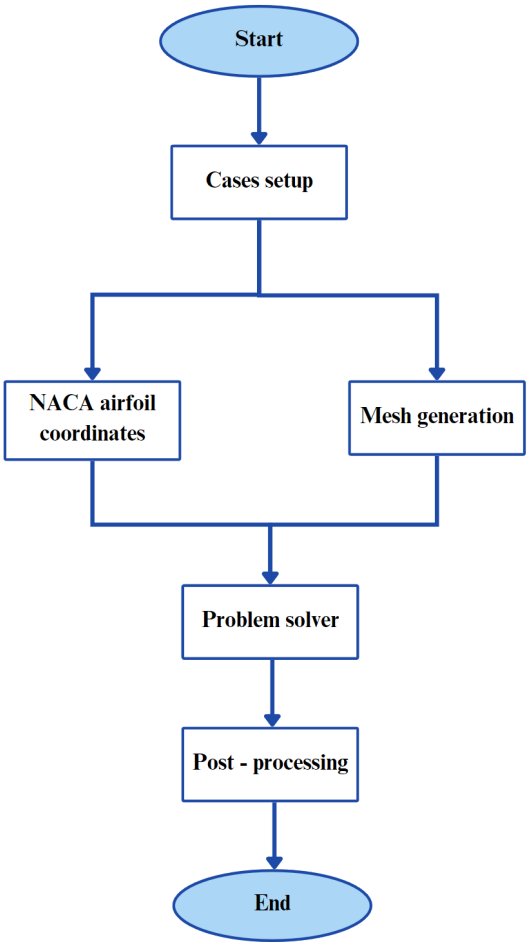

Figure 3.1: Logic diagram of the methodological approach

differential equations by finite element methods, is the textitFEniCS Project [5]. Specifically, the software component *DOLFIN* [4] is employed, which provides the problem-solving environment and serves as a computational backend, and *mshr* for the mesh generation [7]. Additionally, the *NumPy* library [8] is used to execute mathematical operations with the use of matrices, ChaosPy [3] facilitated uncertainty quantification through the application of polynomial chaos methods.

Summing up, the methodology described involves the following steps:

1. **Sample Generation**: Initial conditions are set, and samples are generated using the Monte Carlo method. Uncertain parameters and their joint probability density function (PDF) are defined to estimate total uncertainty.

2. **NACA Airfoil Coordinates**: Coordinates for NACA airfoils are determined using equations from the 1933 NACA report.

3. **Grid and Mesh Creation**: A grid is created to discretize the domain, with a mesh generation function taking the angle of attack and mesh density as inputs. The airfoil geometry is excluded from the mesh.

4. **Boundary Conditions**: Boundary conditions are defined using function spaces for velocity and pressure.

5. **Navier-Stokes Solution**: The Navier-Stokes equations are solved, considering the boundary conditions and uncertain variables. Flow patterns and vorticity are calculated.

6. **Data Analysis**: Mean and standard deviation are calculated from the model data, which is stored for analysis.

3.2 Cases Set Up

As previously stated, the initial step is to establish the initial conditions for the cases to be considered. The requisite input values are the Reynolds number, the standard deviation, and the number of samples to be generated by the Monte Carlo method employed.

The Reynolds number is a crucial parameter in the analysis of the airflow around an airfoil, as it serves as a measure of comparison between the different flow types. Various tests are carried out for different values of Reynolds number, applied to different types of airfoil, as presented in Table 4.3 in Section 4.2.1 . The Reynolds number samples generated are set to follow a uniform distribution function within the interval of $[Re \cdot (1 - \text{standard deviation}), Re \cdot (1 + \text{standard deviation})]$, and the free flow velocity (U_∞) is introduced and set to follow a normal distribution with mean $\mu = 1$ and standard deviation $\sigma = 0.1$.

The desired number of samples is generated in accordance with a joint probability density function of the Reynolds number and U_∞, employing the Monte Carlo method, in particular, the quasi-Monte Carlo/Halton sequence. The way in which samples are obtained through this sequence is described in Section 2.6.3.

Finally, the resulting parameter values are stored for use in the next steps of the methodology.

3.3 Design Approach

The problem is initially addressed by constructing the two-dimensional geometry of the airfoil. The specific types of airfoils studied are specified in Section 4.2.1. The airfoil is situated inside an appropriately computational domain containing a mesh to properly represent the existing flow phenomena. This section outlines these three crucial steps for the creation of the computational domain in which the simulation will take place.

3.3.1 NACA Airfoil Design

The development and design of NACA airfoils involve precise calculations to define their shape and characteristics.

Through calculations and conditions set by the NACA researchers, from the general equation describing the profile of an airfoil:

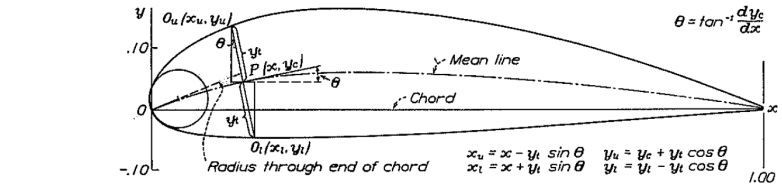

x	y_t	y_c	$\tan\theta$	$\sin\theta$	$\cos\theta$	$y_t \sin\theta$	$y_t \cos\theta$	x_u	y_u	x_l	y_l
0	0	0	[1] 0.40000	0.37140	0.92840	0	0			0	0
0.01250	0.03314	0.00489	.38333	.35793	.93375	0.01186	0.03094	0.00064	0.03583	0.02436	−0.02605
.30000	.10503	.06000	0	0	1	0	.10503	.30000	.16503	.30000	−.04503
.60000	.07986	.04898	−.07347	−.07327	.99731	−.00585	.07965	.60585	.12863	.59415	−.03067
1	.00221	0	−.17143	−.16897	.98562	−.00037	.00218	1.00037	.00218	.99963	−.00218

[1] Slope of radius through end of chord.

FIGURE 2.—Method of calculating ordinates of N.A.C.A. cambered airfoils.

Figure 3.2: Method of calculating coordinates of NACA airfoils [51]

$$\pm y = \alpha_0\sqrt{x} + \alpha_1 x + \alpha_2 x^2 + \alpha_3 x^3 + \alpha_4 x^4 \tag{3.1}$$

The equation for NACA airfoils, which have a thickness of about 20 % of their chord, was derived:

$$\pm y = 0.29690\sqrt{x} - 0.12600x - 0.35160x^2 + 0.24830x^3 - 0.10150x^4 \tag{3.2}$$

If a different thickness is required, the more general formula can be utilized by multiplying the above equation with the appropriate factor:

$$\pm y = \frac{t}{20}(0.29690\sqrt{x} - 0.12600x - 0.35160x^2 + 0.24830x^3 - 0.10150x^4) \tag{3.3}$$

Furthermore, the following calculation can be used to determine the radius of the leading edge:

$$r_t = \frac{1}{2}\left(\frac{t}{0.20}\alpha_0\right)^2 = 1.10t^2 \tag{3.4}$$

Where t is the thickness of the airfoil.

As previously stated, the mean line is a crucial parameter in the NACA airfoil design. It is represented by a general equation:

$$y_c = b_0 + b_1 x + b_2 x^2 \tag{3.5}$$

The leading and trailing points' coordinates for a NACA airfoil were defined at $x = 0, y_c = 0$ and $x = 0, y_c = 0$, respectively.

The parameter y_c corresponds to the geometric locus of the points belonging to the chord of the airfoil.

To calculate the curvature of the mean line, the maximum of the entire curve must be determined.

$$y_c = \frac{m}{(1-p^2)}[(1-2p) + 2px - x^2] \Rightarrow y_c = \frac{m}{p^2}(2px - x^2) \tag{3.6}$$

The wing profile coordinates consist of x_u and y_u for the upper surface and x_l and y_l for the lower surface. Additionally, θ denotes the angle between the tangent of the mean line and the x-axis:

$$\theta = \tan^{-1}\frac{dy_c}{dx} \tag{3.7}$$

The report authors provided a diagram that presents the design elements of an airfoil and offers examples of how to calculate the aforementioned parameters:

The upper and lower surface coordinates can be calculated using the formulas obtained from the diagram in Figure 2.8 [51].

$$x_u = x - y_t \sin\theta \tag{3.8}$$

$$y_u = y_c + y_t \cos\theta \tag{3.9}$$

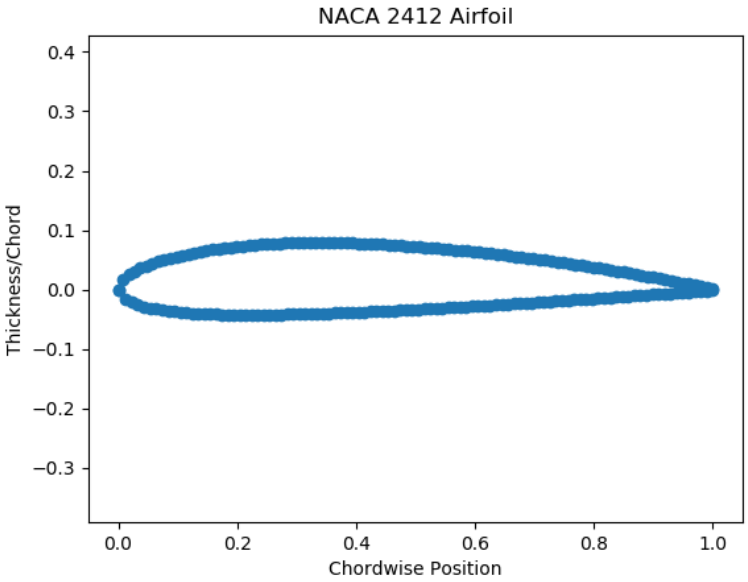

Figure 3.3: Graphical representation of NACA 2412 as generated from the code

$$x_l = x + y_t \sin\theta \tag{3.10}$$

$$y_l = y_c - y_t \cos\theta \tag{3.11}$$

Finally, the center for the radius of the leading edge is placed at the tangent of the mean line to the leading edge.

In conclusion, the methodology described above serves as the foundation for the efficient design of NACA airfoils. By using the aforementioned accurate calculations, engineers are able to determine the optimal NACA airfoil type for aerodynamic applications that require specific characteristics.

In this thesis, the above calculations were incorporated into the problem-solving code in order to visualize the geometry of the airfoil, with the ability to switch between different types, e.g. 4418, 0012, etc. This affords the code considerable flexibility, enabling the study of different airfoils in terms of their characteristics. A portion of this code is presented in the Appendix A. An example of the generated geometry of a NACA **2414** airfoil is provided in Figure 3.3.

3.3.2 Mesh generation

During the mesh creation phase, the coordinates obtained by the above calculations were used for the formation of the two-dimensional geometry of any NACA airfoil, whether symmetrical or not. In addition to the various airfoil characteristics and flow velocities, the study also encompasses different angles of attack, which had to be incorporated into the code. A suitable procedure containing the construction of matrices allows the airfoil to be rotated in order to properly represent the different angles of attack. The center of rotation is considered to be the aerodynamic center which, as previously discussed in subsection 2.3.2, is taken at 25% of the airfoil chord, where $c = 1$.

Afterwards, the orthogonal computational domain is constructed. Its dimensions and the position of the airfoil within the computational domain are derived from the work of Sener and Arsku [86]. The rectangle dimensions are $30c \cdot 20c$. The aerodynamic center of the airfoil is situated at the midpoint of the vertical dimension, with the assumption that its position is at $y = 0$. It is therefore assumed that the airfoil is equidistant from the upper and lower sides of the domain. Furthermore, the leading edge of the airfoil is located at a distance of $10c$, which results in the domain represented in Figure 3.4.

The mesh type selected for this thesis is the unstructured as opposed to the structured type. Furthermore, the mesh is automatically generated. The aforementioned options offer significant advantages, which are discussed in greater detail in Subsection 2.5.3.

The automated creation of the mesh was performed using the FeniCS software, specifically the mesh generator, *mshr*. This library enables the visualization of geometries, such as airfoils, which can be formed from basic shapes such as circles, rectangles, and polygons. Once the airfoil geometry under consideration

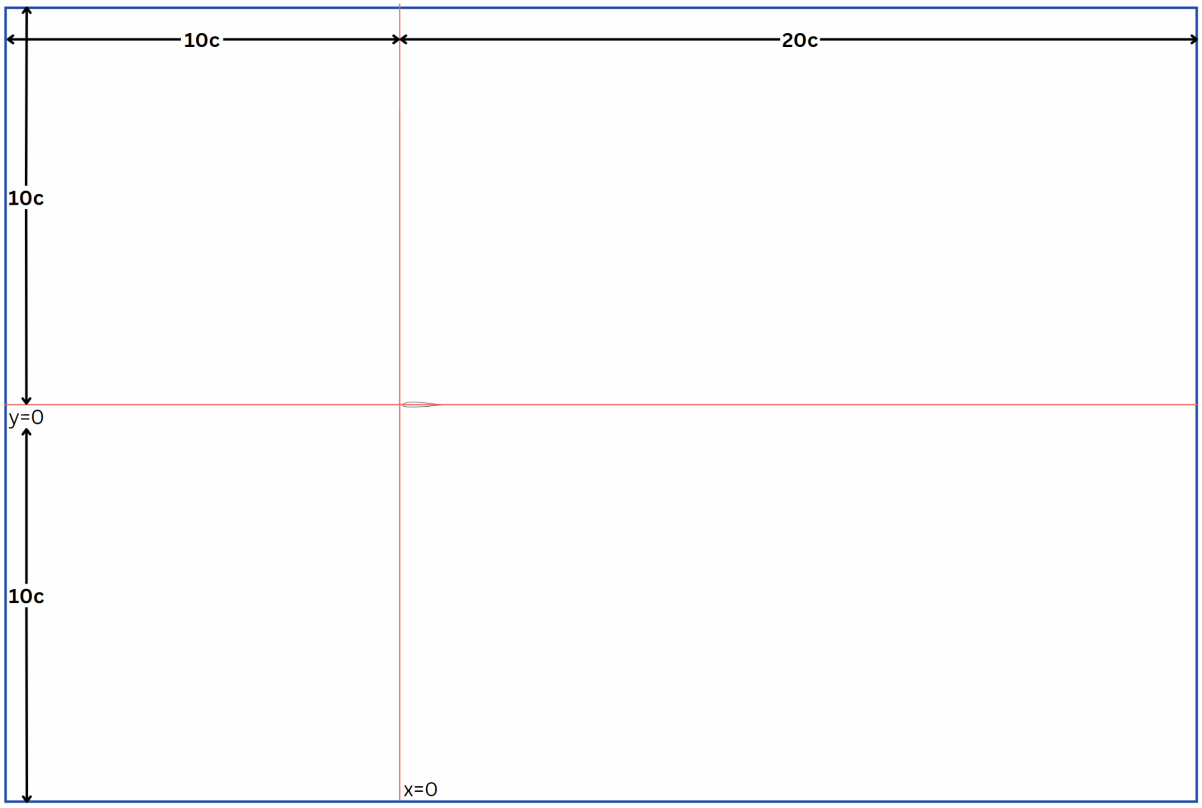

Figure 3.4: Computational domain

is defined, the algorithm discretizes the field with minimal input data and user intervention. In particular, the input parameter required to generate the mesh is the *mesh density*, which can be adjusted to produce a mesh of varying coarseness or fineness. An example of the generated mesh around a NACA 2412 airfoil is illustrated in Figure 3.5.

Once the mesh has been successfully generated, any necessary refinements can be made in accordance with the requirements of the simulation (see example in Figure 3.5). Furthermore, the preferred angle of attack can be set.

3.4 Boundary Conditions

In the context of UQ in flows around NACA airfoils, the identification of appropriate boundary conditions plays a crucial role in flow visualization and the accuracy of the computational results. Boundary conditions represent the influence of the environment on the model [33] and significantly affect the solution of the governing equations. In the present case, the boundary conditions applied are as follows:

- **Inlet:** Defines the region from which the fluid enters the computational domain. This region corresponds to the left-hand edge of the computational domain.
- **Outlet:** Defines the fluid's exit region from the computational domain, which corresponds to its right edge.
- **No-slip wall:** In the area where it is applied, the fluid velocity is assumed to be the same as that of the wall [33], i.e. zero for a stationary wall. This area refers to the surface of the airfoil.
- **Symmetry:** This boundary condition is used to simplify the simulation and is applied to the upper and lower edges of the computational domain.

These boundary conditions are integral to the simulation, and ensure that the fluid flow around the NACA airfoil is accurately modeled, taking into account the uncertainties in the aerodynamic analysis.

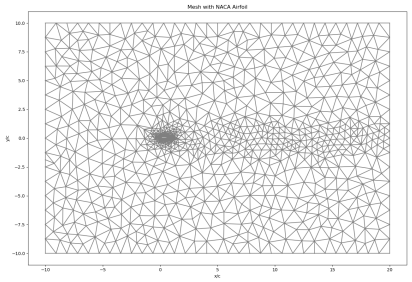

(a) Example mesh (mesh density = 20)

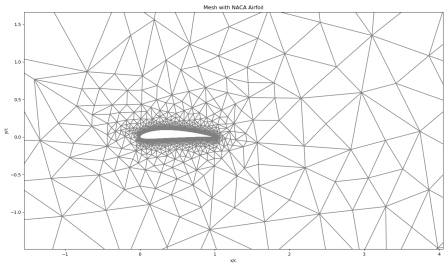

(b) Example mesh (zoomed in)

Figure 3.5: Example mesh for mesh density = 20

3.5 Model Solver

This research is mainly focused on the solution of the Navier-Stokes equations. To this end, a custom model solver has been developed, as seen in Subsection 3.5.3. This solver has been designed to handle complex interactions between the fluid flow and the airfoil geometry. As explained in the previous sections, boundary conditions and stabilization techniques must be incorporated into the code. This approach guarantees that the velocity and pressure fields can be reliably and efficiently computed, as they are essential for evaluating the aerodynamic performance of the airfoil under varying conditions.

3.5.1 Discretization and Monte Carlo Simulation Results

As previously mentioned, the discretization process is one of the main steps of the CFD simulations. The elements used for the construction of the mesh are of *Langragian* type, one the most commonly used element types. A positive integer k is considered as the order of the Lagrange element. On simpler meshes, like the 2D mesh employed in this thesis, on each mesh element, u is a polymomial of order k. In general, for a mesh element of type T, u belongs to the Lagrange shape function space $Lag_k(T)$. For each of the node points of an element p_i, there is a degree of freedom $U_i = u(p_i)$ and a basis function ϕ_i.

Considering that the basis functions are continuous:

$$u = \sum_i U_i \phi_i \tag{3.12}$$

The Lagrange element of order 1 is called the *linear* element and the Lagrange element of order 2 is called the *quadratic* element. For scalar fields such as pressure, linear Lagrange elements are employed, while for vector fields like velocity, quadratic elements are used. In the specific code written for this thesis, these elements are combined into a mixed element, that simultaneously represents the velocity and pressure fields. Based on these elements, the required function spaces are defined. The *mixed* function space W represents the combined space for both velocity and pressure, enabling the solution of these fields, simultaneously. For the velocity and pressure fields respectively, their function spaces are denoted V and Q.

```
1         P1 = FiniteElement("Lagrange", mesh.ufl_cell(), 1)
2         P2 = VectorElement("Lagrange", mesh.ufl_cell(), 2)
3         TH = MixedElement(P2, P1
```

```
4
5         W = FunctionSpace(mesh, TH)
6         V = FunctionSpace(mesh, P2)
7         Q = FunctionSpace(mesh, P1)
```

Listing 3.1: Finite elements and Function Spaces

Consequently, the previously computed Monte Carlo simulation results of the velocity and pressure fields are loaded for further processing. Each Monte Carlo simulation contributes to the reconstruction of a *mean* velocity field which is applied to the mixed function space. The velocity and pressure components are extracted, as well as the corresponding data of W and they are compared to the velocity and pressure fields of the current simulation, resulting in a relative residual, This residual provides a measure of the difference between the current and past velocity fields.

3.5.2 Main Solver

Inside the main solver portion of the code, the Navier-Stokes equations are solved under the specified boundary conditions. Specifically, the way the boundary conditions established in Section 3.4 are applied, is presented on Table 3.1.

Boundary Condition	**Operation**
Inlet	Applies to the specified inlet velocity to the domain boundary where the fluid enters
Outlet	Sets the pressure to zero at the outlet, allowing the fluid to exit the domain
No-slip	Enforces a zero velocity condition on the airfoil surface, ensuring the fluid adheres to the surface
Symmetry	Ensures that the vertical component of the velocity is zero along the top and bottom boundaries (symmetry planes)

Table 3.1: Boundary Conditions

Apart from solving the Navier-Stokes equations, the model solver is also responsible for managing the iterative method involved in the UQ process. The initial values of velocity (u_0) and pressure (p_0) fields serve as the initial guess from which the iterative process begins. The values are both set to zero. The inlet velocity is considered a constant vector with a magnitude of the free stream velocity, which was specified during the first step of the methodology (see Section 3.2), in the horizontal direction. The outlet pressure is set to a constant value of zero, representing zero gauge pressure at the outlet.

In the following step, the variational forms needed to solve the Navier-Stokes equations are defined. These forms are also known as the *weak* forms of the momentum and continuity equation. The weak form of each equation can be expressed by multiplying its non-dimensional form with a test function.

To achieve numerical stabilization, two basic techniques are used which restrict the oscillations and instabilities that occur during the simulation. Such techniques include the *Streamline-Upwind Petrov-Galerkin (SUPG)* method and the *Pressure-Stablizing Petrov-Galerkin method (PSPG).*

- **SUPG:** This is a widely used method of stabilization, especially in the context of transportation problems. In such problems, SUPG has the main advantage of limiting the unphysical oscillations that may arise in the solution, as is common with standard Galerkin methods. This approach ensures the stability and accuracy of the solution, even in cases in which the Reynolds number approaches high values [24]. The stabilization term introduced is proportional to the square of the mesh cell diameter (h) and the user-defined parameter beta (β).

```
1         # stabilization parameter
2         h = CellDiameter(mesh)
3         beta = 0.05
4         delta = beta*h*h
5
6         # add SUPG stabilization
7         F +=  delta*inner(grad(u), grad(v))*dx
```

Listing 3.2: SUPG stabilization

- **PSPG:** It is a stabilization technique, which contributes to the achievement of accuracy and stability in the simulations of incompressible fluid flows. This approach focuses on the analysis of the pressure field. In order to obtain a smooth pressure field, a stabilization term is added to the pressure equation, which results in a reduction of the simulation oscillations, even in coarser meshes [47] [53].

```
F += tau*inner(grad(q), r)*dx
```

Listing 3.3: PSPG stabilization

The iterative process which is performed in a parallel computing context, which allows for the efficient distribution of computational tasks across multiple processors. The simulation uses key variables that are initialized from the data structure obtained in the first step of the methodology. These variables are:

- The total number of Monte Carlo samples,
- The parameter samples used to run the simulation,
- The Reynolds number and the relative standard deviation to quantify the uncertainty,
- The maximum number of iterations, which is defined as 100, and the convergence tolerance for the iterative procedure, which is defined as 10^{-10},
- Variables that record the values of the residuals after each iteration, and which ensure the start of the iterative loop.

Within each of the iterations, the velocity and pressure fields are calculated separately. After processing all samples, the maximum residual from the current iteration is calculated, which is used to evaluate the convergence of the solution.

The iterative process is completed by storing all relevant data, including the number of samples, residuals, and key parameters for further analysis and verification.

The last stage of the methodology, as mentioned above, is the stage of extraction of results and post-processing. In this step, the mean and standard deviation of the calculated solutions for the velocity and pressure fields are calculated. These quantities represent the uncertainty in the flow field due to changes in the input parameters. In addition, the flow function is calculated, which provides insight into the flow patterns around the airfoil. Data such as velocity and pressure values are stored for visualization and further analysis.

In the next subsection, a numerical formulation designed to solve the Navier-Stokes equations for fluid flow under uncertain conditions will be presented. This approach aims to improve computational efficiency while providing a framework for capturing the effects of uncertainty in fluid dynamics problems and is the novelty of this thesis.

3.5.3 Numerical Formulation

Unlike traditional approaches, this methodology utilizes polynomial chaos expansions to model pressure and velocity as stochastic variables, which allows for a comprehensive quantification of uncertainty in flow fields. By reformulating the Navier-Stokes equations for each term of the polynomial expansion, a set of coupled nonlinear equations is obtained. The complexity in solving these equations is addressed by applying Newton's iterative method, which decouples the nonlinear terms, allowing each system to be solved separately.

The basic parameters of the problem (pressure (p), velocity vector (u), and temperature (T)), to be used in its solution, are expressed in polynomial form, applying the Polynomial Chaos method, as follows:

$$\begin{aligned} p(x) &= \sum_{i=1}^{P} p_i(x)\psi_i \\ u(x) &= \sum_{i=1}^{P} u_i(x)\psi_i \\ T(x) &= \sum_{i=1}^{P} T_i(x)\psi_i \end{aligned} \tag{3.13}$$

Where: x: the spatial domain, and ψ_i: the basis functions of the polynomial chaos.
The Navier - Stokes equations are formulated for the field variables for $k \in (0, P)$ as follows:

$$\nabla \cdot u_k = 0 \tag{3.14}$$

$$\frac{\partial u_k}{\partial t} + \sum_{i=0}^{P}\sum_{j=0}^{P} C_i j \left(u_i \cdot \nabla\right) u_j = -\nabla p_k + \frac{1}{Re_k}\Delta u_k + f_k \tag{3.15}$$

$$\frac{\partial T_k}{\partial t} + \sum_{i=0}^{P}\sum_{j=0}^{P} C_i j \nabla \cdot (u_i T_j) = Pr_k \Delta T_k \tag{3.16}$$

Where: t: time, Re: Reynolds number, Pr: Prandtl number, f: forcing term, such as gravity, and C_ijk: multiplication tensor

$$C_{ijk} = \frac{\langle \psi_i \psi_j \psi_k \rangle}{\langle \psi_k \psi_k \rangle} \tag{3.17}$$

As can be seen from the above formulas, the nonlinear terms of the momentum and energy equations construct P + 1 systems of equations, which in turn constitute a system of equations of such magnitude that its solution is extremely costly. To study and quantify uncertainty for two-dimensional flows, an iterative algorithm based on Newton's method for optimization problems is applied. The Newton or Newton-Raphson method is a method of successive approximations to find approximate solutions to a problem. Each approach is based on the estimate of the previous iteration, as indicated by the general form of the method:

$$x_{n+1} = x_n - [F'(x_n)]^{-1} F(x_n) \tag{3.18}$$

To solve the non-linear equation:

$$F(x) = 0 \quad (F : X \to Y) \tag{3.19}$$

Where X, Y: Banach fields, F': the derivative of F, x_i: the approximation corresponding to iteration i, and $i = 0, 1, ...$: the iteration number [34]. For each equation k of the system of equations (see Equations 7 - 9), only the nonlinear term is coupled and can be split:

$$\sum_{i=0}^{P}\sum_{j=0}^{P} C_{ijk}(u_i \cdot \nabla)u_j = \sum_{i=0}^{k-1}\sum_{j=0}^{k-1} C_{ijk}(u_i \cdot \nabla)u_j + (u_k \cdot \nabla)u_k + \sum_{i=k+1}^{P}\sum_{j=k+1}^{P} C_{ijk}(u_i \cdot \nabla)u_j \tag{3.20}$$

$$\sum_{i=0}^{P}\sum_{j=0}^{P} C_{ijk}\nabla \cdot (u_i T_j) = \sum_{i=0}^{k-1}\sum_{j=0}^{k-1} C_{ijk}\nabla \cdot (u_i T_j) + \nabla \cdot (u_k T_k) + \sum_{i=k+1}^{P}\sum_{j=k+1}^{P} C_{ijk}\nabla \cdot (u_i T_j) \tag{3.21}$$

Replacing Eq. 3.20 and 3.21 to Eqs. 3.15 and 3.16 we obtain the basic equations governing the problem:

$$\nabla \cdot u_k = 0 \tag{3.22}$$

$$(u_k \cdot \nabla)u_k + \nabla p_k - \frac{1}{Re_k}\nabla^2 u_k - f_k = -f_{u \neq u_k} \tag{3.23}$$

$$\nabla \cdot (u_k T_k) - P_r \nabla T_k = -f_{T \neq T_k} \tag{3.24}$$

where:

$$f_{u \neq u_k} = \sum_{i=0}^{k-1}\sum_{j=0}^{k-1} C_{ijk}(u_i \cdot \nabla)u_j + (u_k \cdot \nabla)u_k + \sum_{i=k+1}^{P}\sum_{j=k+1}^{P} C_{ijk}(u_i \cdot \nabla)u_j \tag{3.25}$$

$$f_{T \neq T_k} = \sum_{i=0}^{k-1}\sum_{j=0}^{k-1} C_{ijk}\nabla \cdot (u_i T_j) + \nabla \cdot (u_k T_k) + \sum_{i=k+1}^{P}\sum_{j=k+1}^{P} C_{ijk}\nabla \cdot (u_i T_j) \tag{3.26}$$

The system of equations 3.22 - 3.24 is solved by Newton's method, which is used iteratively among the $P+1$ systems of equations of the uncertainty quantification problem to solve each k sets of equations of system 3.22 - 3.24 separately, rather than together, connected. The nonlinear terms $f_{u \neq u_k}$ and $f_{T \neq T_k}$ are treated as source terms, estimated from the old iteration $n-1$ or previous solutions in the same iteration.

Chapter 4

Results

4.1 Benchmark Case

A variety of techniques and methods are used for the verification of the code. A widely known benchmark case is the *lid-driven cavity*. This geometry, as the name suggests, is a square cavity constructed by three solid walls in which no-slip boundary conditions prevail. The upper side of the square is, in essence, a lid moving with a tangential unit velocity. The unit square representing the geometry studied in this problem is shown in Figure 4.1. In this particular application, the Navier-Stokes and continuity equations are solved.

In addition, for sampling the uncertain parameters of the problem, as in the basic methodology applied in this thesis, the Monte Carlo method is used, using the Hammersley pseudo-random method. The quantities of interest (QOIs) of the uncertainty quantification study are selected, which are allowed to deviate $\pm 0.1\%$ from their mean value. The quantities under uncertainty are the Reynolds number and the lid velocity. The resulting samples can be represented in a space of sample parameters, which is shown in Figure 4.2. The sample values of u_lid and Re follow normal and uniform distributions respectively. It should be noted that the number of samples used depends on several factors, including the complexity of the problem and the desired level of accuracy. Nevertheless, it is necessary to take into account the computational resources available to perform the simulation.

To solve the Navier-Stokes equations, FEM is employed for the discretization of the non-linear equations. The mesh constructed for the application of the FEM consists of $N \times N$ triangular-shaped cells, with the cell size decreasing near the walls of the cavity. The mesh for $N = 20$ is demonstrated in Figure 4.3.

For the present benchmark case, in order to establish a baseline for comparison, two separate scenarios have been examined for the low Reynolds numbers:

- $Re = 100$
- $Re = 400$

The following subsections present the results of the simulations of the lid-driven cavity problem for the aforementioned Reynolds numbers.

4.1.1 Streamline plots

A particularly valuable set of results is that of the mean flow fields, which include contour plots of velocity, pressure, and stream function. Such plots are an illustration of the spatial distribution of the magnitude of these specific quantities, providing valuable insight into areas of increased velocity and pressure, as well as the behavior of the flow, by focusing on the density of the streamlines.

Starting from the first set of plots of Figure 4.4, these plots display the variations of different fluid dynamics parameters such as the velocity, the pressure, and the stream function. It is important to note that Figure **??** refers to the Reynolds number with a value of 100. The plot of Figure 4.4a shows the velocity field contours inside the cavity. In the plot, vortices can be clearly observed. The primary vortex dominates near the center of the unit square cavity, while smaller, secondary vortices may start to form on the bottom corners (at this resolution, only the bottom left secondary vortex is visible). One may also observe that denser lines occur around the vortices, especially the main one, indicating high-velocity

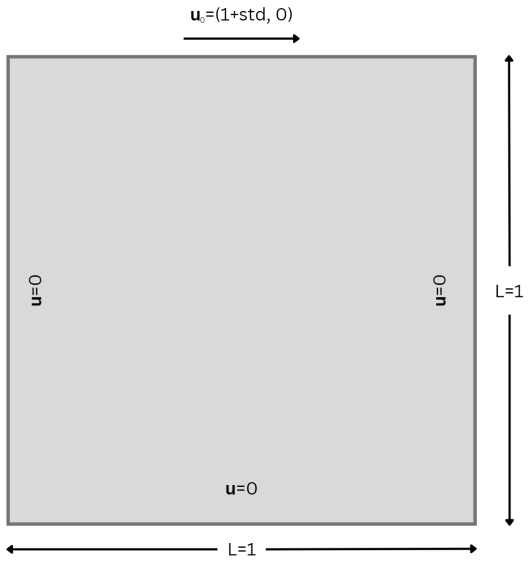

Figure 4.1: Geometry and boundary conditions of the lid-driven cavity

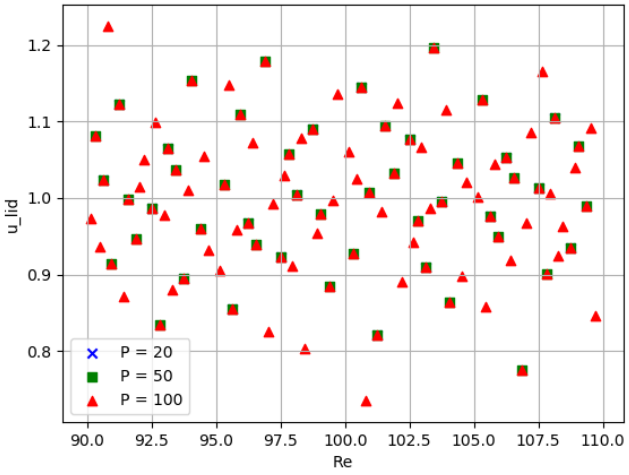

Figure 4.2: Sample parameter space of lid-driven cavity

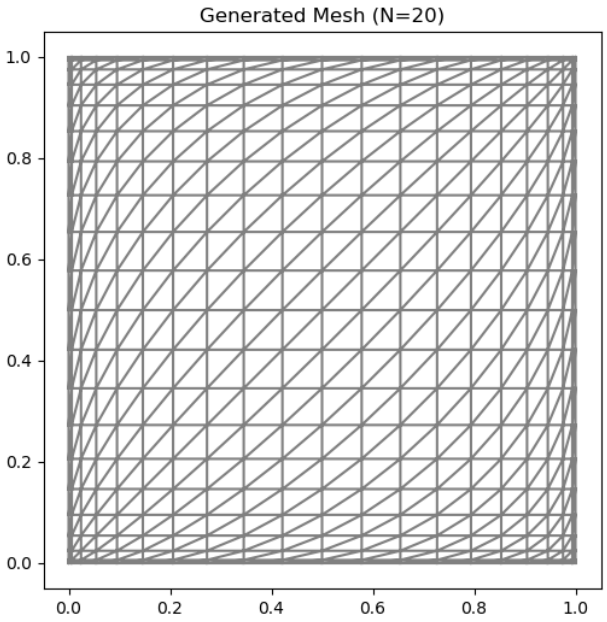

Figure 4.3: Generated mesh for the lid-driven cavity

gradients around the eddy formation, which is typical in lid-driven cavity flows. In Figure 4.4b, the contour plot reflects the pressure gradient within the cavity. On the top corners of the geometry, regions of high pressure can be seen, likely due to the movement of the lid, while the lowest pressure region is located at the bottom of the primary vortex. Similar pressure contours are presented in the work of J. Banaszek et al. [21]. Lastly, the stream function contour plots give an overview of the flow structure, as well as the position of the primary and secondary vortices.

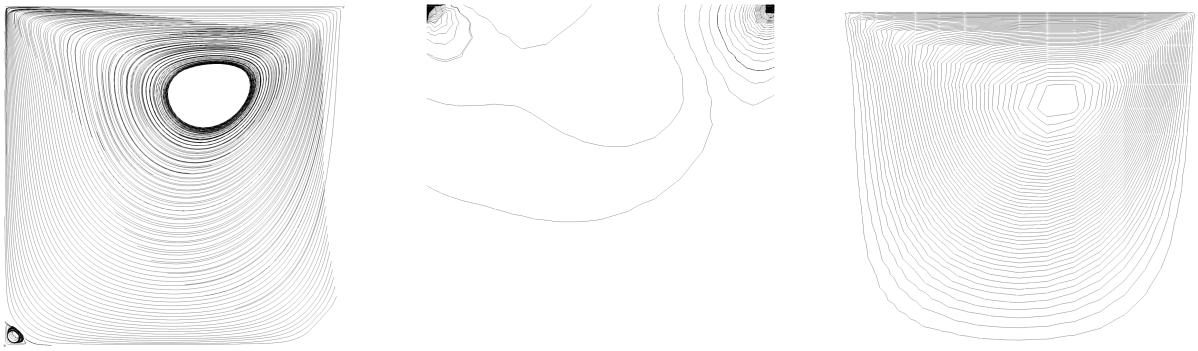

(a) Velocity (b) Pressure (c) Streamfunction

Figure 4.4: Contour Plots of Velocity, Pressure, and Streamfunction for Lid-Driven Cavity Flow at ($Re = 100$)

Similar to the plots of the Figure **??**, the mean streamline contours for $Re = 400$ are presented in Figure 4.5. The velocity plot shows similarities regarding the flow structure and the formation of vortices. However, compared to the $Re = 100$ case, the primary vortex seems to have shifted upward and to the right, with denser streamlines around it, indicating stronger inertial effects that are expected with the increase of Reynolds number. Additionally, the pressure distribution is relatively smooth due to the low Reynolds number. The stream function plot shows the shift of the primary vortex in the cavity, as well as the increase in the size of the secondary vortices near the bottom corners (not visible in the Figure), which could mean that the recirculation regions have also increased.

In the work of M. Gupta and J. Kalita [42], a table containing the strength and location of the centers

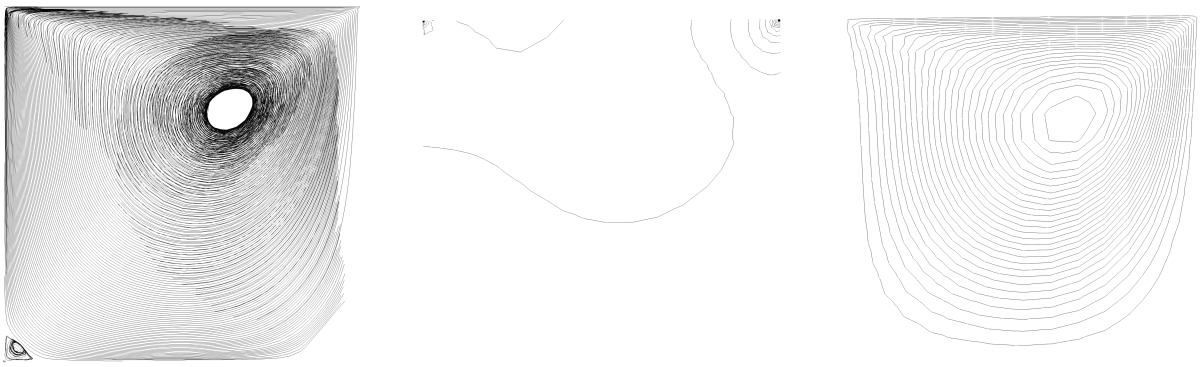

(a) Velocity (b) Pressure (c) Streamfunction

Figure 4.5: Contour Plots of Velocity, Pressure, and Streamfunction for Lid-Driven Cavity Flow at ($Re = 400$)

of primary vortex for the lid-driven square cavity problem, for various Reynolds numbers. Such results come from different scientific papers cited in [99], [38], [85], and [46], and are presented in the table below (Table 4.1)

Re	**Source**	$\psi_{\mathbf{min}}$	x	y
100	*S. P. Vanka* [99]	-0.103	0.6188	0.7375
	U. Ghia et al. [38]	-0.103	0.6172	0.7344
	R. Schreiber et al. [85]	-0.103	0.6167	0.7417
	S. Hou et al. [46]	-0.103	0.6196	0.7373
	M. Gupta et al. [42]	-0.103	0.6125	0.7375
400	*S. P. Vanka* [99]	-0.114	0.5563	0.6000
	U. Ghia et al. [38]	-0.114	0.5547	0.6055
	R. Schreiber et al. [85]	-0.113	0.5571	0.6071
	S. Hou et al. [46]	-0.112	0.5608	0.6078
	M. Gupta et al. [42]	-0.113	0.5500	0.6125

Table 4.1: Comparison of $\psi_{\min}$, x, and y for $Re = 100$ and $Re = 400$ [42]

For the $Re = 100$ and $Re = 400$ cases, the following results occur:

Re	$\psi_{\mathbf{min}}$	x	y
100	-0.1026	0.6111	0.7378
400	-0.0984	0.6363	0.7034

Table 4.2: Comparison of $\psi_{\min}$, x, and y for $Re = 100$ and $Re = 400$

Table 4.1 provides the results from different research papers for both $Re = 100$ and $Re = 400$. The values of the strength of the primary vortex, as well as the horizontal and vertical positions of the vortex center, respectively, serve as comparison targets to the results of the simulation we performed, in order to validate our method. Regarding the simulation results presented in Table 4.2, for $Re = 100$ the minimum streamfunction, ψ_min, aligns closely with the previous data in Table 4.1. Additionally, the vortex center position seems to be similar to other findings. However, for $Re = 400$ there are some variations when comparing the results. The ψ_min value indicates a slightly stronger vortex, as well as a shift to the vortex center.

4.1.2 Uncertainty Quantification

In this methodology, the Uncertainty Quantification analysis was conducted by analyzing the standard deviation contour plots for velocity, pressure, and streamfunction. These plots demonstrate the areas and the magnitude of the variations computed for each field, with higher values of standard deviation being highlighted with warmer colors.

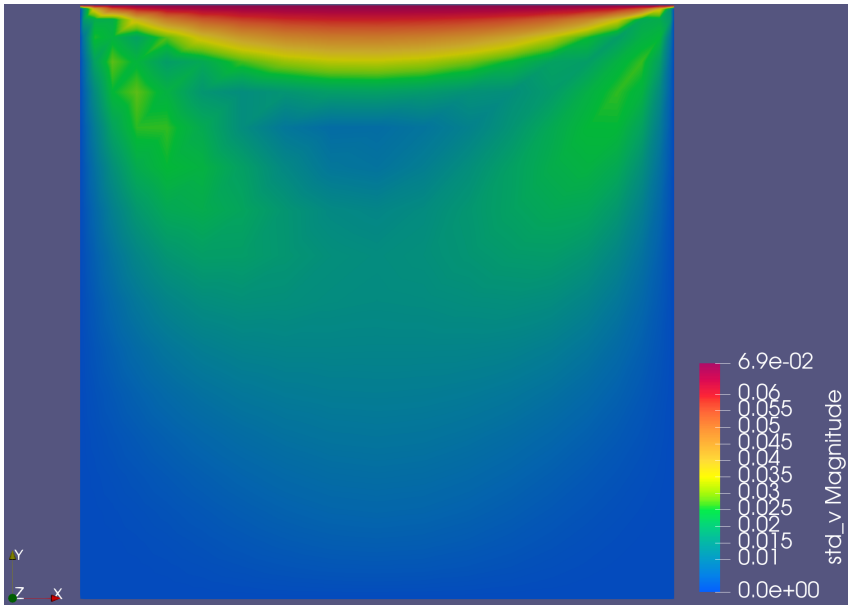

(a) $Re = 100$

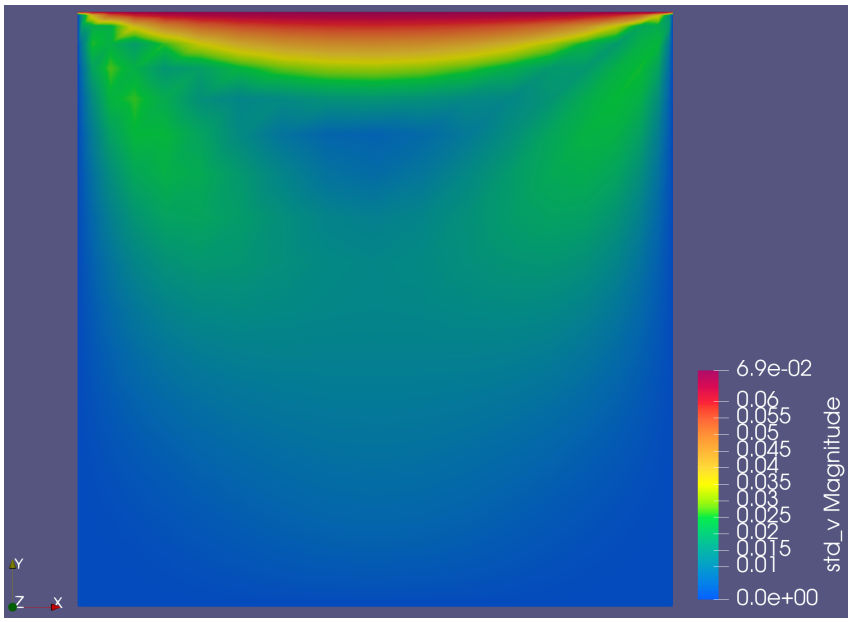

(b) $Re = 400$

Figure 4.6: Standard deviation of velocity for the lid-driven cavity

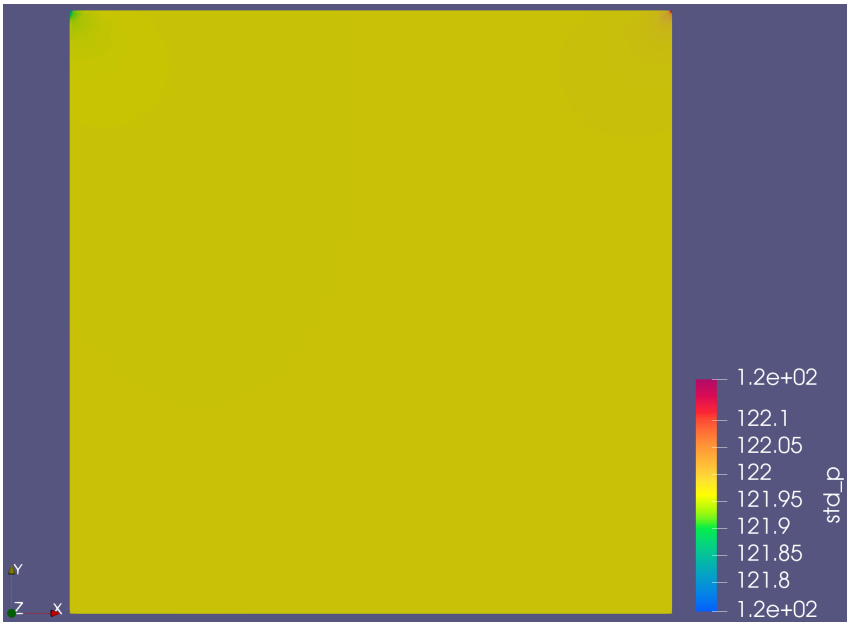

(a) $Re = 100$

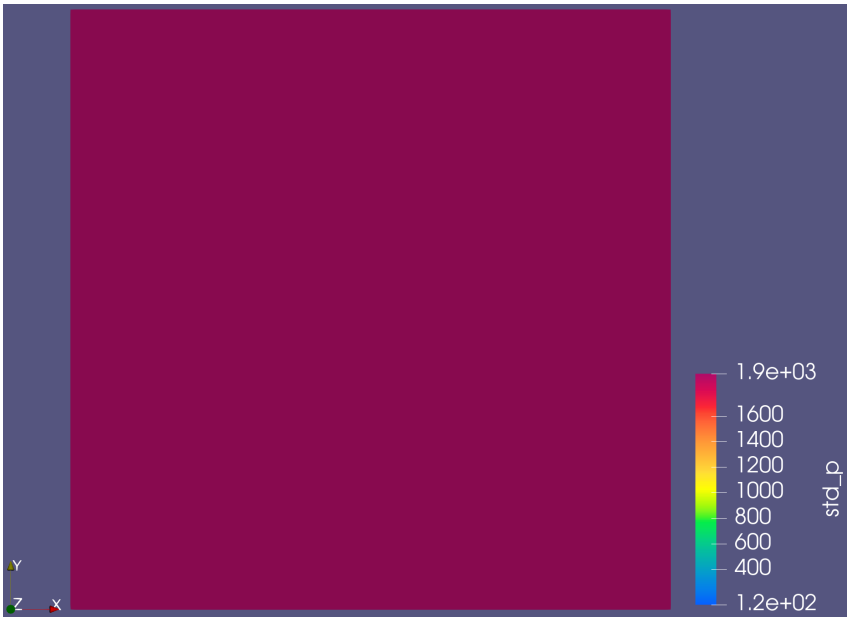

(b) $Re = 400$

Figure 4.7: Standard deviation of pressure for the lid-driven cavity

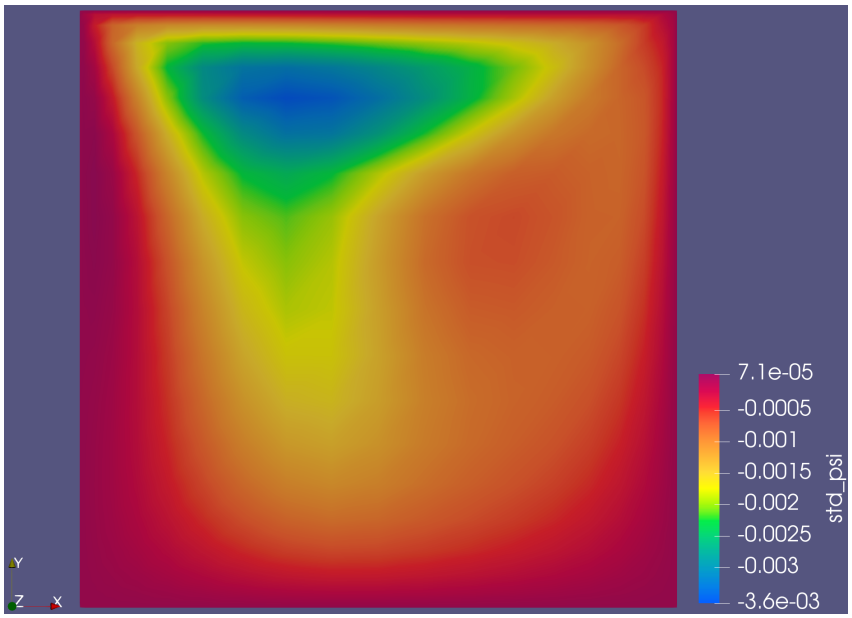

(a) $Re = 100$

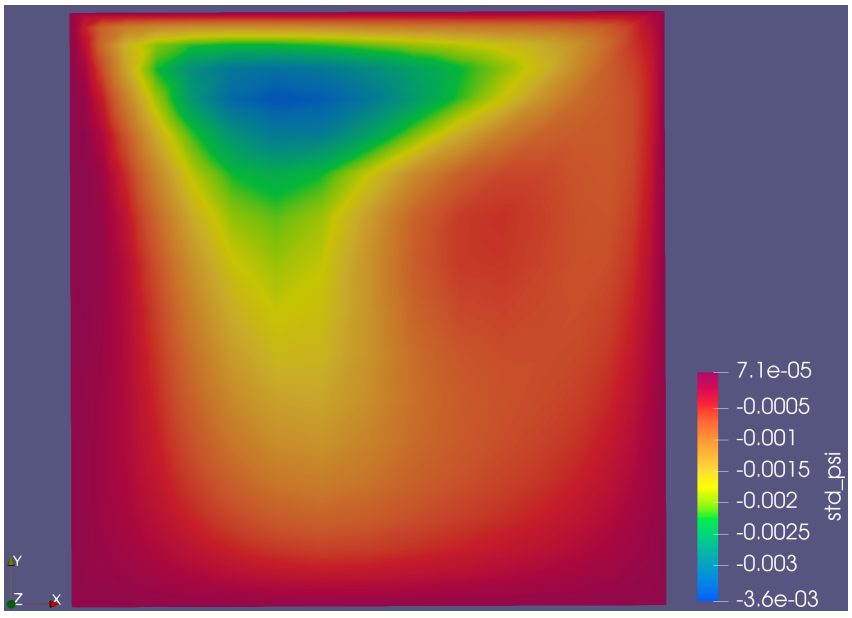

(b) $Re = 400$

Figure 4.8: Standard deviation of streamfunction for the lid-driven cavity

By comparing the plots of Figures 4.6a - 4.8b, we can recognize the regions with the higher fluctuations for each quantity from the mean value. The velocity standard deviation plot may indicate moderate variability, however, significant uncertainty is observed near the top boundary of the domain. This means that although the flow is relatively stable throughout the domain, the interaction with the lid introduces increased uncertainty to the velocity field. On the other hand, the pressure distribution seems to be uniform, as it is seen by the consistent color throughout the computational domain, with uncertainty being decreased by increasing the Reynolds number. This could be linked to stronger unsteady phenomena for lower Reynolds numbers. Lastly, particularly interesting can be the streamfunction contour plots that showcase the variations of the overall flow behavior, with the lower standard deviation values being concentrated in the position of the main vortex.

4.1.3 Code Convergence

A particularly important part of the post-processing of the simulation results is the examination of the code convergence. The convergence rate of the code is visualized by graphs showing the curves of the residual norm as a function of the number of iterations performed by the code until convergence.

The residual norm is a measure of the convergence of the numerical solution to the solution corresponding to the steady state. The smaller the value of the residual norm, the faster the code converges.

As it is illustrated in Figure 4.9, higher Reynolds numbers result to slower convergence. This phenomenon can be explained by the increase in the complexity of the flow at higher Reynolds numbers. Moreover, the flow becomes not only more complex but also more unstable, with stronger recirculations.

Such diagrams prove useful for outlining the flow behavior under different conditions and adjusting various parameters according to the simulation requirements, such as time step and mesh density. Additionally, they provide information on the efficiency of the solver, especially in more complex flow conditions.

A comparison of the two plots presented in Figure 4.9 for the cases $Re = 100$ and $Re = 400$ reveals a clear difference in their respective curves, in terms of the number of iterations required for code convergence. In particular, the number of iterations increases significantly with increasing Reynolds number. The more stable conditions prevailing in the initial case result in a more rapid convergence.

The plots are generated specifically for the benchmark case with the objective of testing and evaluating the capabilities of the code and its sensitivity to changes in the parameters characterizing the problem. As evidenced in the above analysis, changes to the problem parameters have a considerable impact on the convergence of the code. This should be taken into consideration when adapting and applying the code to more complex problems, such as *flow simulation around a NACA airfoil*, which is the key focus of this thesis.

4.2 NACA Airfoil Simulation

4.2.1 Simulation Parameters

In this thesis, uncertainty quantification was performed both on different types of NACA airfoils and for different flow conditions, i.e. different Reynolds numbers.

It is important to consider that different airfoil geometries, from completely symmetrical, such as NACA 0012, to highly cambered airfoils, such as NACA 4412. In this way, the influence of the shape of the airfoil on the occurrence of uncertainties can be investigated. In addition, the wide range of Reynolds numbers ($10^3 - 10^7$) allows the study of flows from laminar, to flows exhibiting fully developed turbulent flow.

For each of the possible combinations of *airfoil type* - *Re number*, the mean value and standard deviation of certain flow characteristics: velocity, pressure, and streamfunction are calculated. The mean value plots illustrate the behavior of the flow, while the standard deviation is a measure of uncertainty in the flow fields.

The cases for which tests were performed are presented in Table 4.3.

4.2.2 NACA Airfoil Results - Mean Contour Plots

In this subsection, the results of the simulations carried out for symmetric and cambered airfoils are presented. For the purpose of clarity, only two of the examined cases mentioned in the Table 4.3 are shown and compared:

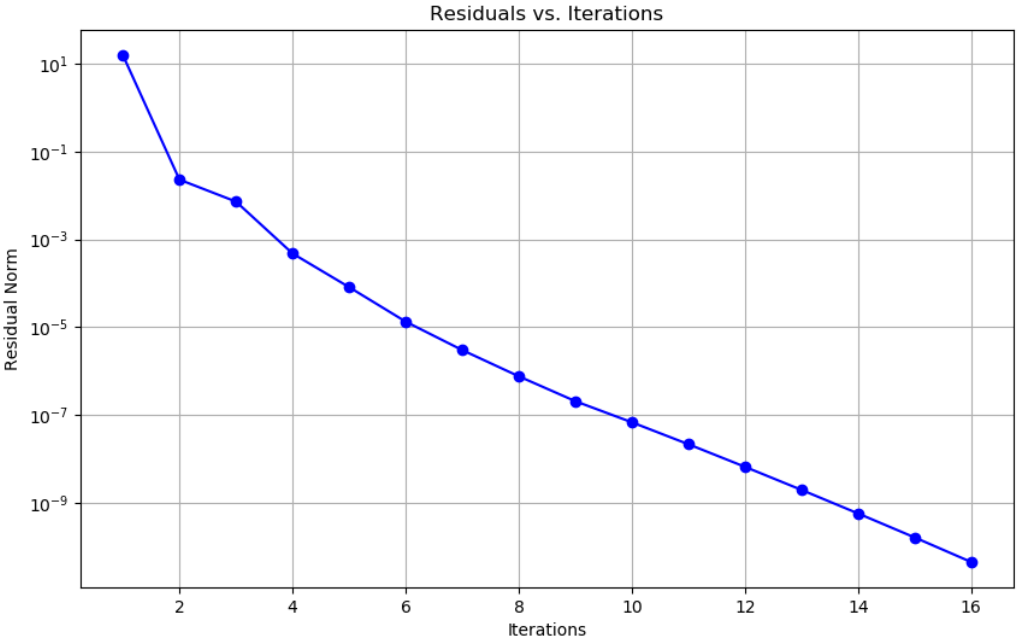

(a) $Re = 100$

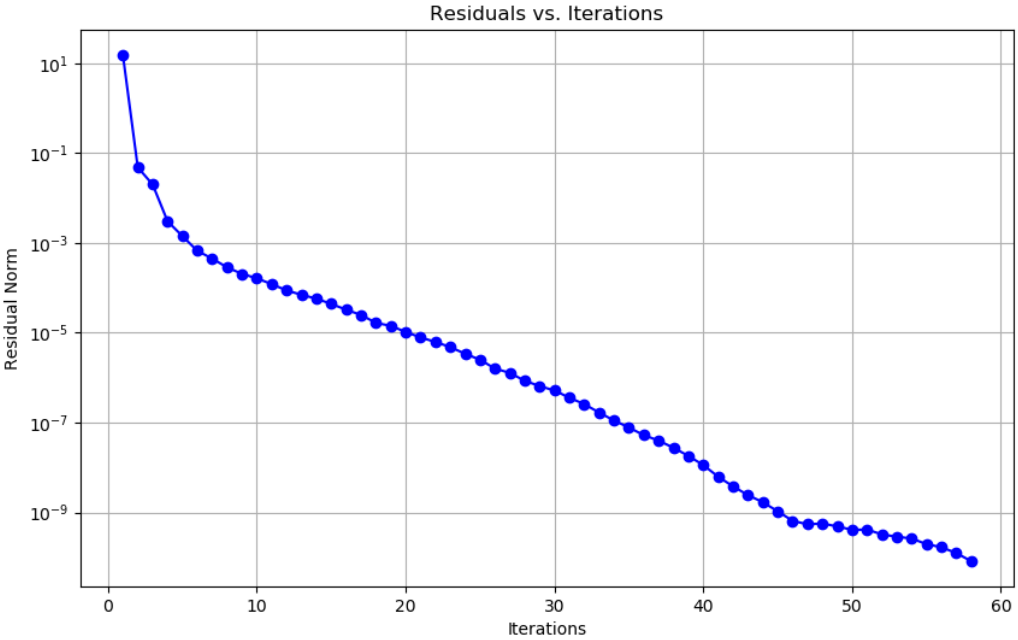

(b) $Re = 400$

Figure 4.9: Code convergence

NACA Airfoil Type	Reynolds Numbers (Re)
NACA 0012	1,000
NACA 2412	10,000
NACA 4412	100,000
	1,000,000
	10,000,000

Table 4.3: Test cases for NACA airfoils and reynolds numbers

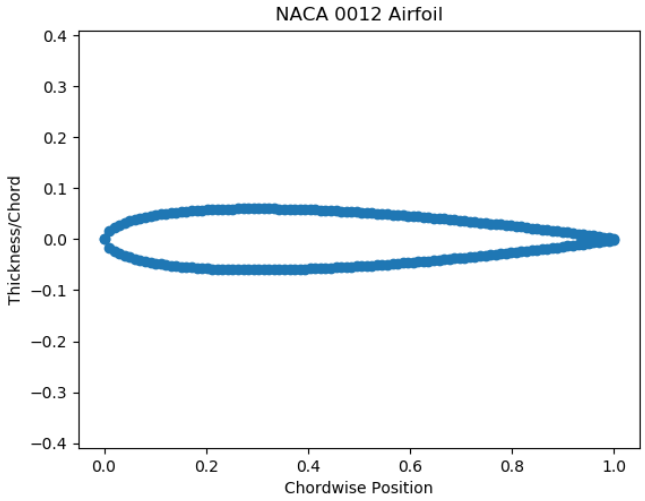

Figure 4.10: Geometry of NACA 0012 airfoil

- The laminar flow case, $Re = 10^3$, and
- The turbulent flow case, $Re = 10^7$

The remaining results are presented in Appendix A.

Symmetric Airfoil

The symmetric airfoil on which uncertainty quantification was performed is NACA 0012. Its shape is shown in Figure 4.10. It is included among the most widely used airfoil types for aerodynamic studies because of its simple geometry. NACA 0012 was studied for various Reynolds numbers to evaluate its behavior and the effect of imposed conditions on velocit and pressure.

Mean distributions for NACA 0012

The mean contour plots are a way of representing the average flow behavior around the NACA airfoil. By examining the mean distributions, we extract information about the regions of high or low velocities and pressures, as well as the streamline patterns.

Mean velocity contour plots

Figures 4.11a and 4.11b show the plots of the average velocity for each of the aforementioned Reynolds numbers. In the centre of the figure, the shape of the airfoil is visible, which is considered to be a solid geometry. The different colours in this graph represent different flow velocity values, as indicated by the colour bar at the bottom of the figure. Based on these colourings, the lowest, up to zero, velocity values are observed near the surface of the airfoil, and as we move away from it, the velocity increases until it reaches the free-flow velocity value.

Around the surface of the airfoil, the boundary layer is observed. In addition, the wake region is observed behind the trailing edge of the airfoil, which implies a reduced velocity with respect to V_∞.

Mean pressure contour plots

Another particularly useful type of graph is the contour plots of mean pressure. These types of plots provide information on how the pressure varies within the computational domain. As in the case of mean

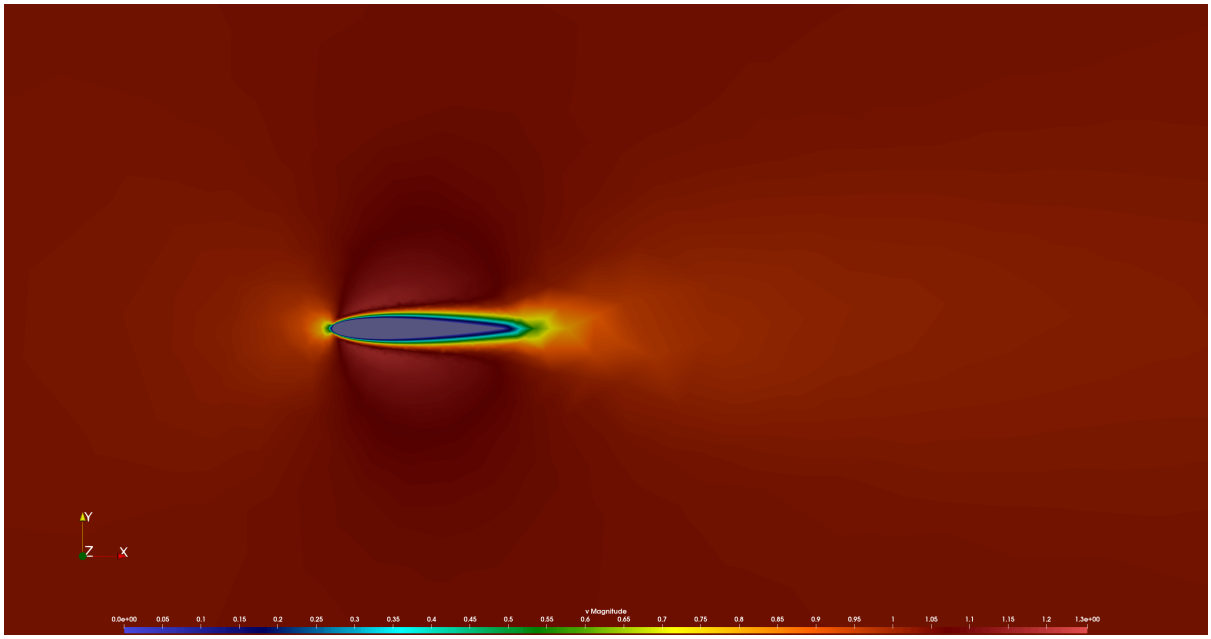

(a) $Re = 10^3$

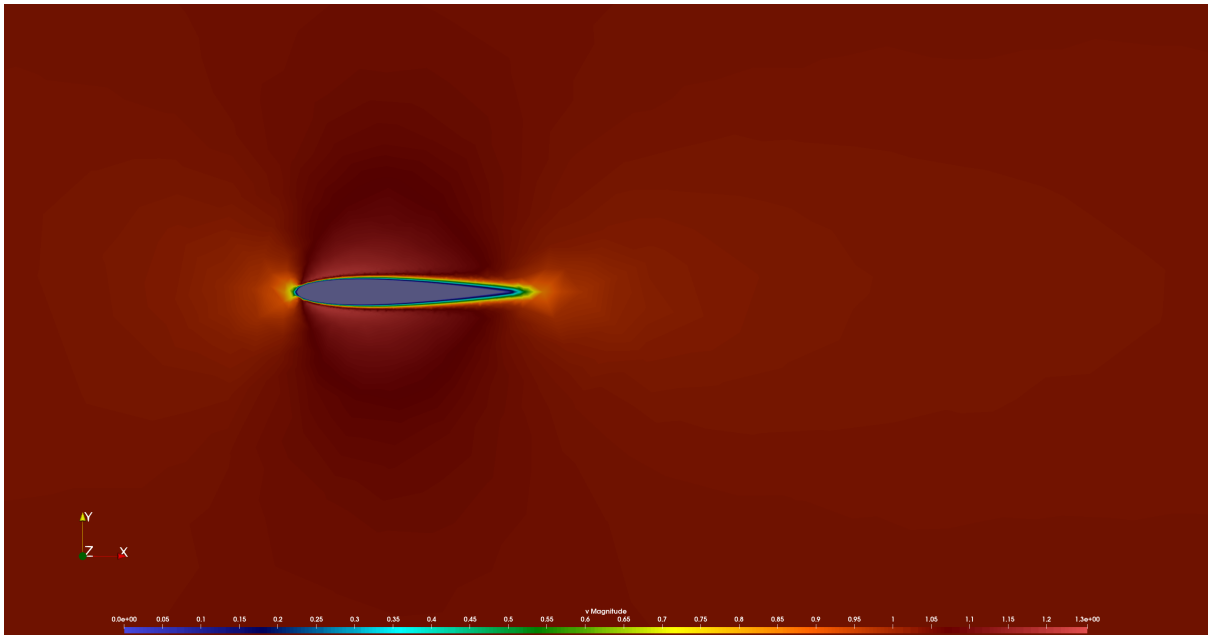

(b) $Re = 10^7$

Figure 4.11: Velocity magnitude contour plot around a NACA 0012 airfoil

velocity contour plots, the size of the corresponding pressure plots is determined by the colors of the color bar at the bottom of the plots.

The pressure distribution has a significant influence on the generation of aerodynamic forces and, in particular, lift. Graphs 4.12a and 4.12b show the pressure distribution around a NACA 0012 airfoil for Reynolds numbers 10^3 and 10^7. When examining these charts, it is wise to focus on two key elements: the **stagnation point** and **the wake region**.

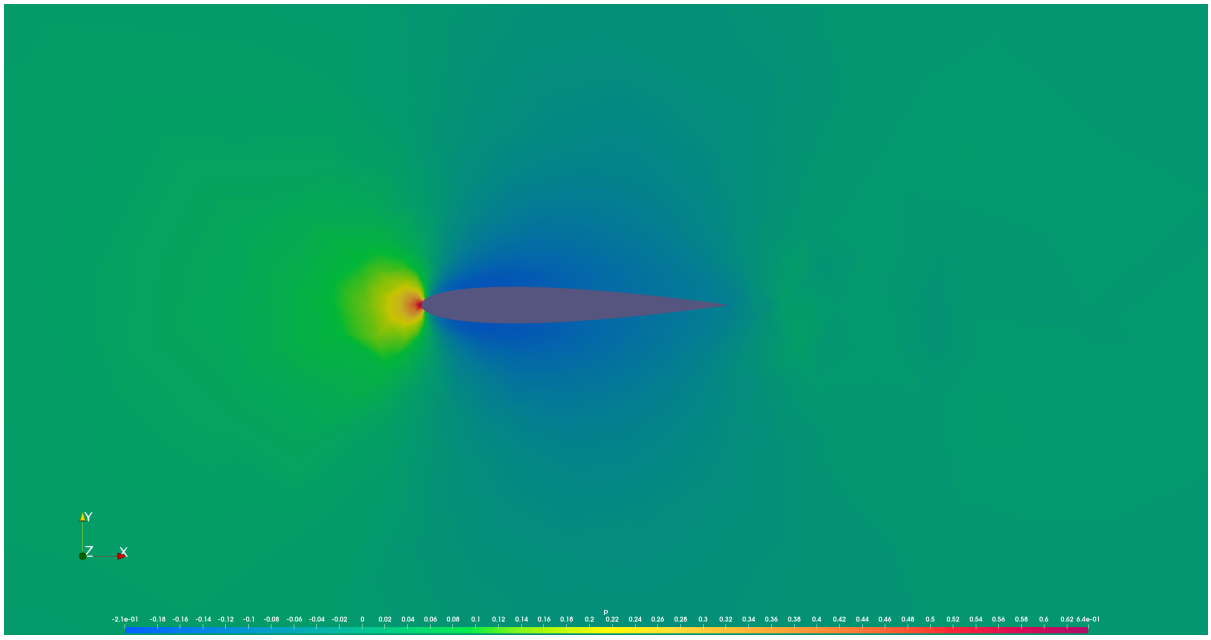

(a) $Re = 10^3$

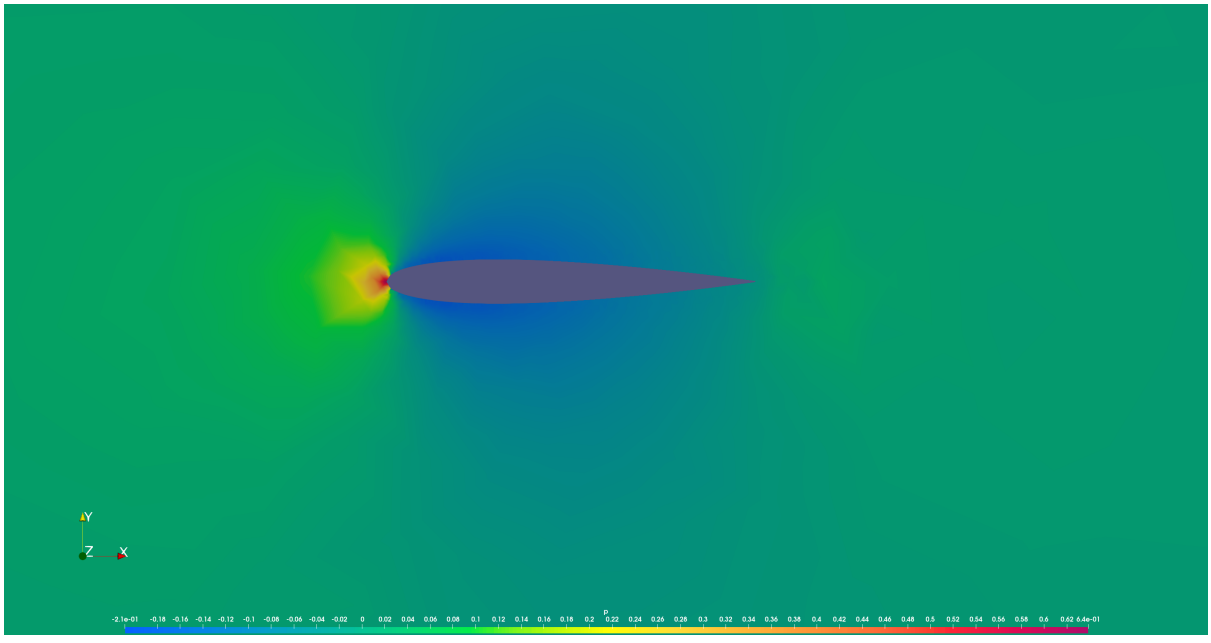

(b) $Re = 10^7$

Figure 4.12: Pressure magnitude contour plot around a NACA 0012 airfoil

Cambered Airfoils

The next stage in the tests conducted is to study the flow behavior around two commonly used cambered airfoils: the NACA 2412 (**??**), and the NACA 4412 (4.13).

In general, cambered airfoils are used in applications where higher lift is required. The asymmetry

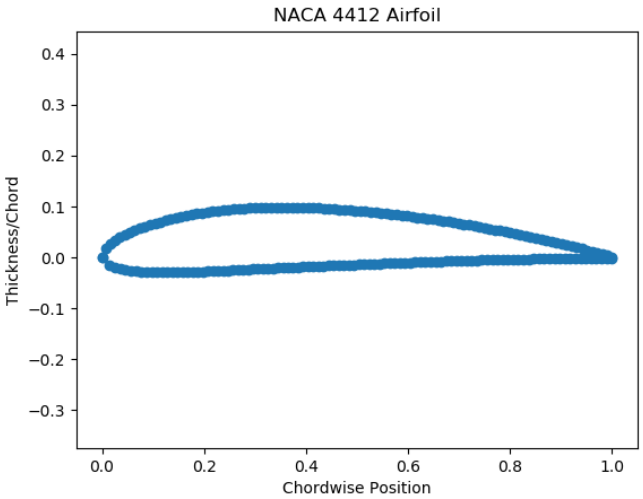

Figure 4.13: Geometry of NACA 4412 airfoil

that characterizes the geometry of these airfoils, unlike symmetrical airfoils, facilitates the generation of lift, even at zero angle of attack.

The contour plots relating to this type of airfoil are presented in the figures 4.14a to 4.15b.

Mean distributions for NACA 2412

The NACA 2412 airfoil is a moderately curved airfoil (with a curvature of 2% of the string length). From the results of the simulations, it is expected that conditions for generating moderate lift at low angles of attack are met. In addition, flow separation occurs earlier than in symmetric airfoils. Figures 4.14a - 4.15b show the distributions of mean velocity and pressure, respectively.

Mean velocity contour plots
See Figures 4.14a and 4.14b.

Mean pressure contour plots
See Figures 4.15a and 4.15b.

Mean distributions for NACA 4412

NACA 4412 has a higher percentage of camber (4%) than NACA 2412. Such airfoils are used in applications of increased lift, such as in slow-flying aircraft and some propellers. This increased lift is the result of the pressure difference between the upper and lower surfaces of the airfoil. Also, the separation of the flow is more prominent than in the case of airfoils with a smaller camber. The mean velocity an pressure contour plots relating to this type of airfoil are presented in the figures ?? - ??.

Mean velocity contour plots
See Figures 4.16a and 4.16b.

Mean pressure contour plots
See Figures 4.17a and 4.17b.

4.2.3 Uncertainty Quantification Results

This section presents the basic diagrams from which the quantification of uncertainty is obtained. The standard deviation contour plots provide information on the variation and uncertainty within the computational domain and help the analyst to identify the areas that are most sensitive to changes in flow conditions and also in the geometry of the airfoil. In particular, the cases that are analyzed are the same as those in the 4.2.2 section.

The contour plots of the standard deviation are analyzed and compared with those of the mean value of the flow characteristics. Typically, areas of high standard deviation are shaded in warmer colors, indicating a larger deviation of the magnitude from the calculated mean. This study is particularly important for assessing the behavior of various airfoils under different conditions.

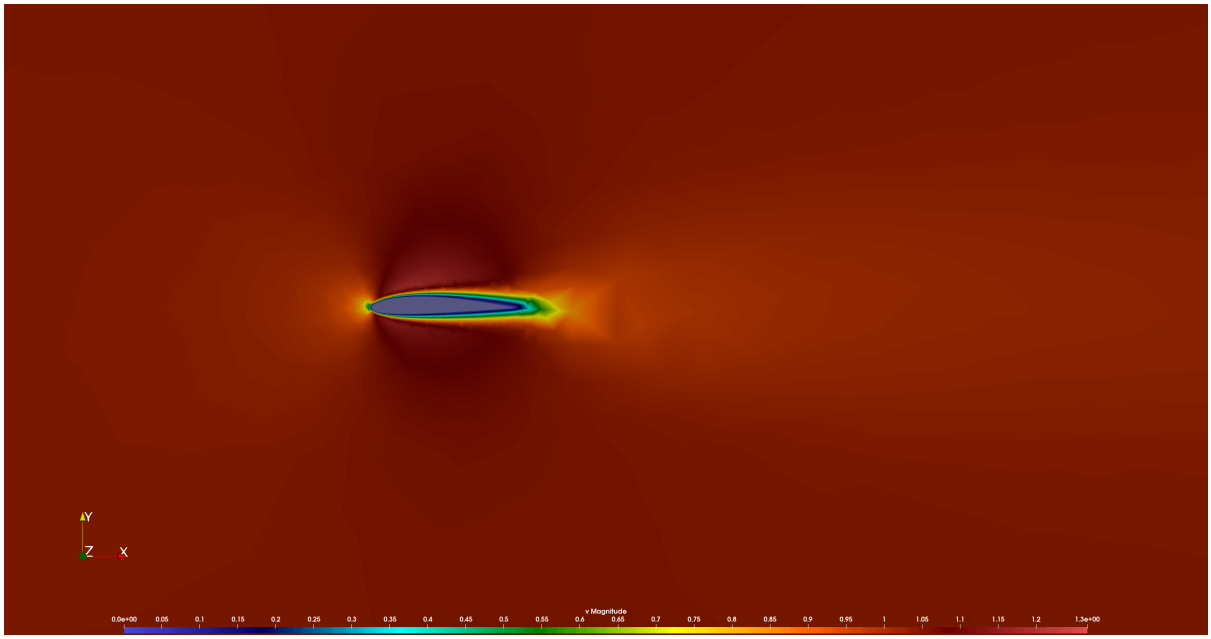

(a) $Re = 10^3$

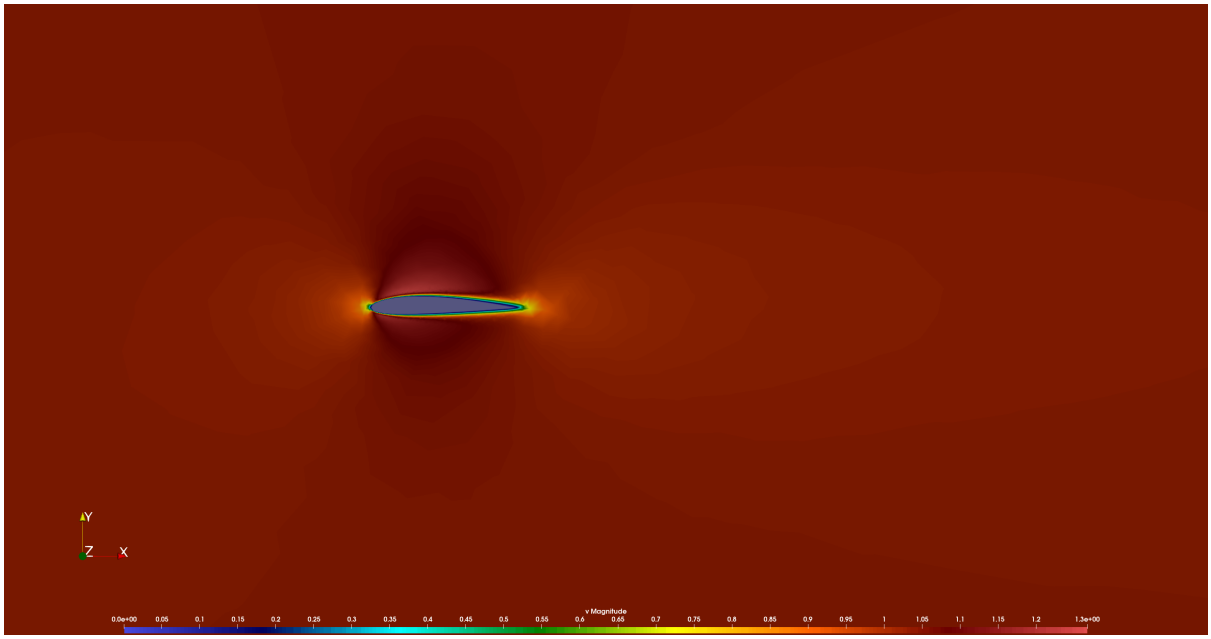

(b) $Re = 10^7$

Figure 4.14: Velocity magnitude contour plot around a NACA 2412 airfoil

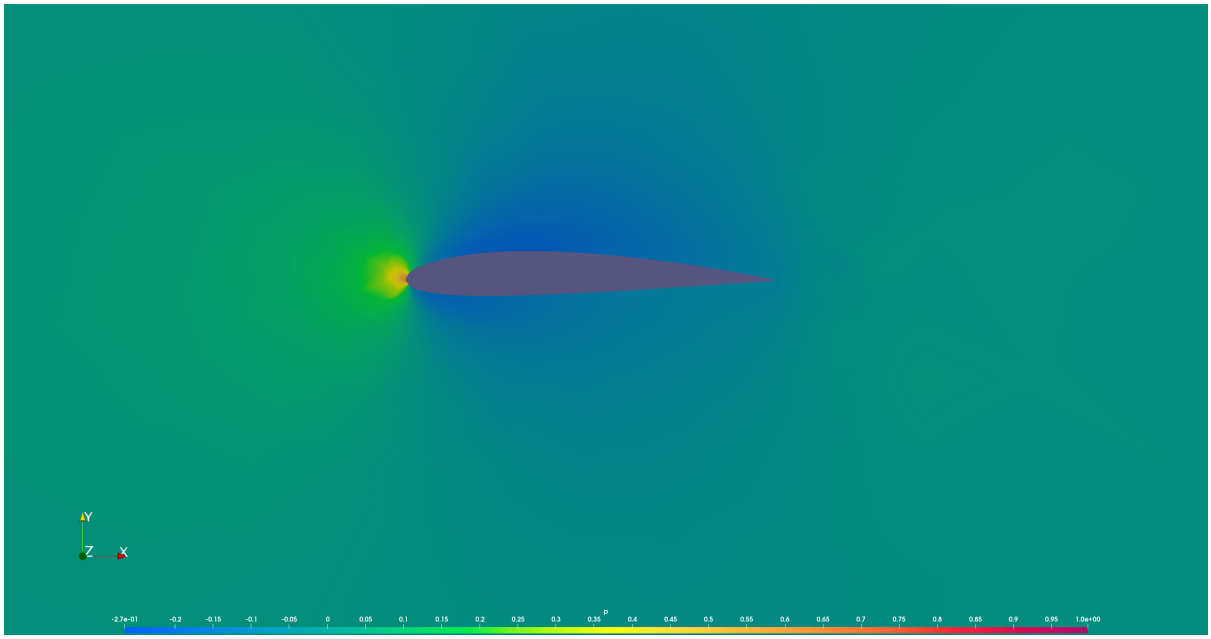

(a) $Re = 10^3$

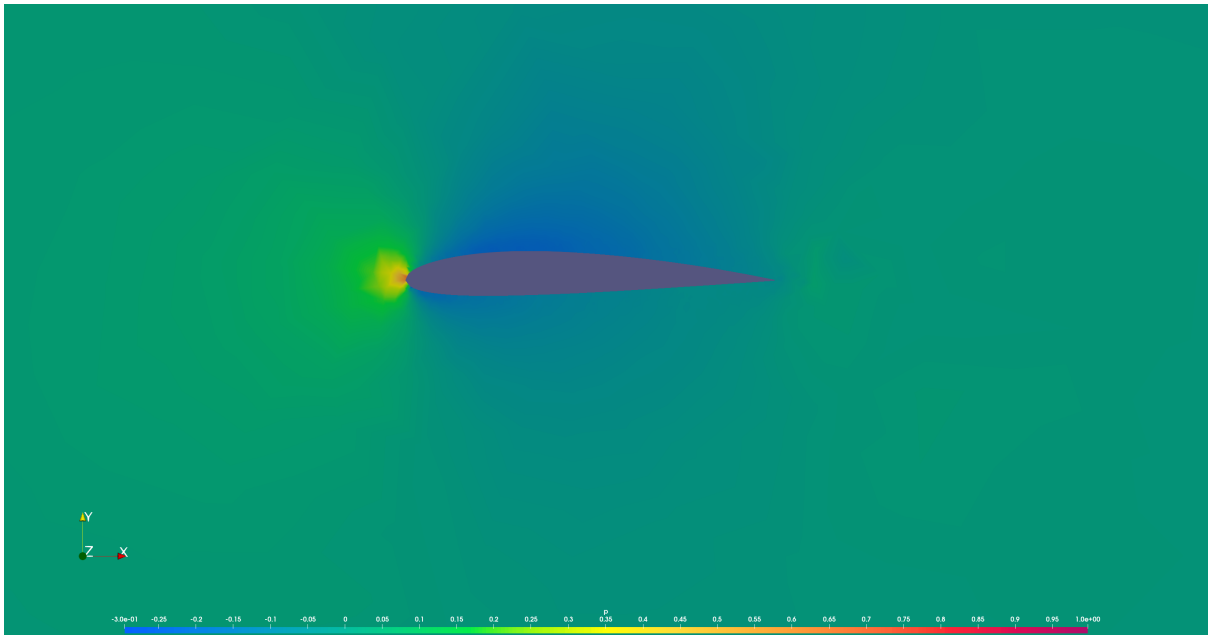

(b) $Re = 10^7$

Figure 4.15: Pressure magnitude contour plot around a NACA 2412 airfoil

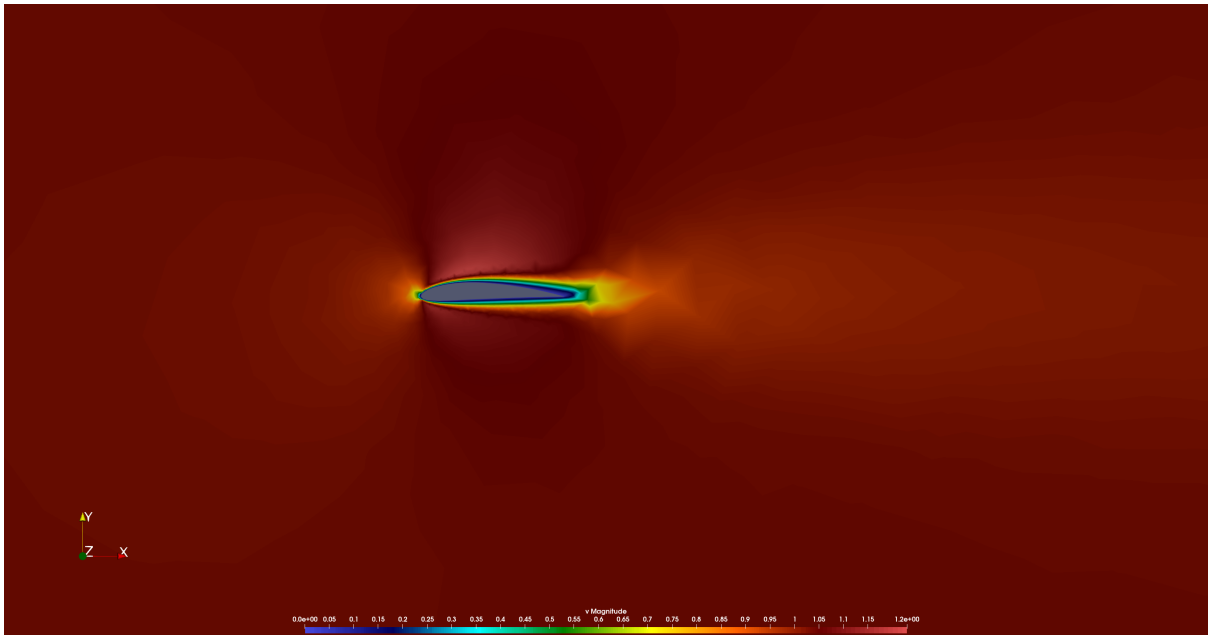

(a) $Re = 10^3$

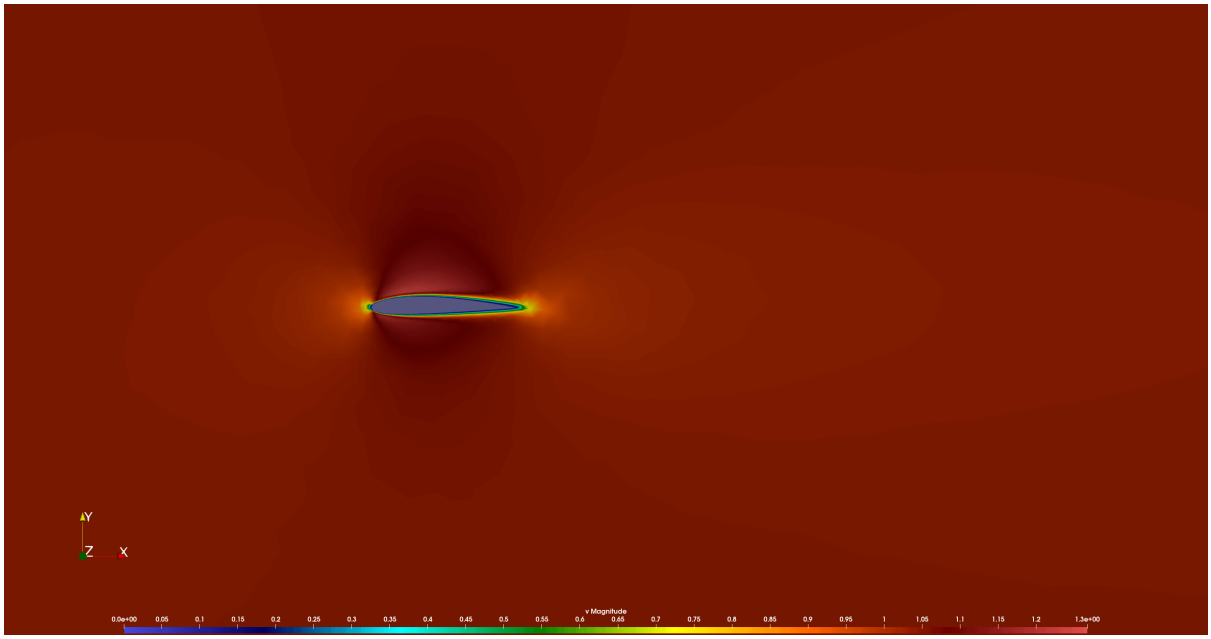

(b) $Re = 10^7$

Figure 4.16: Velocity magnitude contour plot around a NACA 4412 airfoil

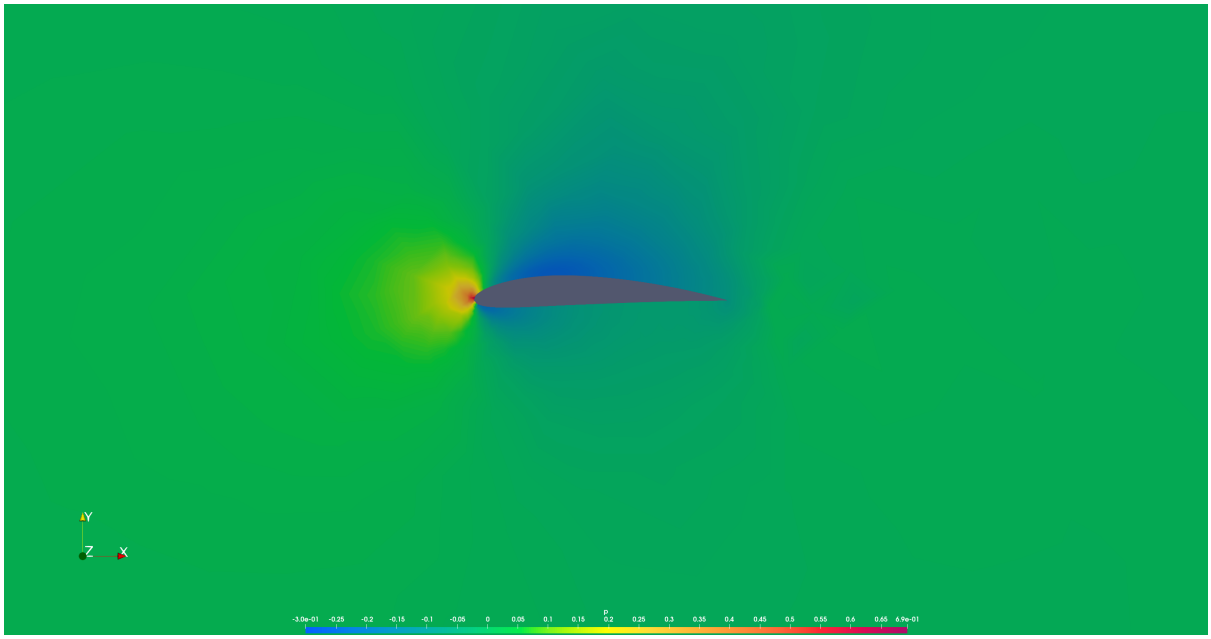

(a) $Re = 10^3$

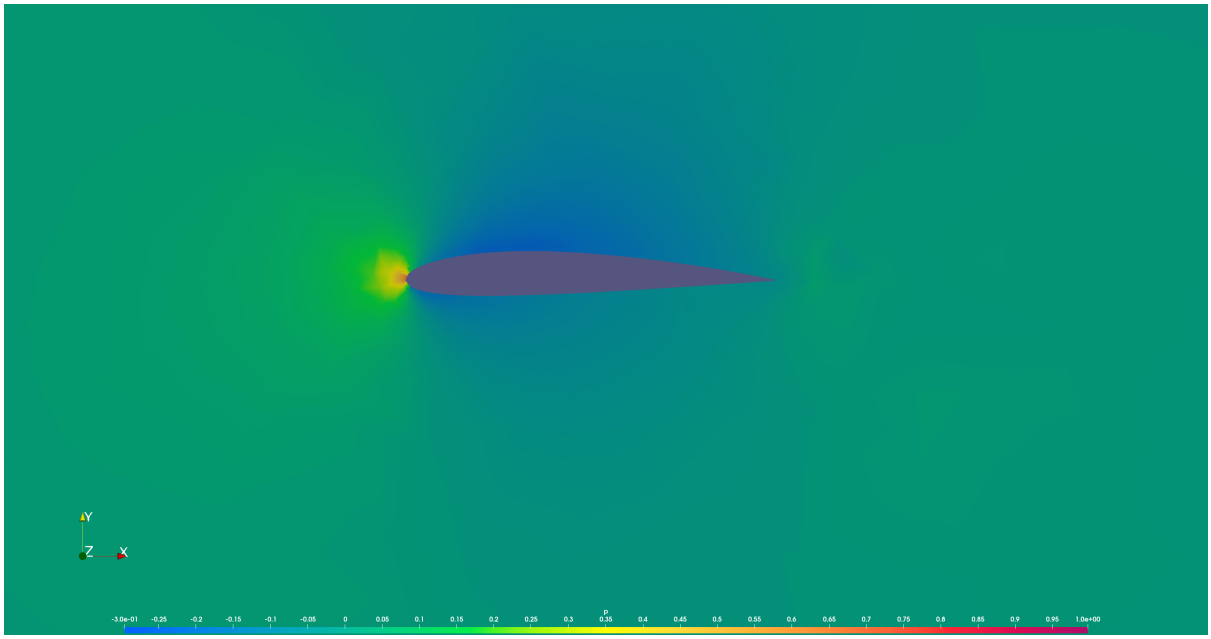

(b) $Re = 10^7$

Figure 4.17: Pressure magnitude contour plot around a NACA 4412 airfoil

Standard Deviation Contour Plots - Velocity

The contour plots of the standard deviation of velocity show the variability of the velocity field within the computational domain. The areas with the largest standard deviation are also associated with the largest uncertainty due to changes in the input parameters. Key areas that should be given special attention when quantifying uncertainty are the two edges of the airfoil, the leading and trailing edge, and the wake region, due to the unsteady phenomena that develop, such as flow separation, turbulence, etc.

NACA 0012

See Figures 4.18a and 4.18b.

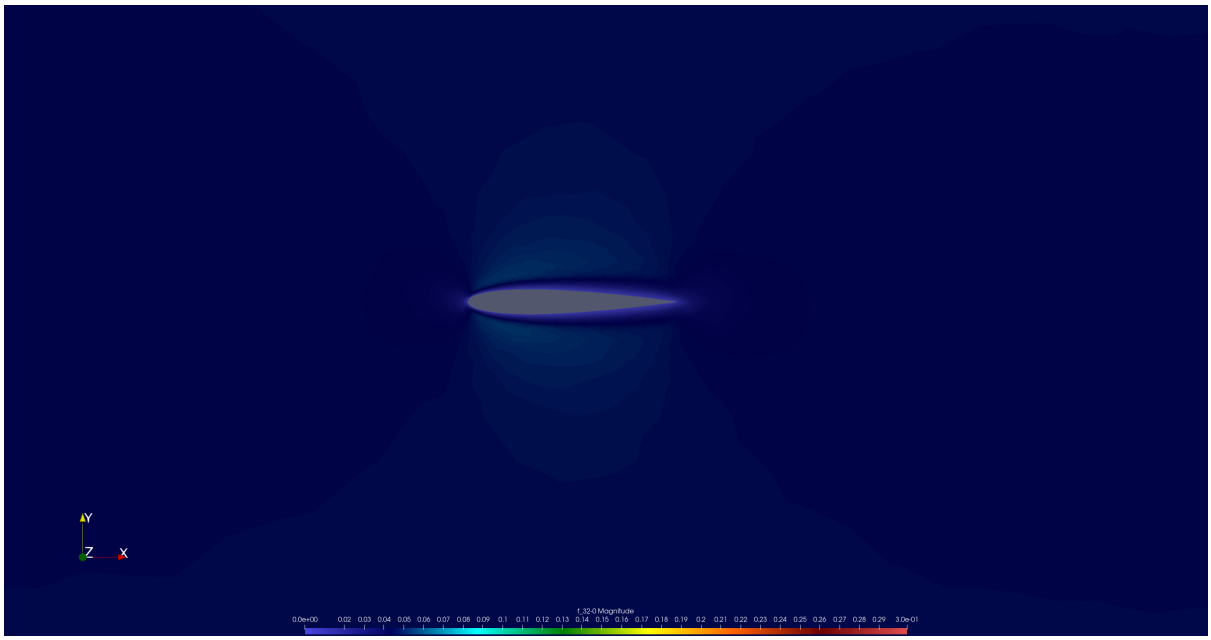

(a) $Re = 10^3$

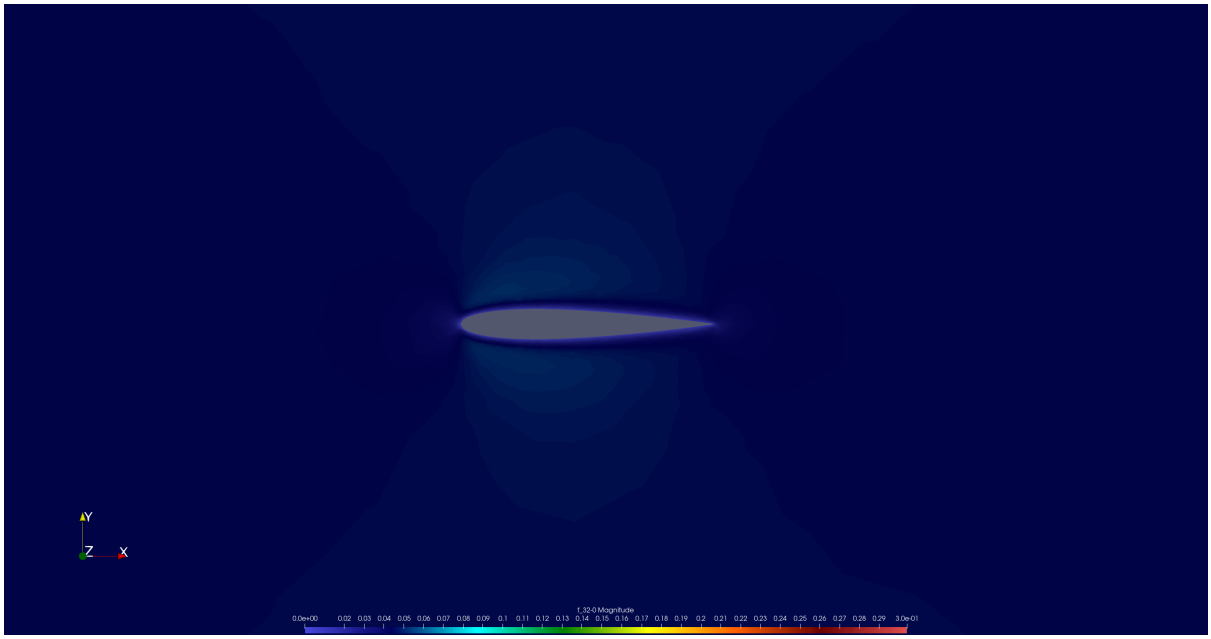

(b) $Re = 10^7$

Figure 4.18: Standard deviation of velocity contour plot for a NACA 0012 airfoil

NACA 2412

See Figures 4.19a and 4.19b.

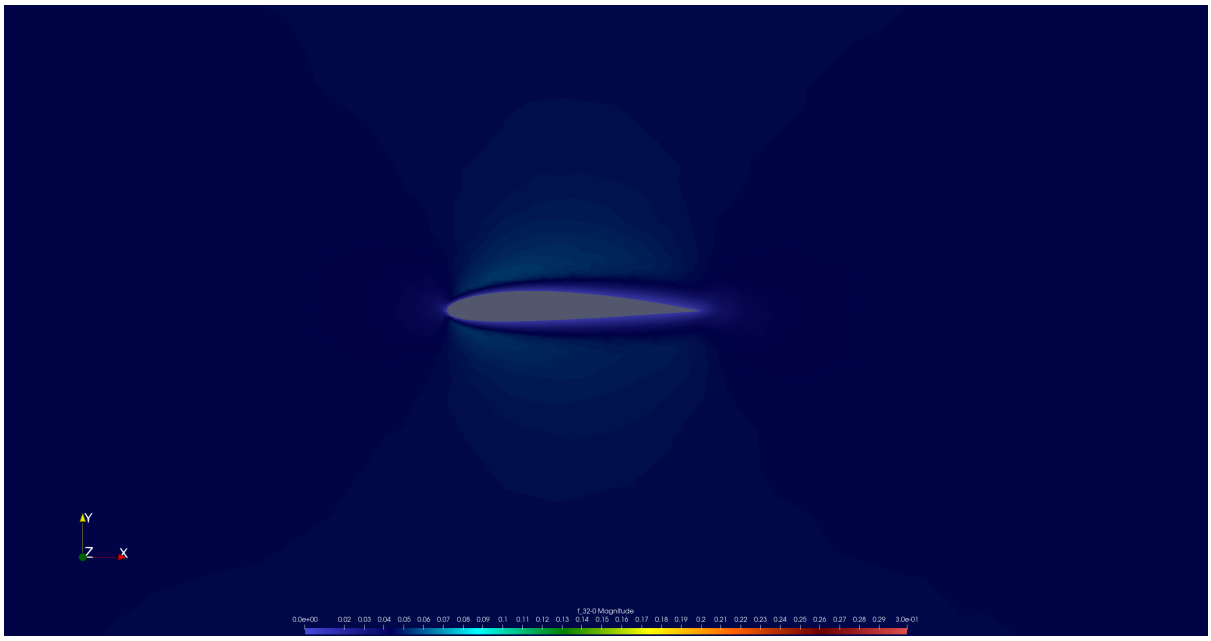

(a) $Re = 10^3$

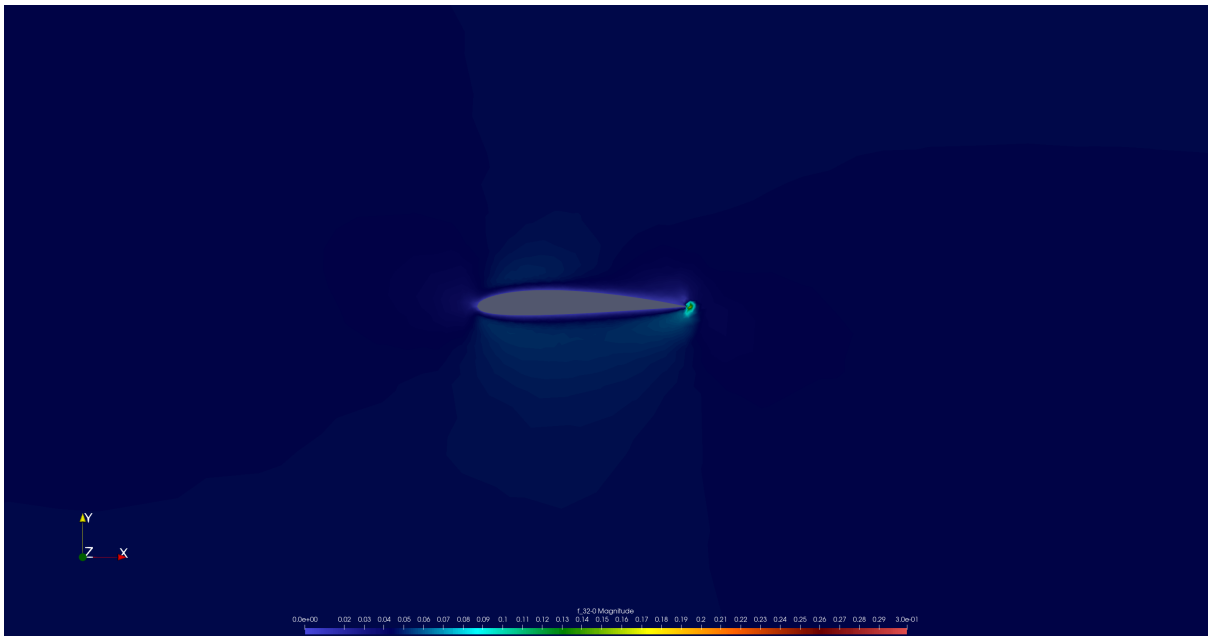

(b) $Re = 10^7$

Figure 4.19: Standard deviation of velocity contour plot for a NACA 2412 airfoil

NACA 4412

See Figures 4.20a and 4.20b.

Standard Deviation Contour Plots - Pressure

The contour plots of the pressure standard deviation reveal, similarly to the velocity standard deviation plots, how the pressure varies in the computational domain. Areas of small standard deviation in these

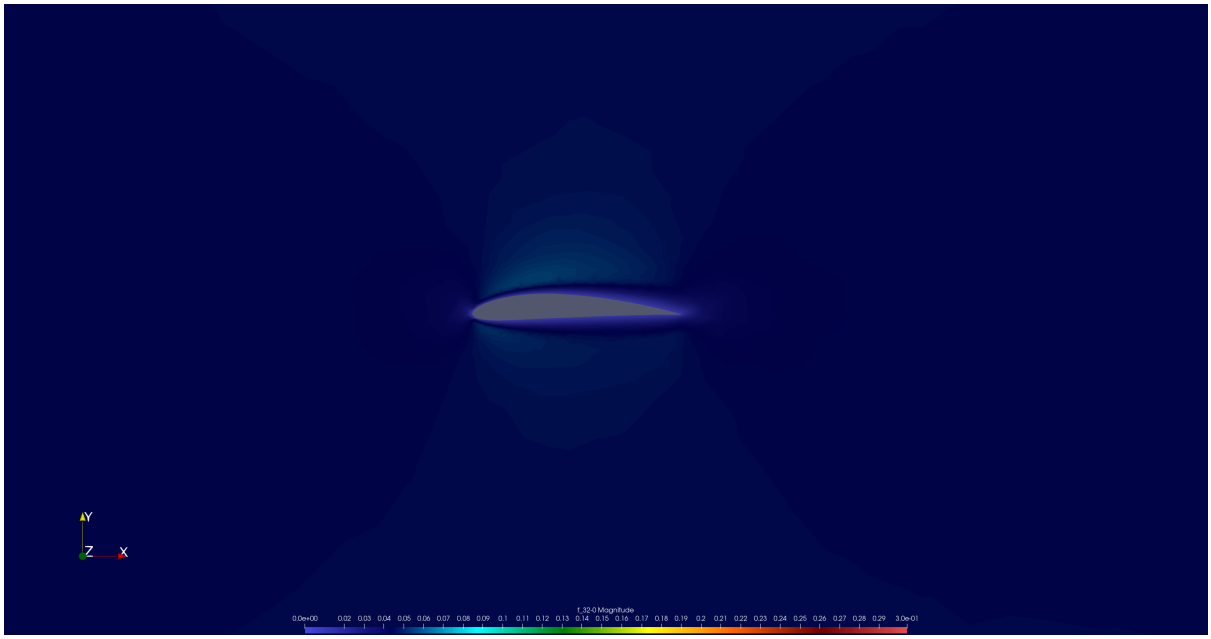

(a) $Re = 10^3$

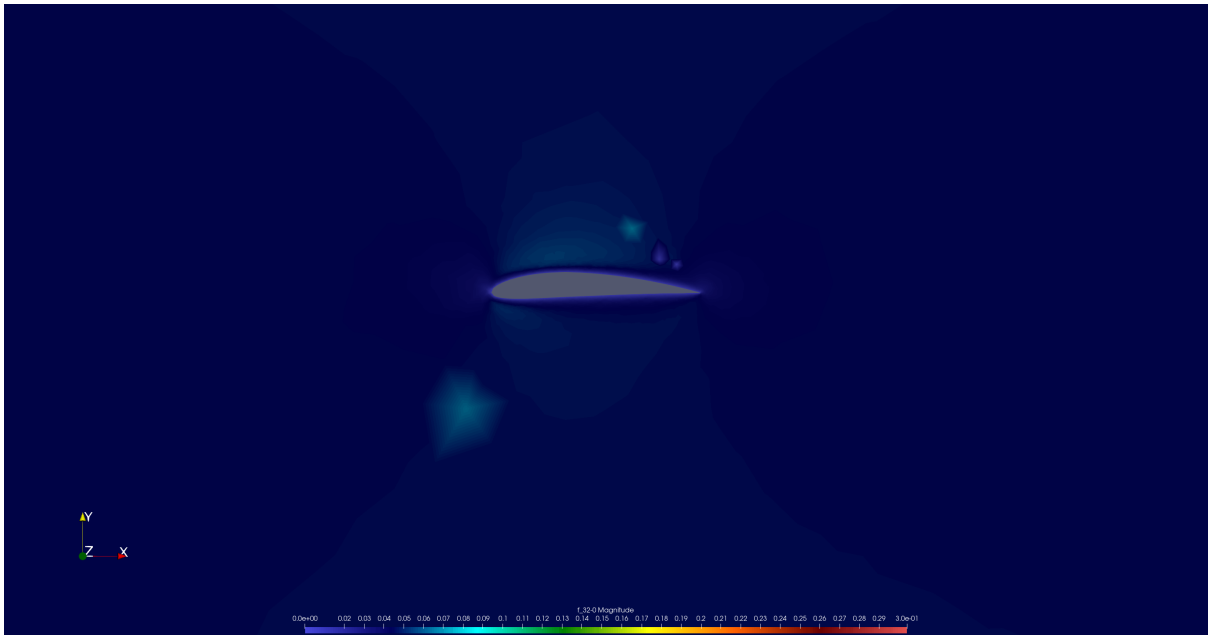

(b) $Re = 10^7$

Figure 4.20: Standard deviation of velocity contour plot for a NACA 4412 airfoil

plots imply stable pressure with small variations. Such phenomena are more pronounced in laminar flows, and the standard deviation increases as the flow becomes more turbulent. Also in these diagrams, the leading edge with the stagnation point and the trailing edge with the wake region play a key role.

NACA 0012

See Figures 4.21a and 4.21b.

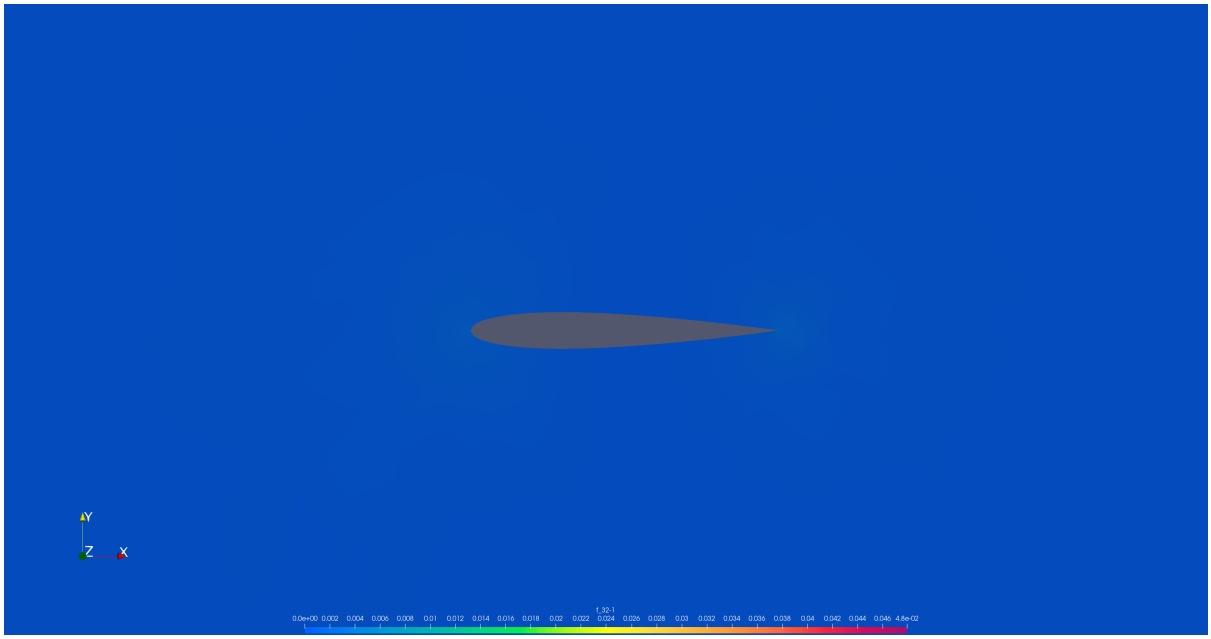

(a) $Re = 10^3$

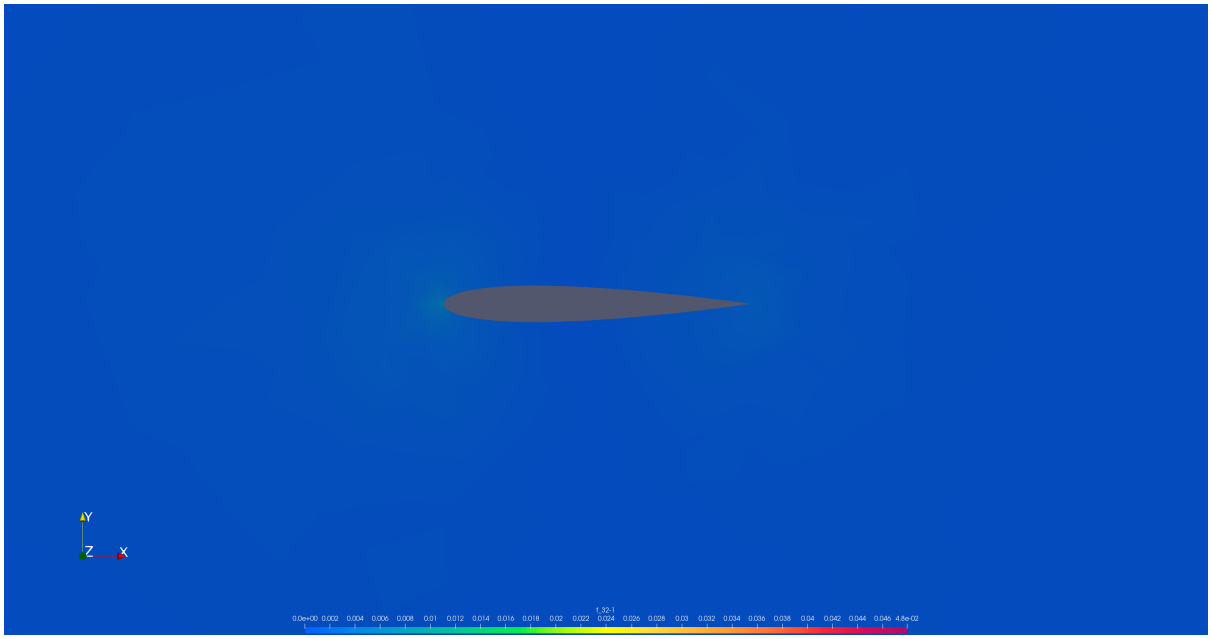

(b) $Re = 10^7$

Figure 4.21: Standard deviation of pressure contour plot for a NACA 0012 airfoil

NACA 2412

See Figures 4.22a and 4.22b.

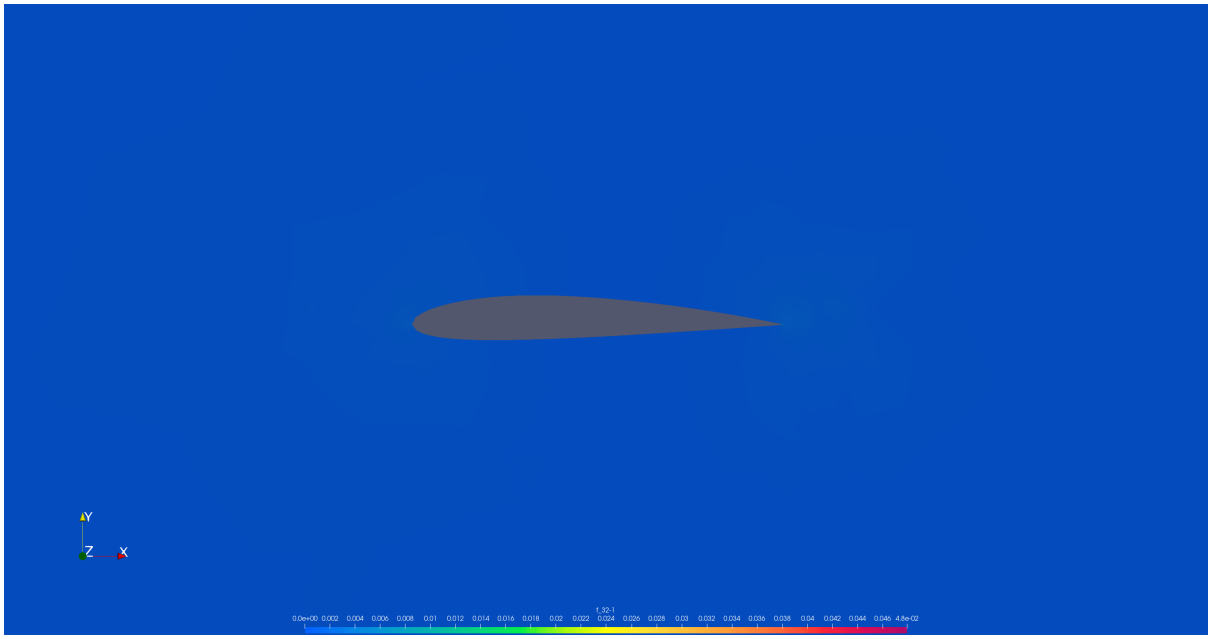

(a) $Re = 10^3$

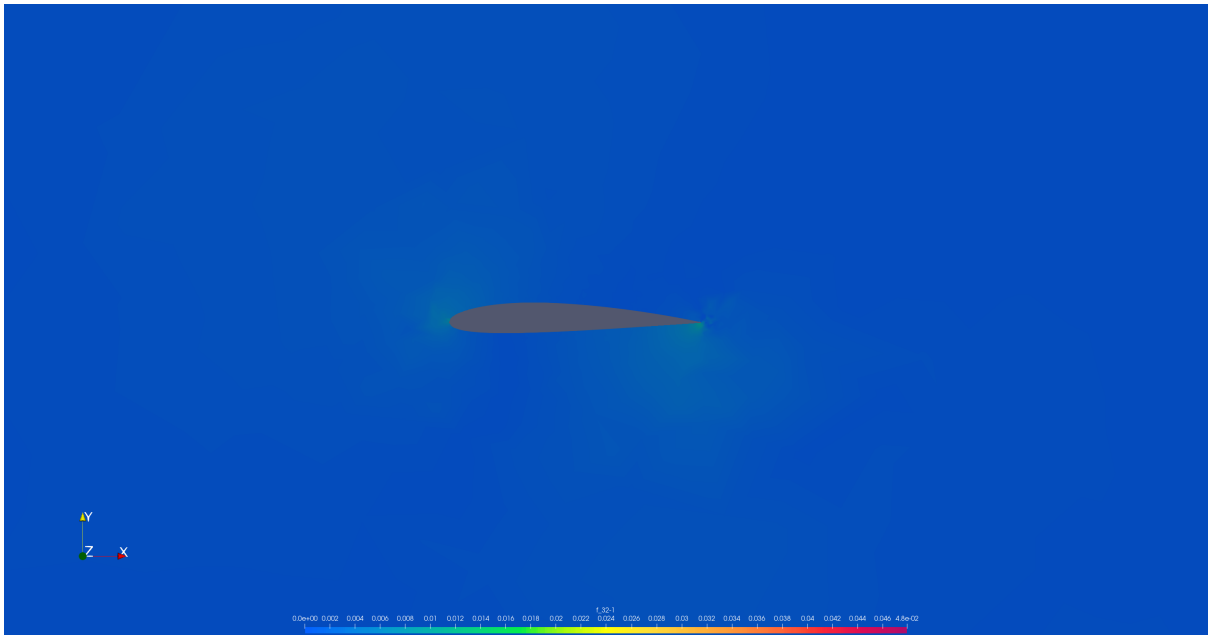

(b) $Re = 10^7$

Figure 4.22: Standard deviation of pressure contour plot for a NACA 2412 airfoil

NACA 4412

See Figures 4.23a and 4.23b.

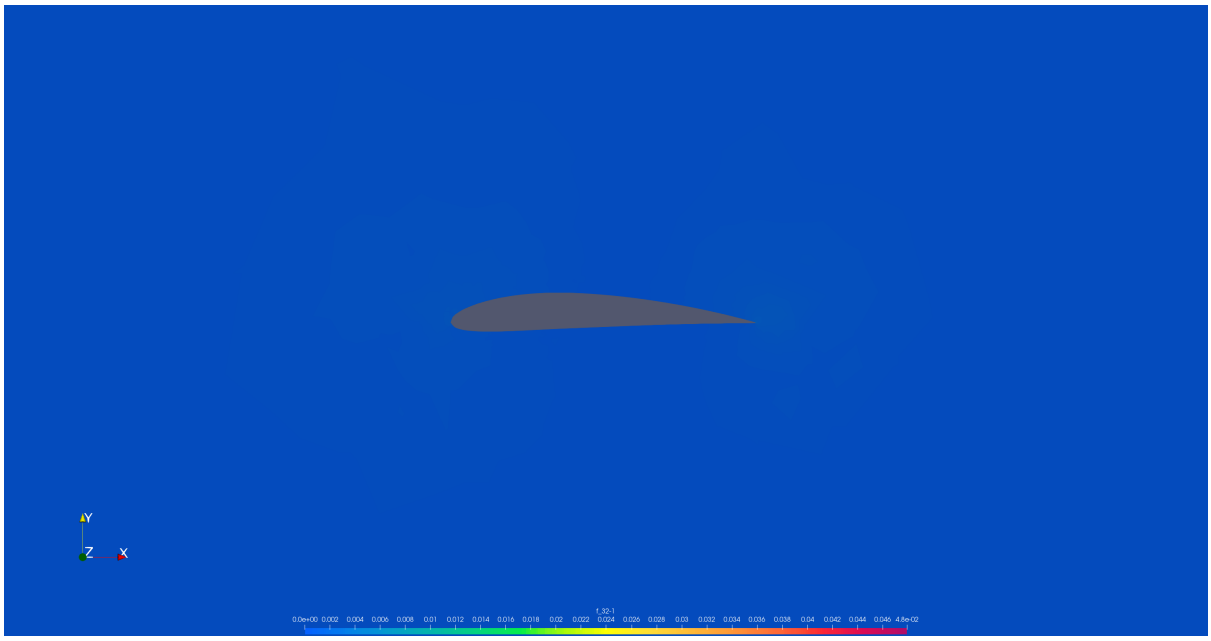

(a) $Re = 10^3$

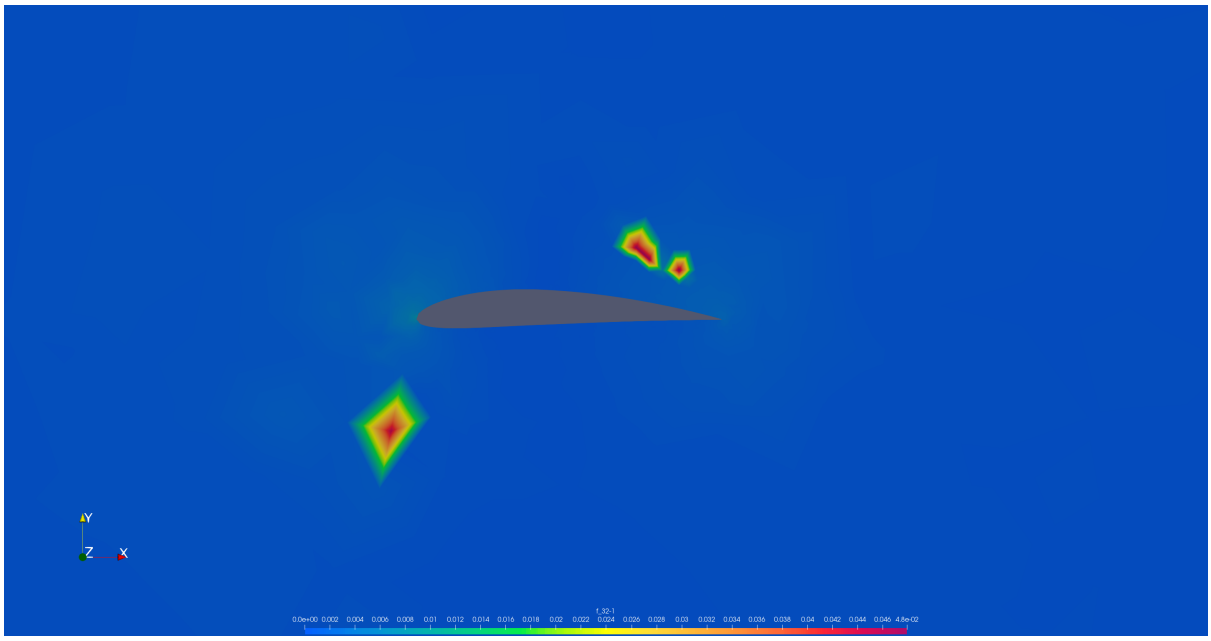

(b) $Re = 10^7$

Figure 4.23: Standard deviation of pressure contour plot for a NACA 4412 airfoil

Chapter 5

Discussion

By examining the individual graphs in figure 4.11, it is beneficial to make a comparison between the two Reynolds number cases. For reduced values of the Reynolds number, the flow is governed by viscous forces. This explains the difference in boundary layer thickness visible between the two graphs, with the boundary layer on the $Re = 10^7$ case being much thinner due to reduced viscous forces. Moreover, in the case of $Re = 10^3$, the wake region appears to be wider compared to the case of $Re = 10^7$ in which this region narrows significantly. A wider wake region is accompanied by stronger viscous effects, which increases the drag force that develops. In inviscid flows, no drag force occurs.

By comparing the graphs 4.15a and 4.15b, we can observe key differences due to the different flow conditions. For both $Re = 10^3$ and $Re = 10^7$, the region of maximum pressure in front of the leading edge of the airfoil is identified. This is the stagnation point, where the flow hits the airfoil head-on and its velocity is minimized. In flows characterized by high Reynolds numbers ($Re = 10^7$), the stagnation point appears to be more localized than in the case of $Re = 10^7$.

In addition, an area of low pressure is visible around the upper and lower surface of the airfoil. These areas indicate an acceleration of the flow due to the shape of the airfoil, creating lift. In the case of the lower Reynolds number, the low-pressure distribution appears to be symmetrical due to the laminar flow and the symmetrical shape of the airfoil in question. However, in the case of turbulent flow, the low-pressure region extends over a larger area of the computational domain. This phenomenon implies a higher flow acceleration and generation of a higher buoyancy force.

Also of interest is the wake region, which provides useful information about the flow behavior around the NACA 0012 airfoil. In Figure 4.15a, the wake occupies a larger area. The wider wake area indicates a more pronounced drag force. In graph 4.15b a narrower wake area is observed. This means that the flow does not separate the airfoil surface as fast as in the case of $Re = 10^3$.

As far as convex airfoils are concerned, there are significant differences in the flow behavior around this type of airfoil compared to symmetrical airfoils.

The contour plots of the mean velocity show that the two airfoils exhibit similar behavior, both for $Re = 10^3$ and $Re = 10^7$. Except for the larger wake region, which is typical for laminar flow, the flow separation occurs earlier than the symmetric airfoils, due to the curvature of the shape of these airfoils. As the Reynolds number increases, so does the lift applied to the airfoil surface. Particularly at high Reynolds numbers, the flow remains attached to the surface for a longer distance before separating, resulting in a thinner wake area, more efficient lift generation, and thus reduced drag and improved aerodynamic performance.

The mean pressure contour plots have as their main component the pressure difference developed between the upper and lower surfaces of the airfoil. In both NACA 2412 and NACA 4412, the pressure developed on the upper surface is significantly lower than on the lower surface. As mentioned, this pressure difference is due to the asymmetry in the geometry of the curved airfoils, giving them the ability to generate lift even at zero angle of attack.

For the uncertainty quantification stage, simulations were performed for the cases in Table 4.3, of which the two extreme cases regarding the Reynolds number are presented and analyzed for the three types of airfoils under consideration, NACA 0012, NACA 2412, and NACA 4412. The contour plots which are obtained for the standard deviation for the velocity and pressure magnitudes provide important information about the presence of uncertainties as the input parameters change.

When observing the plots for the lowest Reynolds number, they appear to be similar due to the steady nature of the flow. For NACA 0012, the plot indicates minimal standard deviation as inferred from the

colorings compared to the corresponding color bar values at the bottom of the graph. In general, the flow appears uniform around the airfoil with small variations in velocity at both ends of the airfoil. By changing the geometry of the airfoil, and introducing camber in its shape, the standard deviation also increases, especially at the trailing edge. The camber causes more complex flow phenomena, especially in the wake region, increasing the presence of uncertainties. This phenomenon is confirmed by the contour plot corresponding to the standard deviation of the flow velocity around NACA 4412. The even higher camber causes more uncertainty at the trailing edge, as higher values of standard deviation values are visible in this region, which also extends for a larger area in the wake region.

As can be seen from the graphs 4.21a to 4.23b, the flow for $Re = 10^7$ follows a similar behavior to the case of $Re = 10^3$, with the change of the geometry of the airfoil under consideration. However, in these cases, the existence of uncertainties is intensified due to the change in the flow conditions determined by the value of the Reynolds number. Consequently, the greatest uncertainty is observed in the case described by Figure 4.23b, as it involves the most complex geometry and turbulent and unsteady flow.

Moving on to the analysis of the plots representing the standard deviation of pressure, one of the first observations is that there are not as significant changes in the pressure field as there were in the velocity field. However, there are key points that are more sensitive to changes in the problem parameters. The graph 4.21a shows a uniform pressure field, as the standard deviation shows little to no variation. This is due to the low Reynolds number and the symmetric shape of the airfoil. A similar picture is seen in the graph 4.21b, indicating that the change in flow conditions introduces significant uncertainties in the solution for this particular airofoil. As for the graphs involving the standard deviation of velocity, the standard uncertainty increases with increasing airfoil curvature and also with increasing Reynolds number. Of particular interest is the case of the graph 4.23b, in which regions of increased standard deviation are observed. This phenomenon is not a result of changing input data, but of the instability that the code exhibits in more complex cases of geometry and flow conditions. One solution to this problem is to further increase the stabilization parameter for the stabilization method applied, SUPG.

In summary, the study presented in the previous chapters provides valuable insight into the aerodynamic characteristics of different airfoil shapes under varying flow conditions, described by the Reynolds number. The importance of the viscosity in shaping flow behavior is clearly highlighted through the mean velocity contour plots, with lower Reynolds numbers resulting in thicker boundary layers and wider wake regions. Therefore, drag is increased. On the contrary, in higher Reynolds numbers the flow is attached to the airfoil surface for longer which contributes to the efficient lift generation. The information obtained by the mean contour plots is critical for the robust aerodynamic design and the optimization of the airfoil's performance.

Furthermore, the uncertainty quantification analysis gives a clear image of how the variations in flow characteristics, as well as the shape of the airfoil, impact its overall performance. It is evident by the contour plots that there are certain high-risk areas of the airfoil that are susceptible to introducing uncertainty and therefore should be taken into consideration during the design of the airfoil. These regions include the leading and trailing edges of the airfoil, and the wake region. Additionally, as the flow regimes and the geometry of the airfoil become more complex, the uncertainties present become even more significant, making UQ analysis an indispensable part of aerodynamics study, and further reinforcing the objective of the present research.

Chapter 6

Conclusions

The study presented in this thesis focused on the development and evaluation of a new algorithm to quantify uncertainty in simpler geometries, such as the lid-driven cavity, or, more importantly, in more sophisticated shapes like the NACA airfoils. This novel approach attempts to solve the Navier-Stokes equations, by uncoupling them and solving them separately and iteratively. For the completion of this task, the iterative Newton method is employed. The main objective of this method is to achieve faster and less computationally expensive simulations, than the traditional methods solving the coupled form of the simulations. Finally, UQ was conducted for various NACA airfoil types and flow conditions, for which the Monte Carlo and Polynomial Chaos methods were employed.

Through comprehensive analysis, the study reveals how the Reynolds number and the airfoil design impact the behavior of the flow around it. Higher Reynolds numbers lead to thinner boundary layers and narrower wake regions, which proves to be beneficial for lift generation. Conversely, flows with low Reynolds numbers are characterized by increased drag and diminished aerodynamic efficiency. However, an important observation was made about the significance of the camber on an airfoil, which itself produces lift, a property that may be useful for applications where maximum lift generation is required for low angles of attack.

However, the substance of this thesis is the UQ analysis. The UQ results underscore the critical impact of the varying Reynolds numbers and airfoil camber on flow characteristics. It was found that when introducing complexity into the flow or the geometry itself, uncertainty is more pronounced, especially in high-risk parts of the airfoil which were easier to identify through the simulations. Recognizing these regions is critical for the improvement of aerodynamic design and the performance of airfoils.

While the present research has aimed to enhance our understanding of UQ in aerodynamic simulations, it comes with its own limitations. The current algorithm faces challenges when applied to unsteady flows and complex geometries, especially at higher angles of attack. However, after taking appropriate measures like applying stabilization techniques, the method could be applied to even turbulent flows and cambered airfoils.

Considering those limitations, future research should focus on addressing these limitations, so that the algorithm can give us more comprehensive results, including data from tests conducted for different angles of attack, drag and lift coefficient plots, and, overall more stable and even more reliable results. Later on, a proposed use for this algorithm could be its inclusion in machine learning models constructed for optimization, to facilitate robust design and produce more efficient airfoils.

In summary, this thesis highlights the role of uncertainty quantification in aerodynamic modeling and airfoil design. By recognizing and quantifying uncertainties, the proposed algorithm can serve as a valuable tool for enhancing aerodynamic design and enabling faster, more reliable simulations in the future.

Bibliography

[1] Ansys | Engineering Simulation Software.

[2] ANSYS FLUENT 12.0 User's Guide - 6.1 Mesh Topologies.

[3] Chaospy — chaospy 4.3.13 documentation.

[4] DOLFIN documentation — DOLFIN documentation.

[5] FEniCS.

[6] Finite Element Method Basics - MATLAB & Simulink.

[7] mshr documentation — mshr 2018.2.0.dev0 documentation.

[8] NumPy -.

[9] ParaView - Open-Source, Multi-Platform Data Analysis and Visualization Application.

[10] Airfoil | Aerodynamics, Wing Design, Flight Dynamics | Britannica, March 2024.

[11] Mach number | Description & Facts | Britannica, May 2024.

[12] Ira H. Abbott, Albert E. Von Doenhoff, and Louis Stivers. Summary of Airfoil Data. Technical report, National Advisory Committee for Aeronautics, January 1945. NTRS Author Affiliations: NTRS Report/Patent Number: NACA-TR-824 NTRS Document ID: 19930090976 NTRS Research Center: Legacy CDMS (CDMS).

[13] Ali Akbar. Effect of Angle of Attack on Airfoil NACA 0012 Performance. *R.E.M. (Rekayasa Energi Manufaktur) Jurnal*, 5(1):35–40, June 2020. Number: 1.

[14] Ahmad A. Alsahlani. A Study of Impacts of Airfoil Geometry on the Aerodynamic Performance at Low Reynolds Number. *International Journal of Mechanical Engineering and Robotics Research*, pages 99–106, 2023.

[15] Vish Subramaniam Amos Gilat. *Numerical Methods For Engineers And Scientists.*

[16] J. D. Anderson. *Governing Equations of Fluid Dynamics*, pages 15–51. Springer Berlin Heidelberg, Berlin, Heidelberg, 1992.

[17] J.D. Anderson. *Fundamentals of Aerodynamics.* McGraw-Hill Education, 2010.

[18] Anthony J. Martyr and David R. Rogers. *Measurement of liquid fuel, oil, and combustion air consumption.* Butterworth-Heinemann, January 2021. Pages: 511-535.

[19] Asproulias Ioannis. Experimental study of the effect of wing arrangement on the aerodynamic loads of a model aircraft wing, 2008.

[20] Australian Mathematical Sciences Institute. Newton-raphson method. https://amsi.org.au/ESA_Senior_Years/SeniorTopic3/3j/3j_2content_2.html, 2024. Accessed: 2024-08-24.

[21] J. Banaszek, Y. Ria, Tomasz Kowalewski, and Marek Rebow. Semi-implicit fem analysis of natural convection in freezing water. *Numerical Heat Transfer Applications*, 36, 03 2000.

[22] Chakshu Baweja, Ishaan Prakash, Dhannarapu Rakesh, and Utsav Niroula. *Analysis and Optimization of Dimpled Surface Modified for Wing Planforms.* July 2016.

[23] Robert S. Brodkey and Harry C. Hershey. *Transport Phenomena: A Unified Approach*. Brodkey Publishing, February 2003. Google-Books-ID: CjBTMYXM7ccC.

[24] Alexander N. Brooks and Thomas J.R. Hughes. Streamline upwind/petrov-galerkin formulations for convection dominated flows with particular emphasis on the incompressible navier-stokes equations. *Computer Methods in Applied Mechanics and Engineering*, 32(1):199–259, 1982.

[25] Claudia E. Brunner, Janik Kiefer, Martin O. L. Hansen, and Marcus Hultmark. Study of Reynolds number effects on the aerodynamics of a moderately thick airfoil using a high-pressure wind tunnel. *Experiments in Fluids*, 62(8):178, August 2021.

[26] Cadence CFD. CFD Meshing Methods.

[27] Ramon Codina. Comparison of some finite element methods for solving the diffusion-convection-reaction equation. *Computer Methods in Applied Mechanics and Engineering*, 156:185–210, 04 1998.

[28] COMSOL AB. *COMSOL Multiphysics® Reference Manual*. COMSOL AB, 2017. https://doc.comsol.com/5.3/doc/com.comsol.help.comsol/comsol_api_xmesh.40.4.html.

[29] R. Courant. Variational methods for the solution of problems of equilibrium and vibrations. *Bulletin of the American Mathematical Society*, 49(1):1–23, January 1943. Publisher: American Mathematical Society.

[30] F. E. C. Culick. The Wright Brothers: First Aeronautical Engineers and Test Pilots. *AIAA Journal*, 41(6):985–1006, 2003. Publisher: American Institute of Aeronautics and Astronautics _eprint: https://doi.org/10.2514/2.2046.

[31] E. Dick. Introduction to Finite Element Methods in Computational Fluid Dynamics. In John F. Wendt, editor, *Computational Fluid Dynamics*, pages 235–274. Springer, Berlin, Heidelberg, 2009.

[32] Karthik Duraisamy, Gianluca Iaccarino, and Heng Xiao. Turbulence Modeling in the Age of Data. *Annual Review of Fluid Mechanics*, 51(Volume 51, 2019):357–377, January 2019. Publisher: Annual Reviews.

[33] Manely Eslahpazir, Rainer Krull, and Ulrich Krühne. 2.09 - computational fluid dynamics. In Murray Moo-Young, editor, *Comprehensive Biotechnology (Third Edition)*, pages 95–107. Pergamon, Oxford, third edition edition, 2019.

[34] A. Galántai. The theory of Newton's method. *Journal of Computational and Applied Mathematics*, 124(1):25–44, December 2000.

[35] Herman F. George and Farrukh Qureshi. *Newton's Law of Viscosity, Newtonian and Non-Newtonian Fluids*, pages 2416–2420. Springer US, Boston, MA, 2013.

[36] Roger Ghanem, David Higdon, and Houman Owhadi. Introduction to Uncertainty Quantification. In Roger Ghanem, David Higdon, and Houman Owhadi, editors, *Handbook of Uncertainty Quantification*, pages 3–6. Springer International Publishing, Cham, 2017.

[37] Roger Ghanem and John Red-Horse. Polynomial Chaos: Modeling, Estimation, and Approximation. In Roger Ghanem, David Higdon, and Houman Owhadi, editors, *Handbook of Uncertainty Quantification*, pages 521–551. Springer International Publishing, Cham, 2017.

[38] U Ghia, K.N Ghia, and C.T Shin. High-re solutions for incompressible flow using the navier-stokes equations and a multigrid method. *Journal of Computational Physics*, 48(3):387–411, 1982.

[39] Charles Harvard Gibbs-Smith and Science Museum (Great Britain). *Sir George Cayley's Aeronautics, 1796-1855*. H.M. Stationery Office, 1962. Google-Books-ID: dAtFAAAAIAAJ.

[40] G.R. Liu and S. S. Quek. *The Finite Element Method : A Practical Course*, volume Second edition. Butterworth-Heinemann, Oxford, UK, 2013.

[41] David Greenblatt and Israel J. Wygnanski. The control of flow separation by periodic excitation. *Progress in Aerospace Sciences*, 36(7):487–545, October 2000.

[42] Murli M. Gupta and Jiten C. Kalita. A new paradigm for solving navier–stokes equations: stream-function–velocity formulation. *Journal of Computational Physics*, 207(1):52–68, 2005.

[43] Ajay Harish. What Is FEM & FEA Explained | Finite Element Method, October 2016.

[44] Tahj Hill. Numerical Analysis and Fluid Flow Modeling of Incompressible Navier-Stokes Equations. *UNLV Theses, Dissertations, Professional Papers, and Capstones*, May 2019.

[45] Joe D. Hoffman and Steven Frankel. *Numerical Methods for Engineers and Scientists*. CRC Press, October 2018. Google-Books-ID: F5K3DwAAQBAJ.

[46] Shuling Hou, Qisu Zou, Shiyi Chen, Gary Doolen, and Allen C. Cogley. Simulation of cavity flow by the lattice boltzmann method. *Journal of Computational Physics*, 118(2):329–347, 1995.

[47] Thomas J.R. Hughes. Multiscale phenomena: Green's functions, the dirichlet-to-neumann formulation, subgrid scale models, bubbles and the origins of stabilized methods. *Computer Methods in Applied Mechanics and Engineering*, 127(1):387–401, 1995.

[48] W.F. Hughes and J.A. Brighton. *Schaum's Outline of Theory and Problems of Fluid Dynamics: By William F. Hughes and John A. Brighton*. Schaum's outline series. McGraw-Hill, 1967.

[49] David G. Hull. *Fundamentals of Airplane Flight Mechanics*. Springer Science & Business Media, January 2007. Google-Books-ID: QUZgTj7iejwC.

[50] J. Gordon Leishman. *Introduction to Aerospace Flight Vehicles*. January 2023.

[51] Jacobs, Eastman N Ward, Kenneth E and Pinkerton, Robert M. The characteristics of 78 related airfoil sections from tests in the variable-density wind tunnel. NACA Technical Report 19930091108, January 1933.

[52] A. Jameson. The Evolution of Computational Methods in Aerodynamics. *Journal of Applied Mechanics*, 50(4b):1052–1070, December 1983.

[53] Volker John. The Stokes Equations. In Volker John, editor, *Finite Element Methods for Incompressible Flow Problems*, pages 137–242. Springer International Publishing, Cham, 2016.

[54] Mrinal Kaushik. Thin Airfoil Theory. In Mrinal Kaushik, editor, *Theoretical and Experimental Aerodynamics*, pages 127–144. Springer, Singapore, 2019.

[55] Kwangki Kim, Dongying Shen, Zoltan Nagy, and Richard Braatz. Wiener's polynomial chaos for the analysis and control of nonlinear dynamical systems with probabilistic uncertainties. *Control Systems, IEEE*, 33:58–67, 10 2013.

[56] George Klir and Bo Yuan. *Fuzzy sets and fuzzy logic*, volume 4. Prentice hall New Jersey, 1995.

[57] Kozo Fujii. Progress and future prospects of CFD in aerospace—Wind tunnel and beyond. *Progress in Aerospace Sciences*, 41(6):455–470, August 2005. Publisher: Pergamon.

[58] K. S. G. Krishnan, O. Bertram, and O. Seibel. Review of hybrid laminar flow control systems. *Progress in Aerospace Sciences*, 93:24–52, August 2017.

[59] Aymen Labidi. What Is the Mach number? November 2019.

[60] Ulrich Langer and Martin Neumüller. *Direct and Iterative Solvers*, pages 205–251. Springer International Publishing, Cham, 2018.

[61] Maurice Lemaire. *Mechanics and Uncertainty*. John Wiley & Sons, April 2014. Google-Books-ID: cj1jAwAAQBAJ.

[62] Xingrui Li, Chengxi Liu, Chenxu Wang, and Federico Milano. Arbitrary polynomial chaos-based power system dynamic analysis with correlated uncertainties. *International Journal of Electrical Power & Energy Systems*, 157:109806, 2024.

[63] Wing Kam Liu, Shaofan Li, and Harold S. Park. Eighty Years of the Finite Element Method: Birth, Evolution, and Future. *Archives of Computational Methods in Engineering*, 29(6):4431–4453, October 2022.

[64] Alex Loeven and Hester Bijl. Airfoil Analysis with Uncertain Geometry Using the Probabilistic Collocation Method. In *49th AIAA/ASME/ASCE/AHS/ASC Structures, Structural Dynamics, and Materials Conference, 16th AIAA/ASME/AHS Adaptive Structures Conference,10th AIAA Non-Deterministic Approaches Conference, 9th AIAA Gossamer Spacecraft Forum, 4th AIAA Multidisciplinary Design Optimization Specialists Conference*, Structures, Structural Dynamics, and Materials and Co-located Conferences. American Institute of Aeronautics and Astronautics, April 2008.

[65] Daryl L. Logan. *A First Course in the Finite Element Method*. THOMSON, 2011. Google-Books-ID: Dwk3EAAAQBAJ.

[66] Fei Lu, Matthias Morzfeld, Xuemin Tu, and Alexandre J. Chorin. Limitations of polynomial chaos expansions in the bayesian solution of inverse problems. *Journal of Computational Physics*, 282:138–147, 2015.

[67] Maeda and Schepers. Wind turbine performance assessment and knowledge management for aerodynamic behaviour modelling and design: IEA experience. In *Wind Energy Systems*, pages 350–365. Woodhead Publishing, January 2011.

[68] Marcelo Dasilva and Nancy Hall. What Is Drag?, July 2022.

[69] Koushik Marepally, Yong Su Jung, James Baeder, and Ganesh Vijayakumar. Uncertainty quantification of wind turbine airfoil aerodynamics with geometric uncertainty. *Journal of Physics: Conference Series*, 2265(4):042041, May 2022.

[70] Michael J. Martin and Iain D. Boyd. Blasius boundary layer solution with slip flow conditions. *AIP Conference Proceedings*, 585(1):518–523, August 2001.

[71] David Miller, Brenda Ng, John Eslick, Charles Tong, and Yang Chen. Advanced computational tools for optimization and uncertainty quantification of carbon capture processes. *Computer Aided Chemical Engineering*, 34:202–211, 12 2014.

[72] A. Monti, Ferdinanda Ponci, and Teems Lovett. A polynomial chaos theory approach to uncertainty in electrical engineering. volume 2005, page 6 pp., 12 2005.

[73] Yasuki Nakayama. Chapter 9 - Drag and Lift. In Yasuki Nakayama, editor, *Introduction to Fluid Mechanics (Second Edition)*, pages 177–201. Butterworth-Heinemann, January 2018.

[74] William L. Oberkampf and Timothy G. Trucano. Verification and Validation in Computational Fluid Dynamics. Technical Report SAND2002-0529, Sandia National Lab. (SNL-NM), Albuquerque, NM (United States); Sandia National Lab. (SNL-CA), Livermore, CA (United States), March 2002.

[75] Jigar Parekh. *Development of Methods for Uncertainty Quantification in CFD Applied to Wind Turbine Wake Prediction*. PhD thesis, University of Groningen, 2023.

[76] Peter F. Pelz, Marc E. Pfetsch, Sebastian Kersting, Michael Kohler, Alexander Matei, Tobias Melz, Roland Platz, Maximilian Schaeffner, and Stefan Ulbrich. Types of Uncertainty. In Peter F. Pelz, Peter Groche, Marc E. Pfetsch, and Maximilian Schaeffner, editors, *Mastering Uncertainty in Mechanical Engineering*, pages 25–42. Springer International Publishing, Cham, 2021.

[77] Kim-Hung Pho. Improvements of the newton–raphson method. *Journal of Computational and Applied Mathematics*, 408:114106, 2022.

[78] Raphaël Pile and Guillaume Parent. Comparison of Stabilization Methods for Finite Element Method in the Context of Space Charges. In *24th International Conference on the Computation of Electromagnetic Fields (COMPUMAG)*, Kyoto, Japan, May 2023.

[79] C. RADHAKRISHNA Rao. Some Combinatorial Problems of Arrays and Applications to Design of Experiments†. In JAGDISH N. Srivastava, editor, *A Survey of Combinatorial Theory*, pages 349–359. North-Holland, January 1973.

[80] S.S. Rao. *The Finite Element Method in Engineering*. Elsevier Science, 2017.

[81] D. A. Reay. 1 - Mythology or Fact: Flight in Early Civilisations. In D. A. Reay, editor, *The History of Man-Powered Flight*, pages 1–10. Pergamon, January 1977.

[82] D. A. Reay. 2 - Leonardo da Vinci: — a Scientist among Sceptical Philosophers. In D. A. Reay, editor, *The History of Man-Powered Flight*, pages 11–29. Pergamon, January 1977.

[83] Christopher J. Roy and William L. Oberkampf. A comprehensive framework for verification, validation, and uncertainty quantification in scientific computing. *Computer Methods in Applied Mechanics and Engineering*, 200(25):2131–2144, June 2011.

[84] Ideen Sadrehaghighi. *Aerodynamics of Airfoils and Wings (including Case Studies)*. June 2023.

[85] R Schreiber and H.B Keller. Driven cavity flows by efficient numerical techniques. *Journal of Computational Physics*, 49(2):310–333, 1983.

[86] Mehmet Zeki Sener and Erhan Aksu. The numerical investigation of the rotation speed and Reynolds number variations of a NACA 0012 airfoil. *Ocean Engineering*, 249:110899, April 2022.

[87] Snorri Gudmundsson. *General Aviation Aircraft Design : Applied Methods and Procedures*, volume First edition. Butterworth-Heinemann, Oxford, UK, 2014.

[88] Victor Lyle Streeter, E. Benjamin Wylie, and Keith W. Bedford. *Fluid Mechanics*. WCB/McGraw Hill, 1998. Google-Books-ID: oJ5RAAAAMAAJ.

[89] Bruno Sudret. Polynomial chaos expansions. Master class, 4th National Conference on Multidisciplinary Design, Analysis and Optimization, October 2021. Indian Institute of Technology Madras, India.

[90] Suprayitno, J. C. Yu, Aminnudin, and R. Wulandari. Airfoil aerodynamics optimization under uncertain operating conditions. *Journal of Physics: Conference Series*, 1446(1):012014, January 2020. Publisher: IOP Publishing.

[91] Spatial Team. Manual vs. Auto Meshing: What's the Difference?, April 2022.

[92] James L. Tocher. The Evolution of the Finite Element Method. *SAE Transactions*, 89:24–28, 1980. Publisher: SAE International.

[93] Tom Benson. Inclination Effects on Lift.

[94] Tom Benson. What is Lift?, May 2021.

[95] A. Torres-Hernandez and Fernando Brambila. *Fractional Newton-Raphson Method*. October 2017.

[96] C. Unal, B. Williams, F. Hemez, S. H. Atamturktur, and P. McClure. Improved best estimate plus uncertainty methodology, including advanced validation concepts, to license evolving nuclear reactors. *Nuclear Engineering and Design*, 241(5):1813–1833, May 2011.

[97] Elena Vagnoni. The Reaction Turbines Used in PHES Units and Related Problems. January 2022.

[98] Dirk Vandepitte and David Moens. Quantification of uncertain and variable model parameters in non-deterministic analysis. In Alexander K. Belyaev and Robin S. Langley, editors, *IUTAM Symposium on the Vibration Analysis of Structures with Uncertainties*, volume 27, pages 15–28. Springer Netherlands, Dordrecht, 2011. Series Title: IUTAM Bookseries.

[99] S.P Vanka. Block-implicit multigrid solution of navier-stokes equations in primitive variables. *Journal of Computational Physics*, 65(1):138–158, 1986.

[100] Henk Kaarle Versteeg and Weeratunge Malalasekera. *An Introduction to Computational Fluid Dynamics: The Finite Volume Method*. Pearson Education, 2007.

[101] Tongguang Wang, Wei Zhong, Yaoru Qian, and Chengyong Zhu. Fundamentals of Computational Fluid Dynamics. In Tongguang Wang, Wei Zhong, Yaoru Qian, and Chengyong Zhu, editors, *Wind Turbine Aerodynamic Performance Calculation*, pages 175–191. Springer Nature Singapore, Singapore, 2023.

[102] Norbert Wiener. The homogeneous chaos. *American Journal of Mathematics*, 60:897, 1938.

[103] Heng Xiao and Paola Cinnella. Quantification of model uncertainty in RANS simulations: A review. *Progress in Aerospace Sciences*, 108:1–31, July 2019.

[104] Dongbin Xiu and George Em Karniadakis. The wiener–askey polynomial chaos for stochastic differential equations. *SIAM Journal on Scientific Computing*, 24(2):619–644, 2002.

[105] Claire Yu Yan. *Introduction to Engineering Thermodynamics*. BCcampus, 2022. Google-Books-ID: FvNrzwEACAAJ.

[106] Y.D. Dwivedi, Abdul Wahab, Aditi Deekshita Pallay, and Akhil Shesham. Effect of surface roughness on aerodynamic performance of the wing with NACA 4412 airfoil at Reynolds number 1.7 × 105. *Materials Today: Proceedings*, 56:468–476, January 2022. Publisher: Elsevier.

[107] L. A. Zadeh. Fuzzy sets. *Information and Control*, 8(3):338–353, June 1965.

[108] Juan Zhang, Junping Yin, and Ruili Wang. Basic Framework and Main Methods of Uncertainty Quantification. *Mathematical Problems in Engineering*, 2020(1):6068203, 2020. _eprint: https://onlinelibrary.wiley.com/doi/pdf/10.1155/2020/6068203.

[109] Olek C. Zienkiewicz, Robert L. Taylor, and J. Z. Zhu. *The Finite Element Method: Its Basis and Fundamentals*. Elsevier, May 2005. Google-Books-ID: YocoaH8lnx8C.

[110] Florian Zwicke, Philipp Knechtges, Marek Behr, and Stefanie Elgeti. Automatic implementation of material laws: Jacobian calculation in a finite element code with tapenade. *Computers & Mathematics with Applications*, 72(11):2808–2822, 2016.

Appendix A

Additional Results

A.1 Mean Distributions

A.1.1 NACA 0012

See Figures A.2 and A.2.

A.1.2 NACA 2412

See Figures A.4 and A.4.

A.1.3 NACA 4412

See Figures A.6 and A.6.

A.2 Standard Deviation

A.2.1 NACA 0012

See Figures A.7 and A.8.

A.2.2 NACA 2412

See Figures A.9 and A.10.

A.2.3 NACA 4412

See Figures A.11 and A.12.

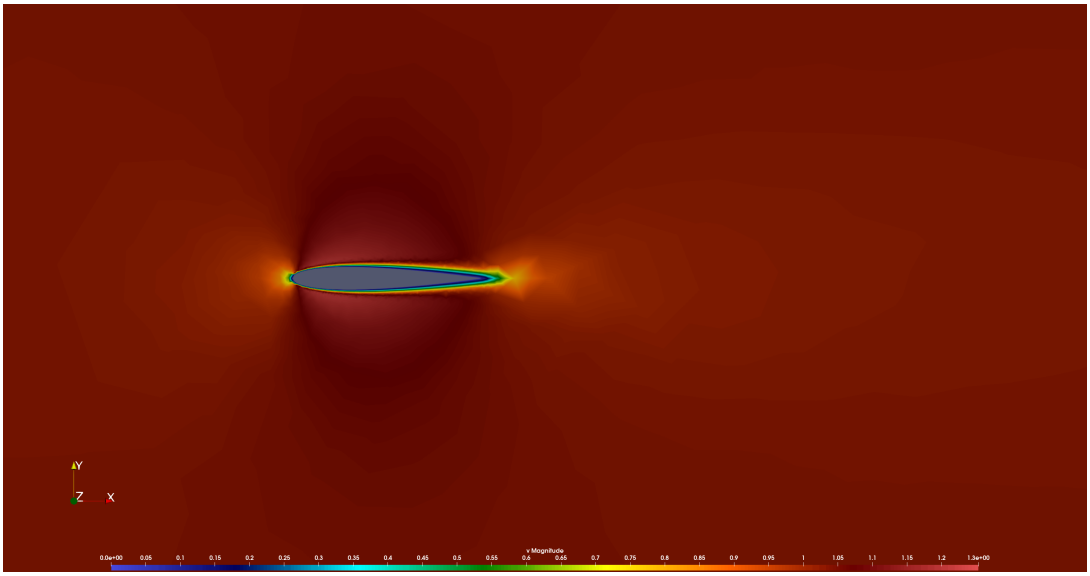

(a) $Re = 10^4$

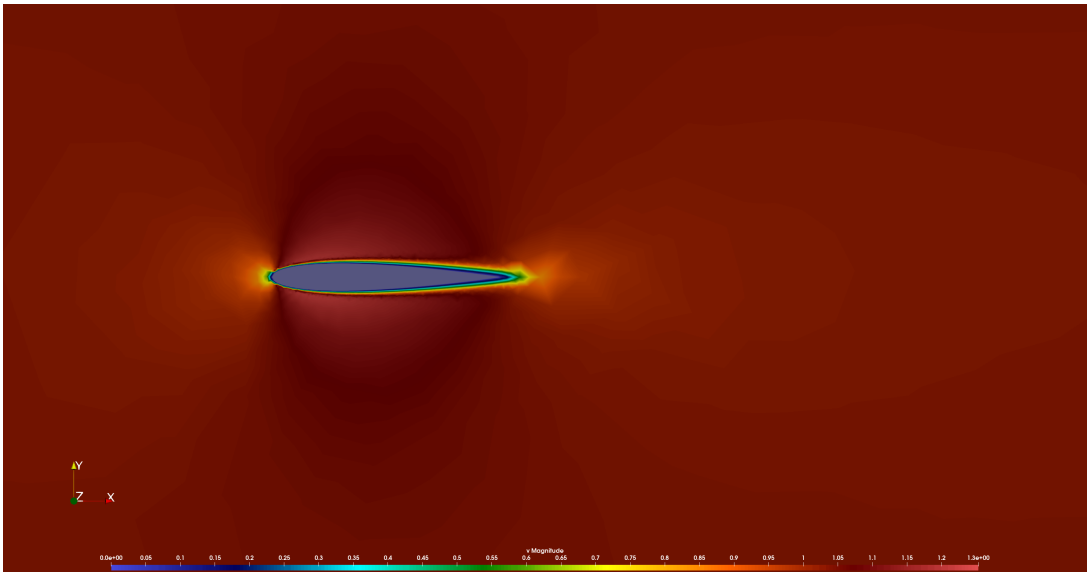

(b) $Re = 10^5$

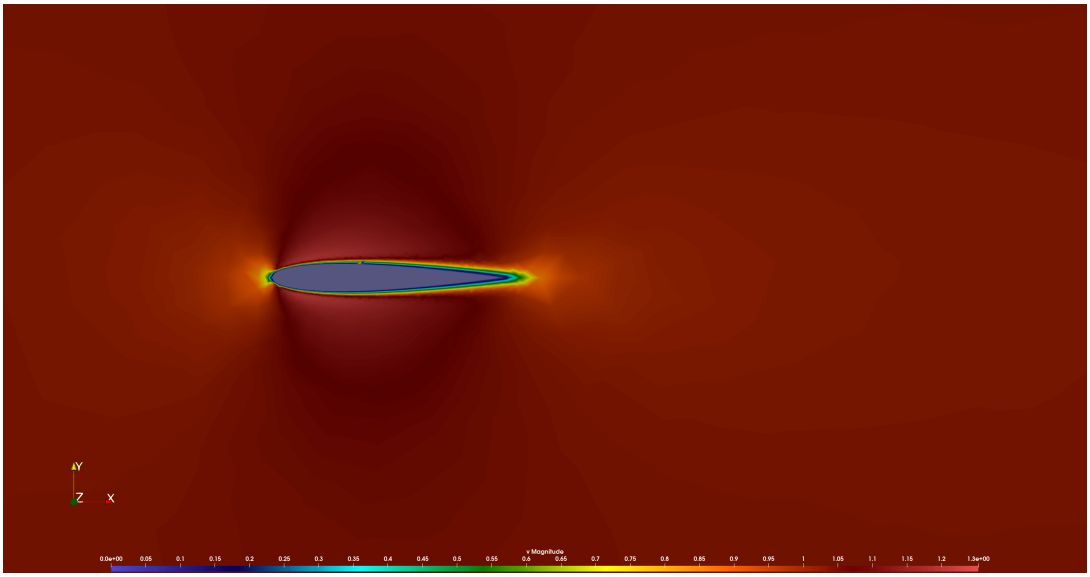

(c) $Re = 10^6$

Figure A.1: Velocity magnitude contour plot around a NACA 0012 airfoil

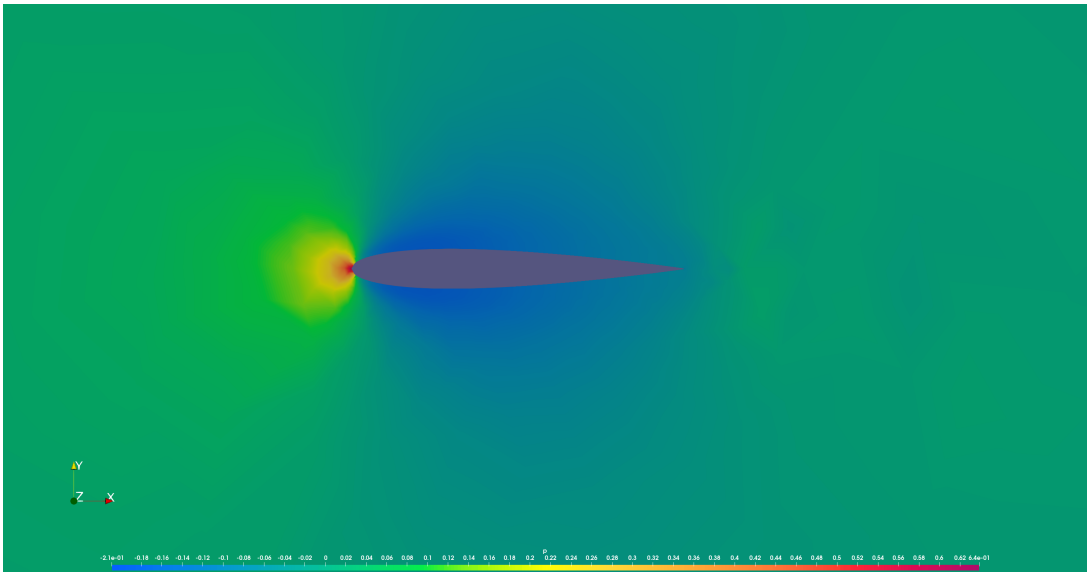

(a) $Re = 10^4$

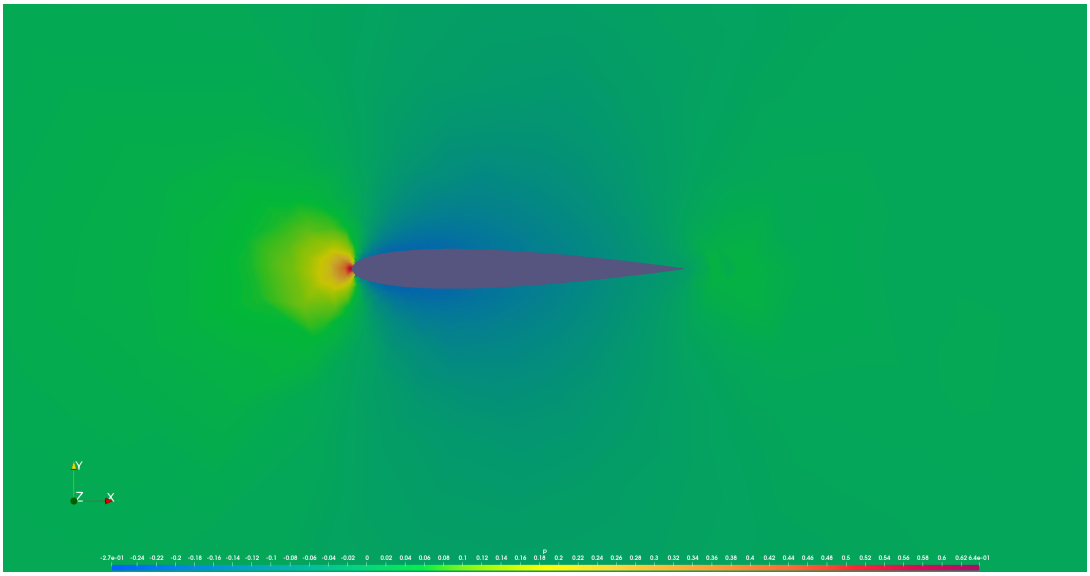

(b) $Re = 10^5$

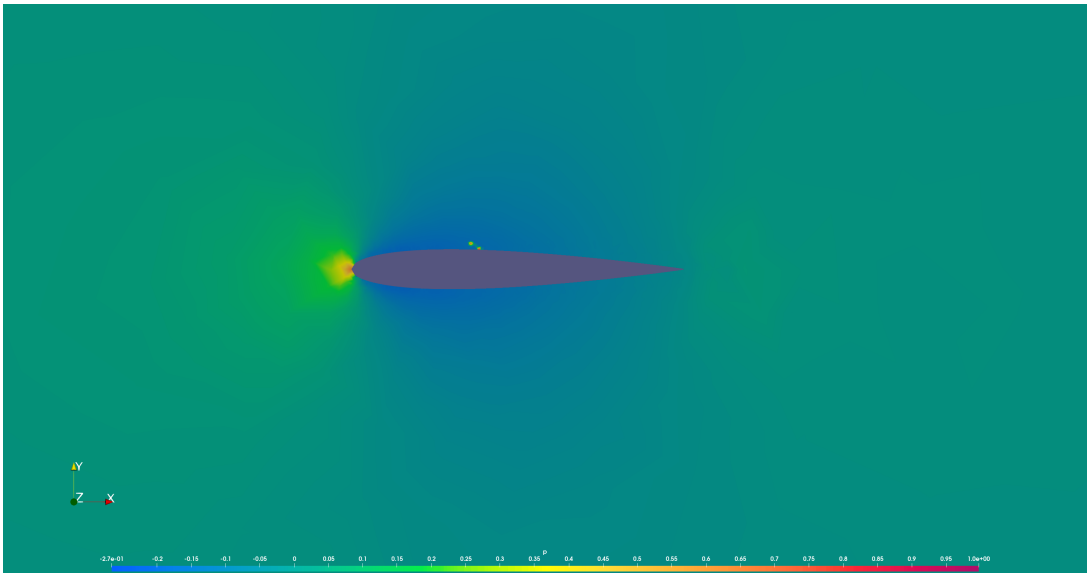

(c) $Re = 10^6$

Figure A.2: Pressure magnitude contour plot around a NACA 0012 airfoil

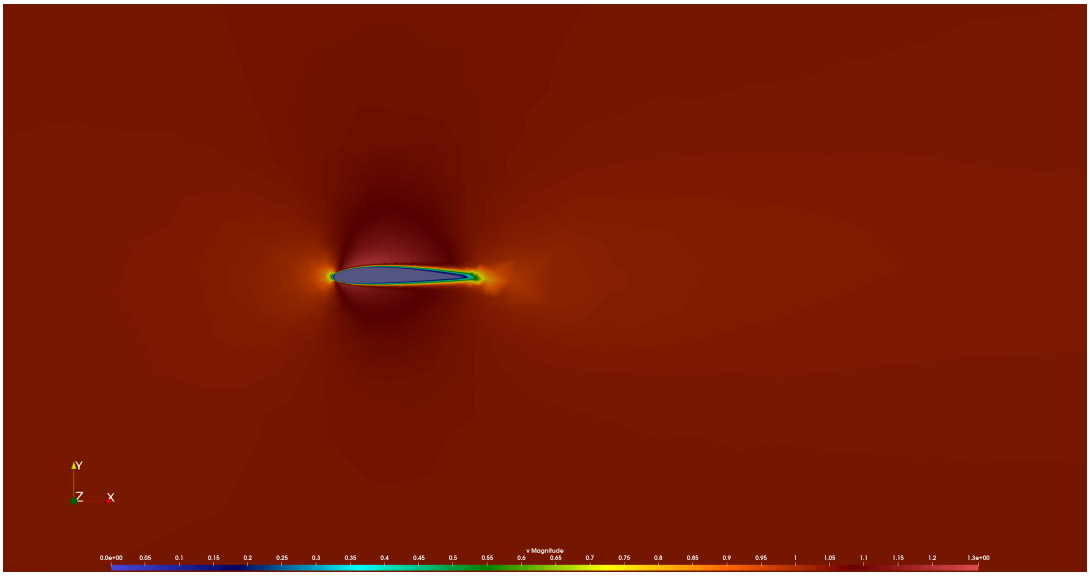

(a) $Re = 10^4$

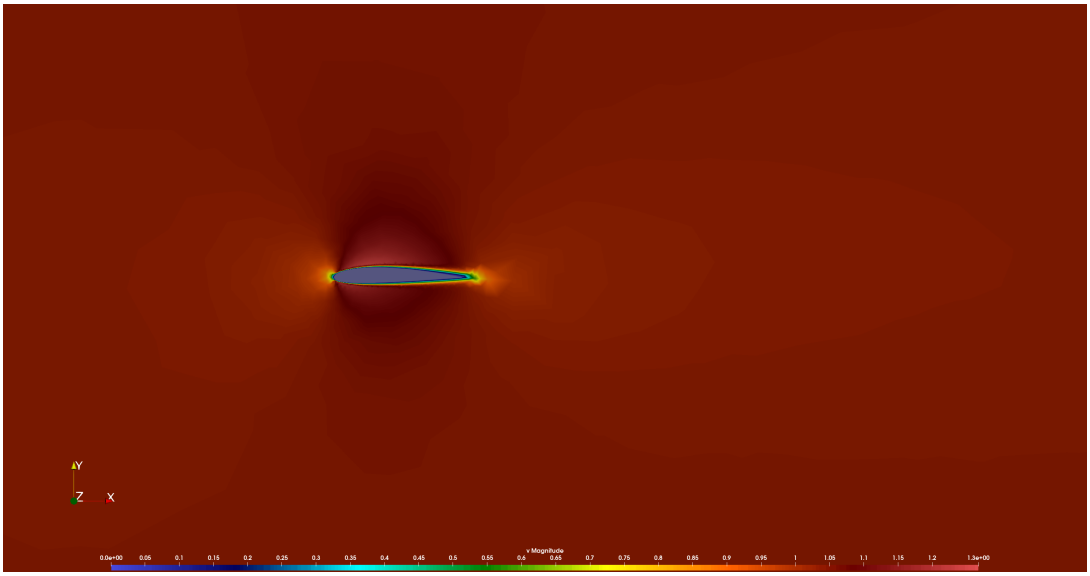

(b) $Re = 10^5$

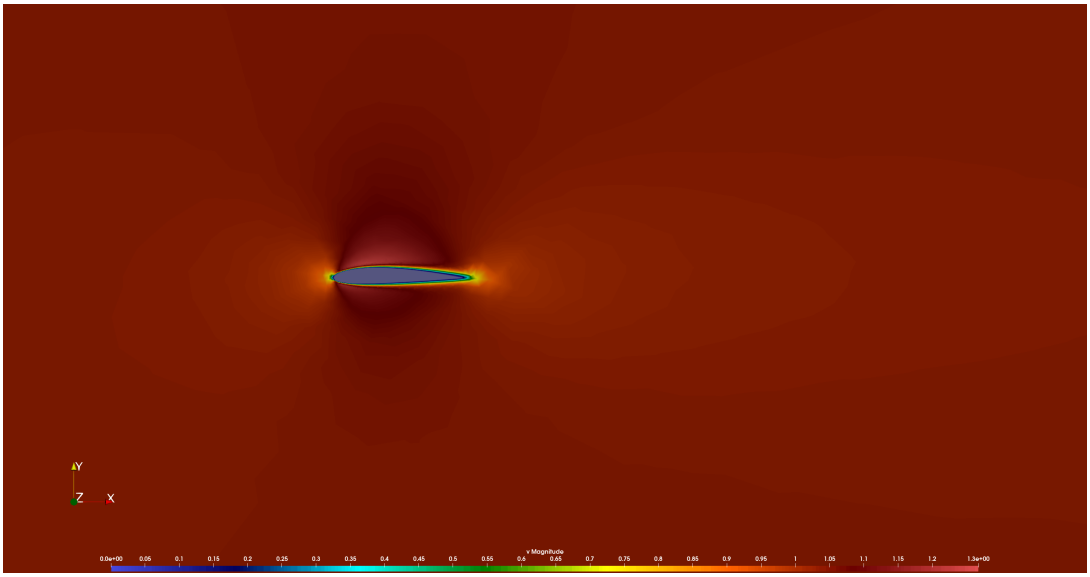

(c) $Re = 10^6$

Figure A.3: Velocity magnitude contour plot around a NACA 2412 airfoil

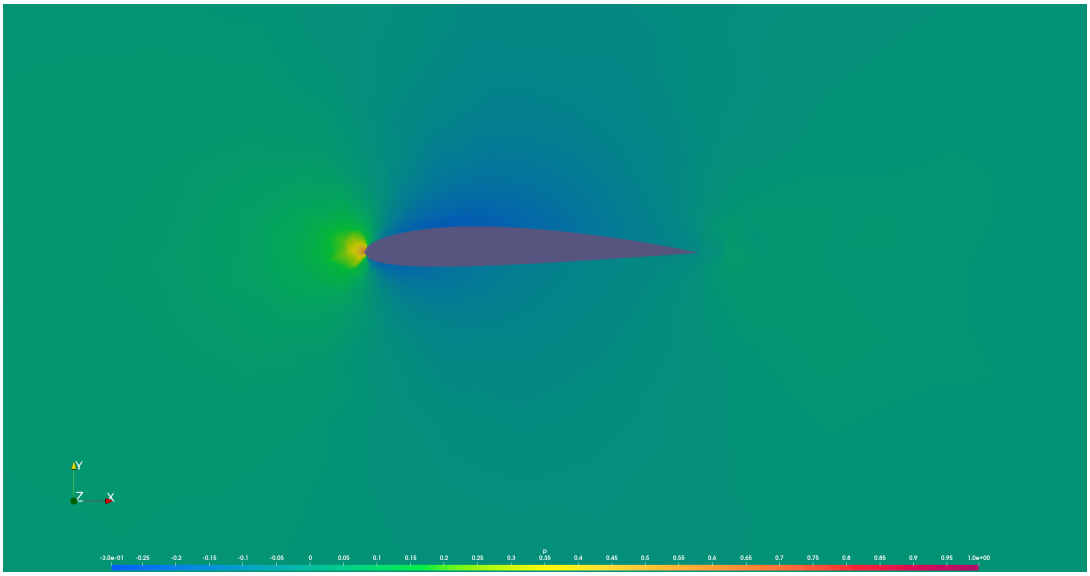

(a) $Re = 10^4$

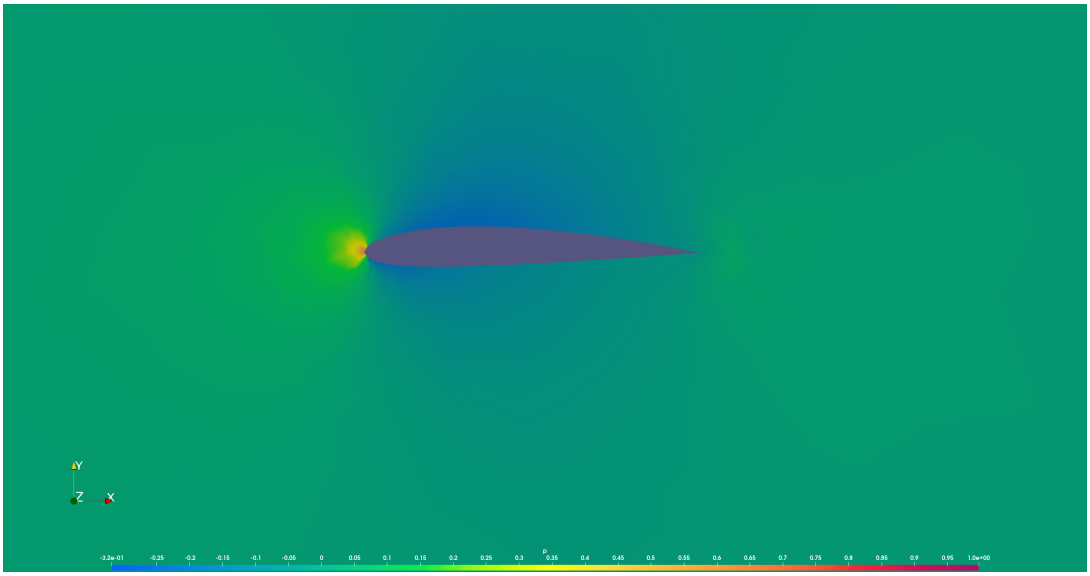

(b) $Re = 10^5$

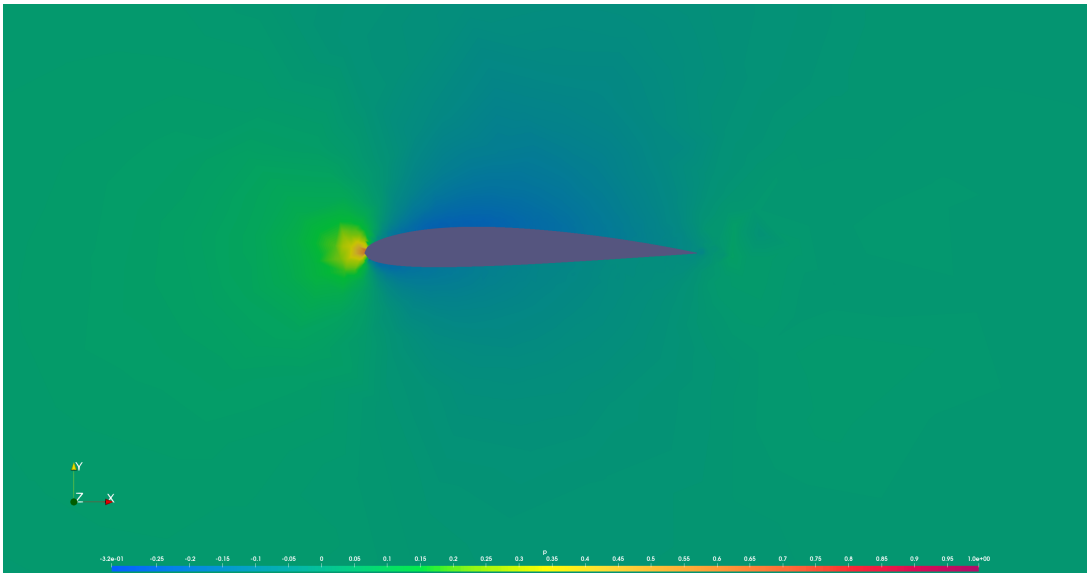

(c) $Re = 10^6$

Figure A.4: Pressure magnitude contour plot around a NACA 2412 airfoil

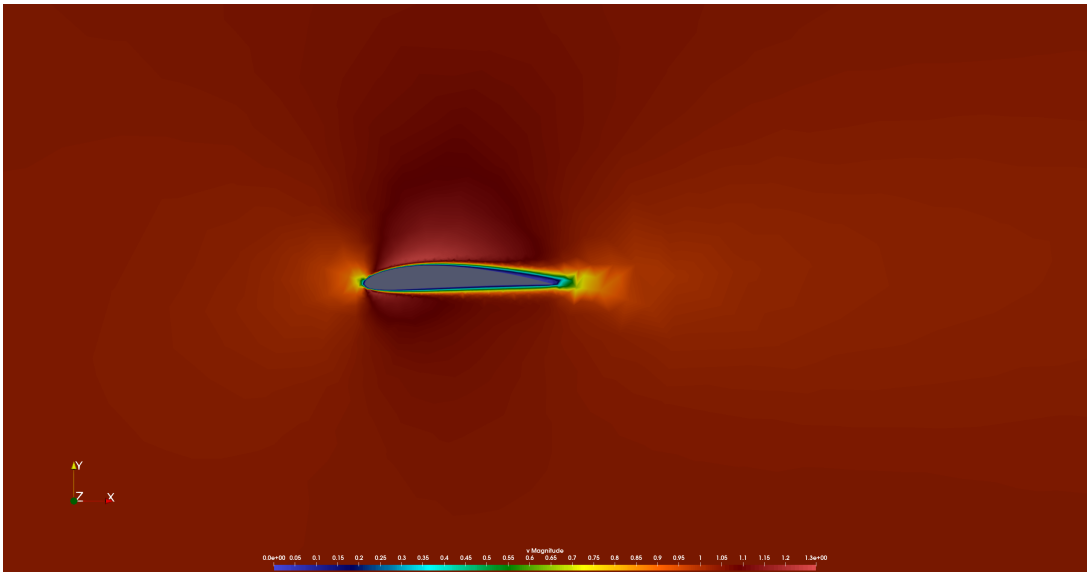

(a) $Re = 10^4$

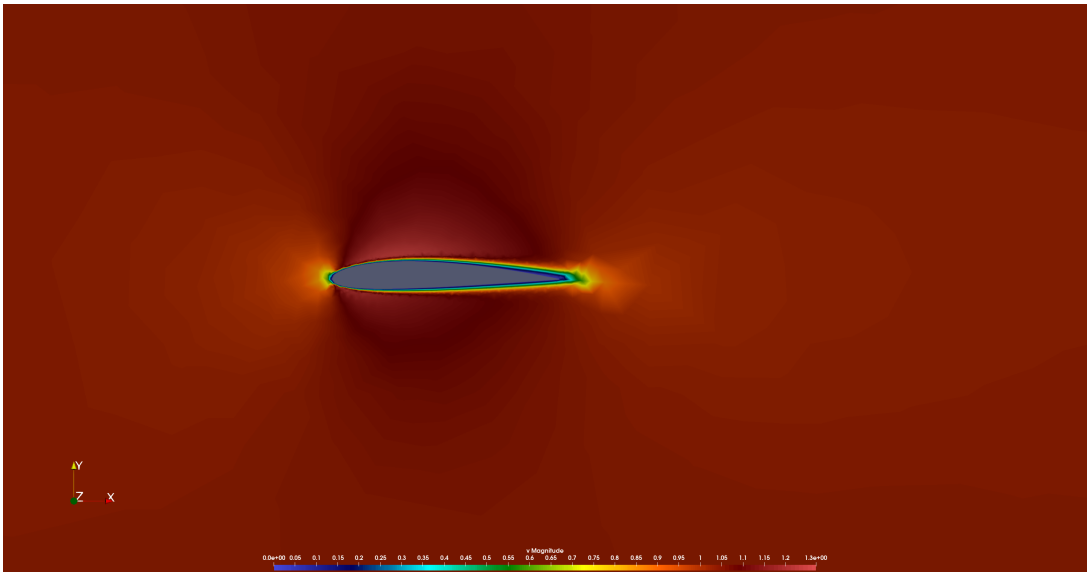

(b) $Re = 10^5$

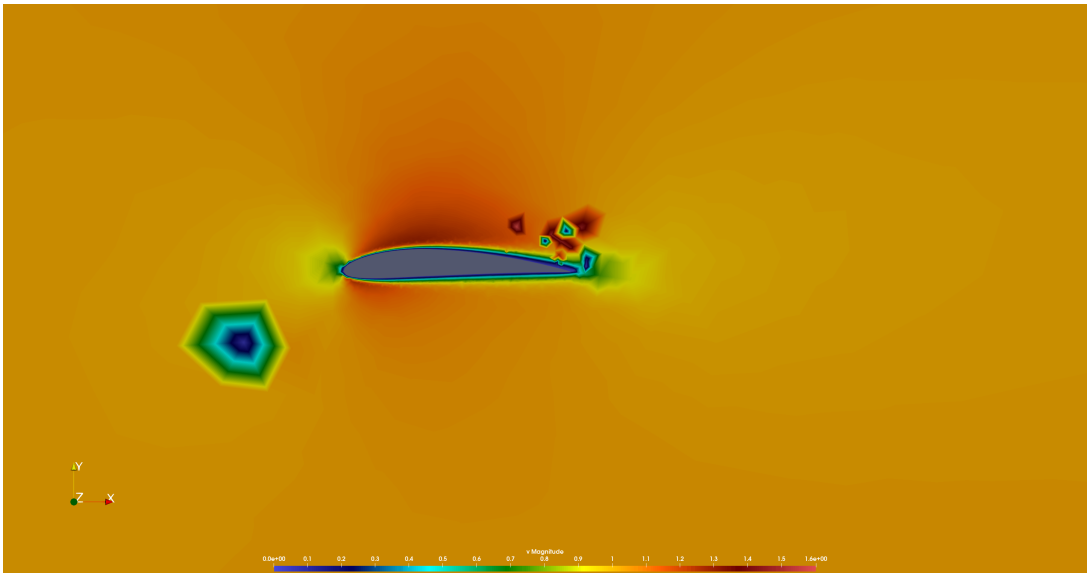

(c) $Re = 10^6$

Figure A.5: Velocity magnitude contour plot around a NACA 4412 airfoil

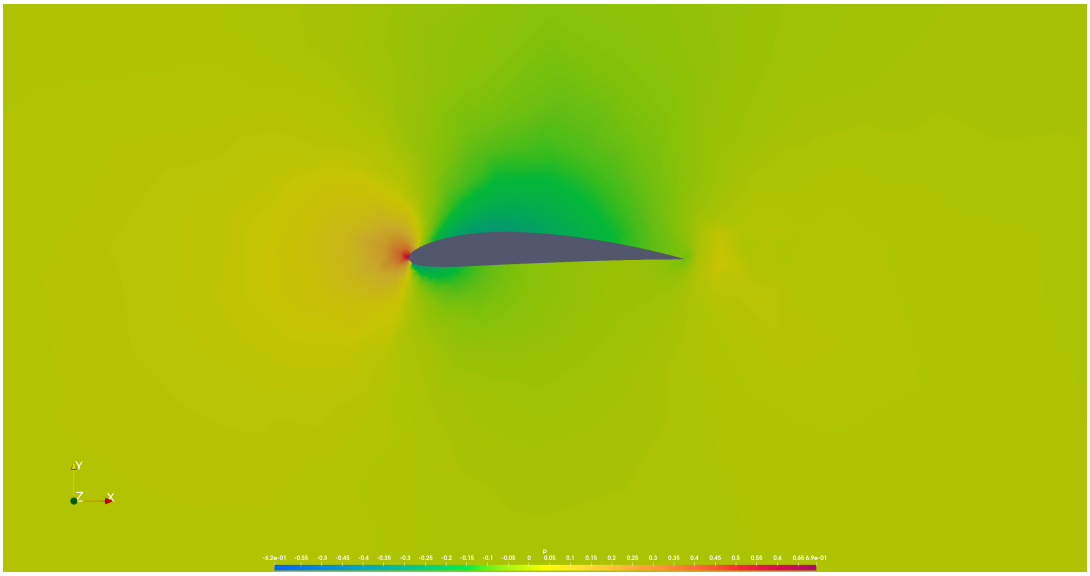

(a) $Re = 10^4$

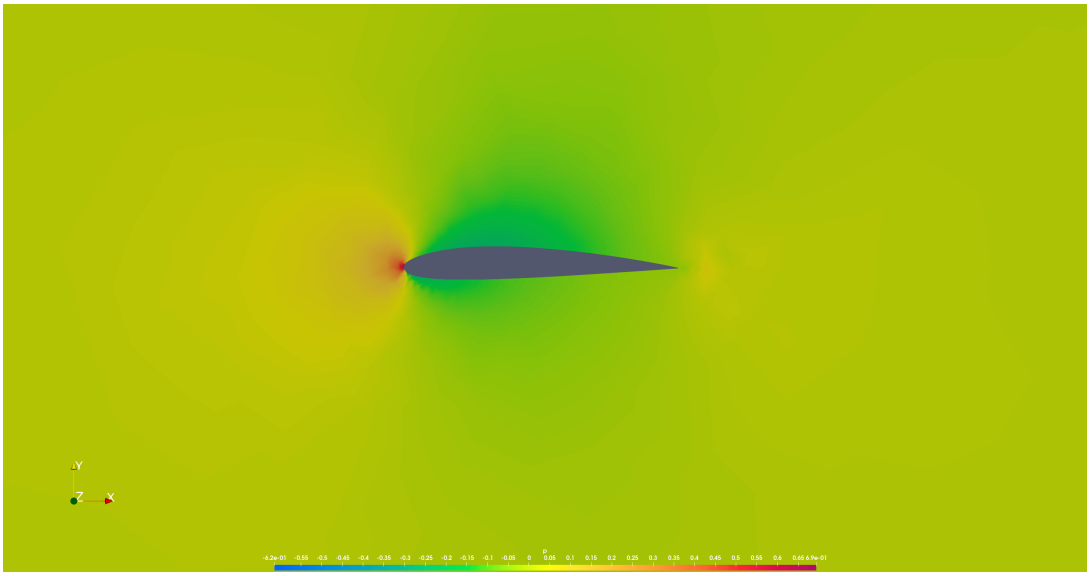

(b) $Re = 10^5$

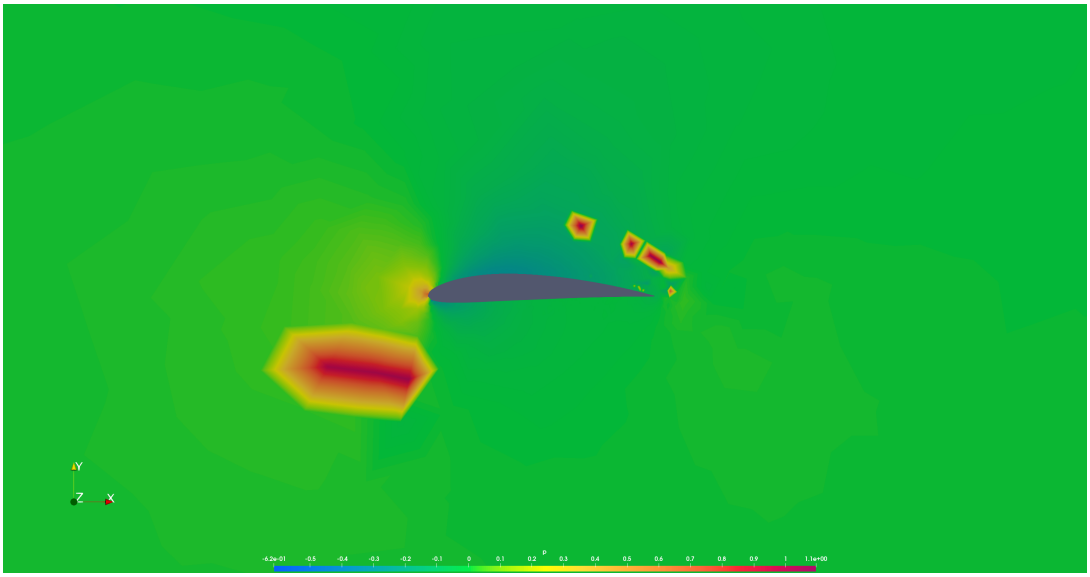

(c) $Re = 10^6$

Figure A.6: Pressure magnitude contour plot around a NACA 4412 airfoil

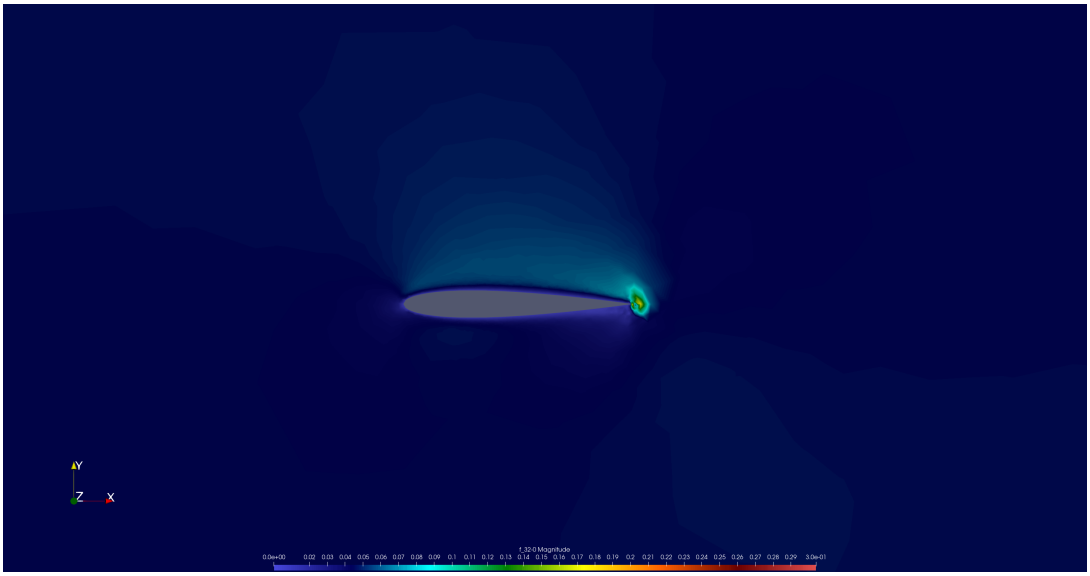

(a) $Re = 10^4$

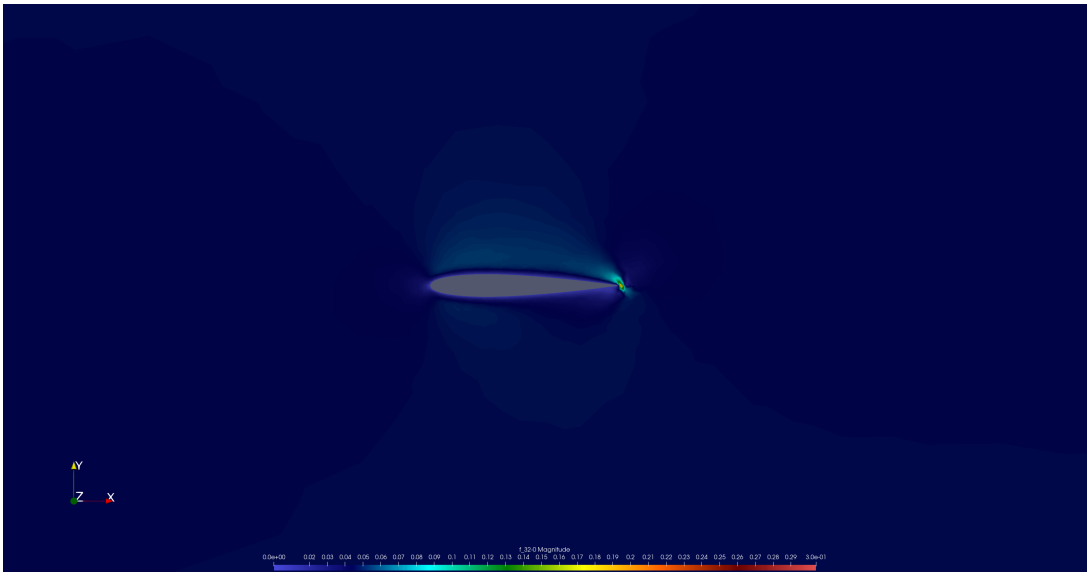

(b) $Re = 10^5$

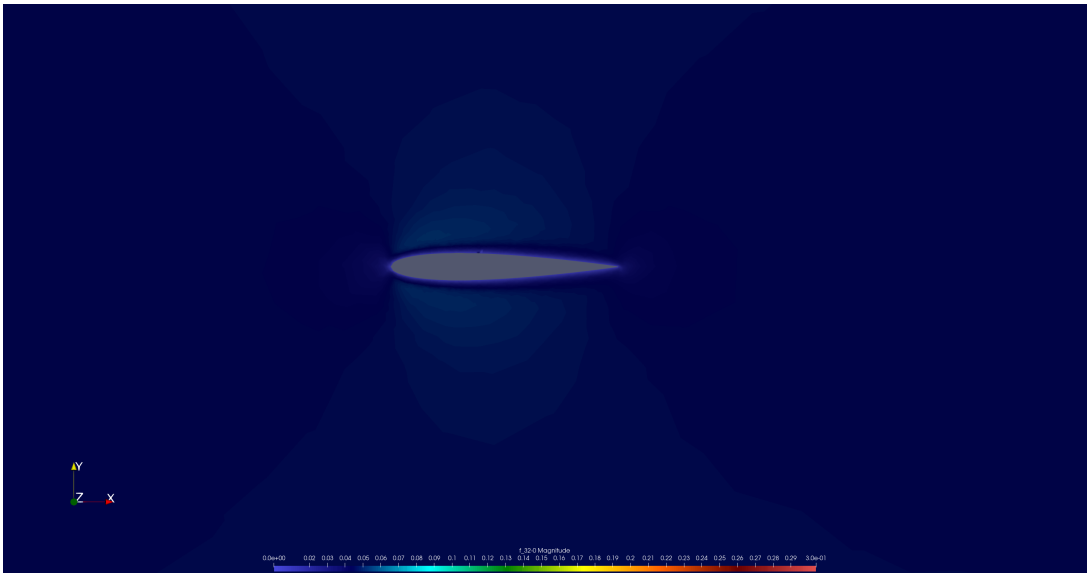

(c) $Re = 10^6$

Figure A.7: Standard deviation of velocity contour plot for a NACA 0012 airfoil

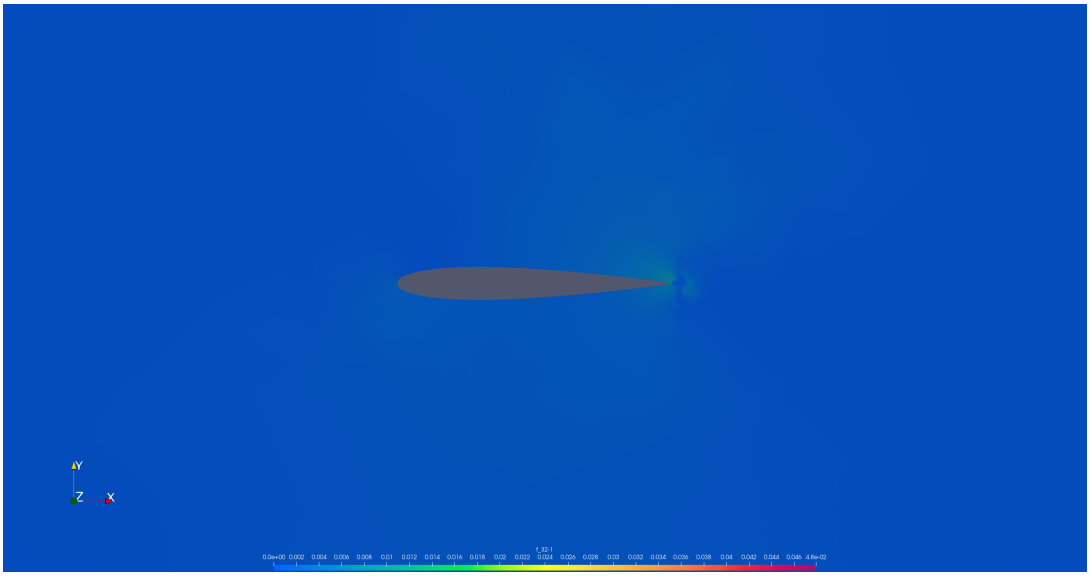

(a) $Re = 10^4$

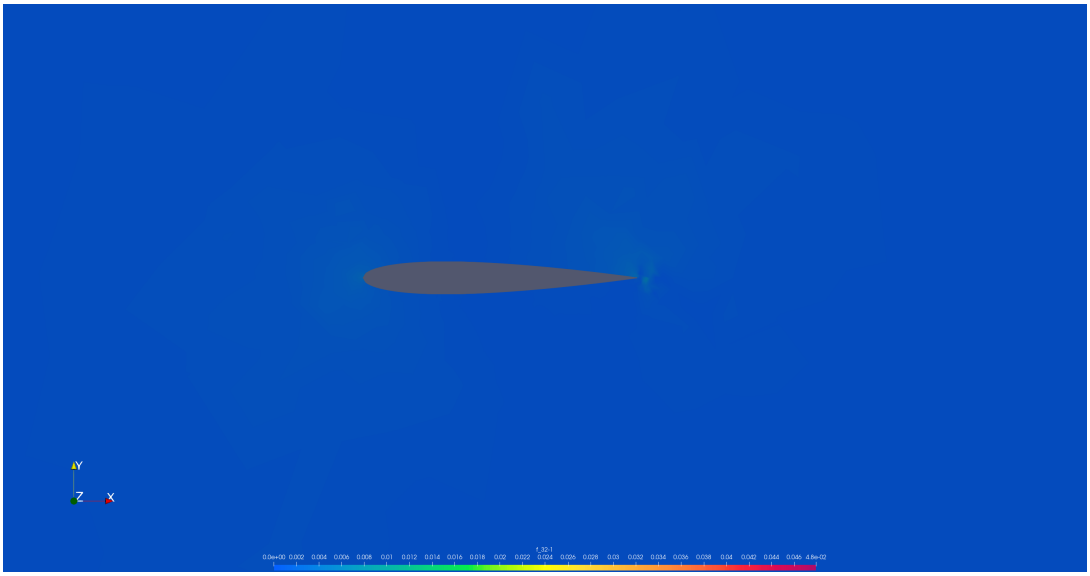

(b) $Re = 10^5$

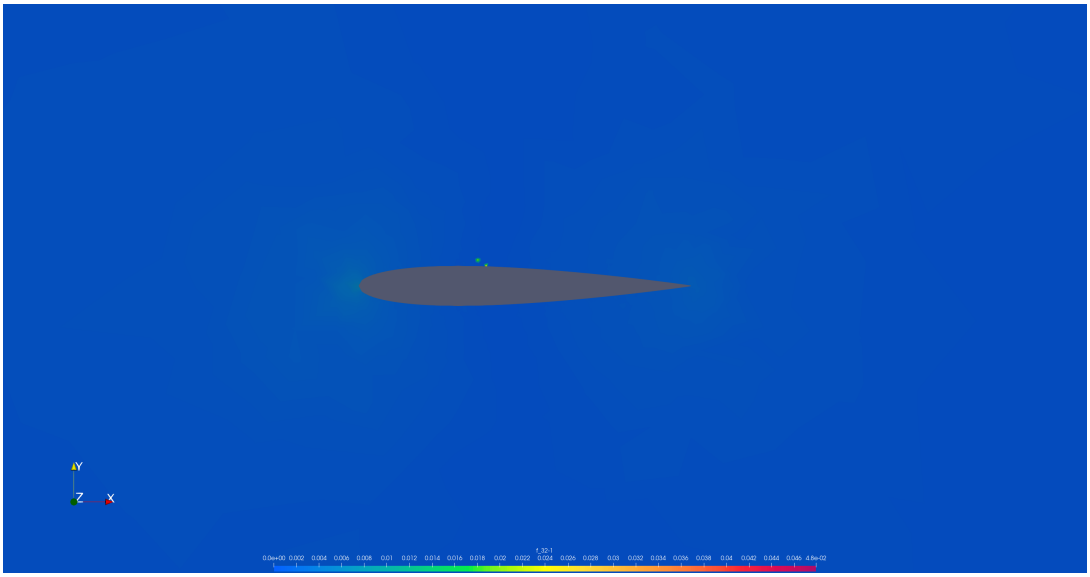

(c) $Re = 10^6$

Figure A.8: Standard deviation of pressure contour plot for a NACA 0012 airfoil

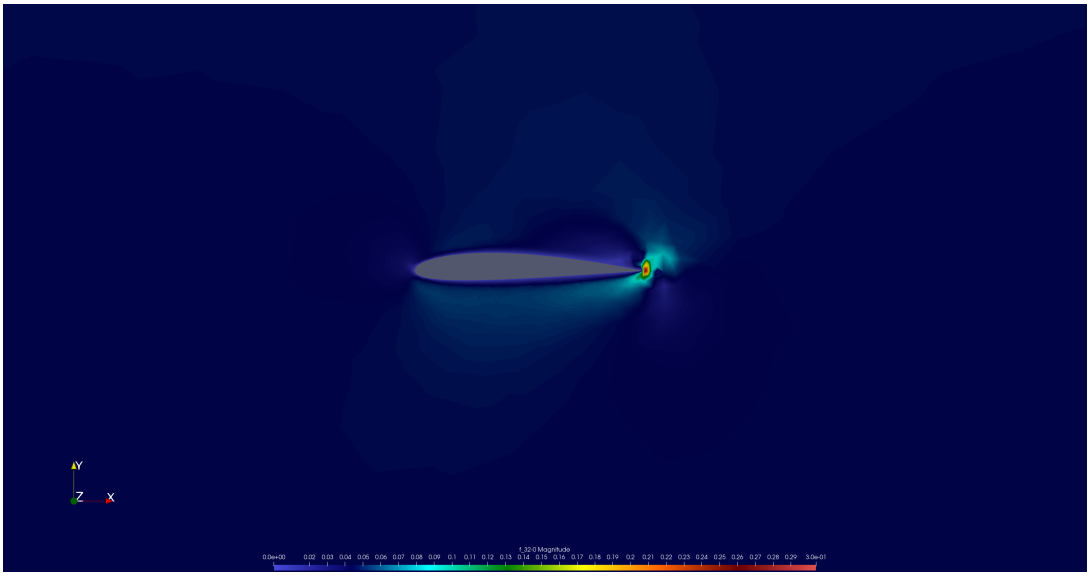

(a) $Re = 10^4$

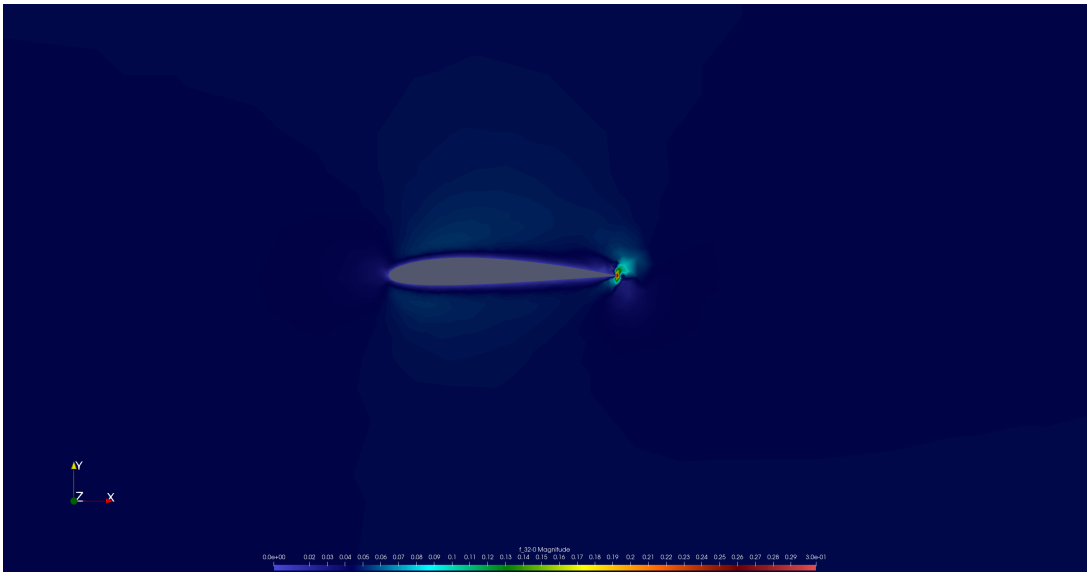

(b) $Re = 10^5$

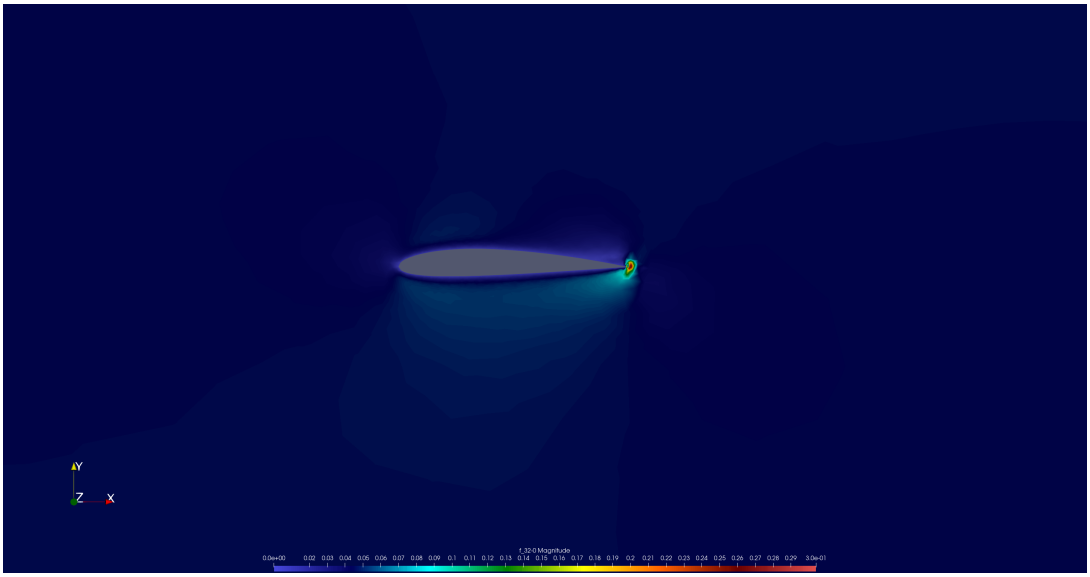

(c) $Re = 10^6$

Figure A.9: Standard deviation of velocity contour plot for a NACA 2412 airfoil

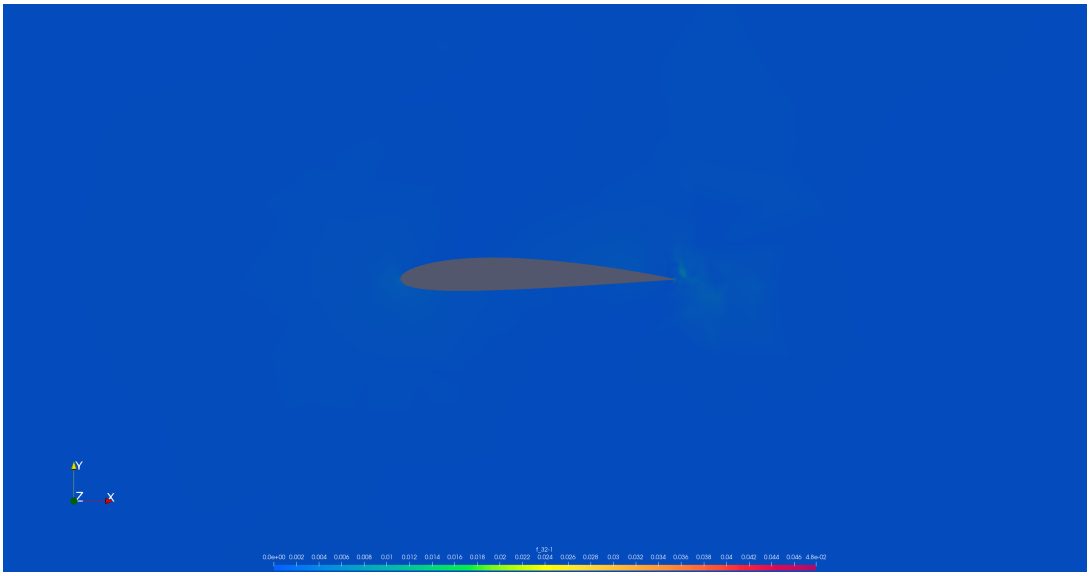

(a) $Re = 10^4$

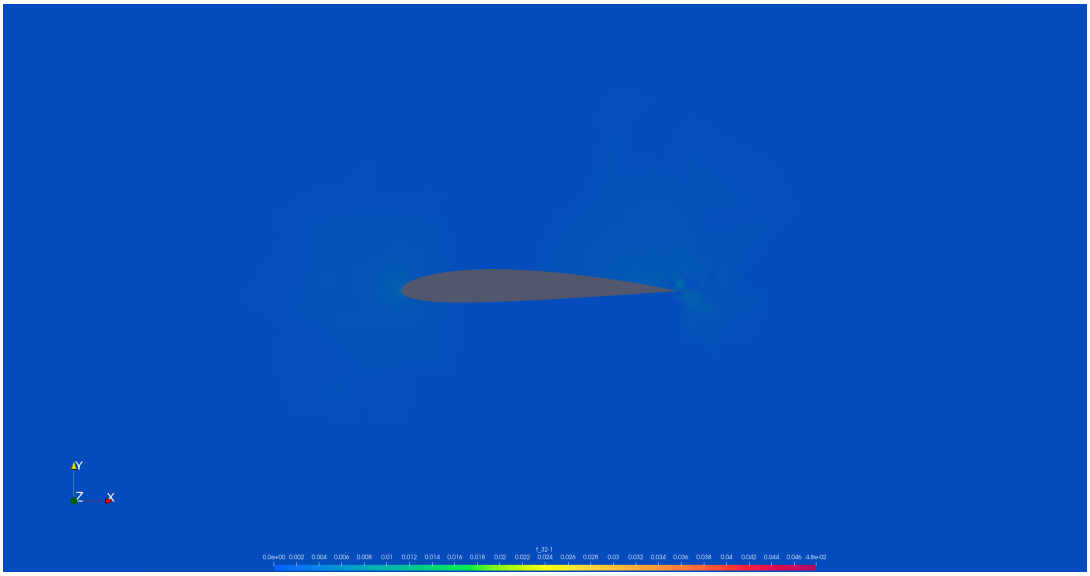

(b) $Re = 10^5$

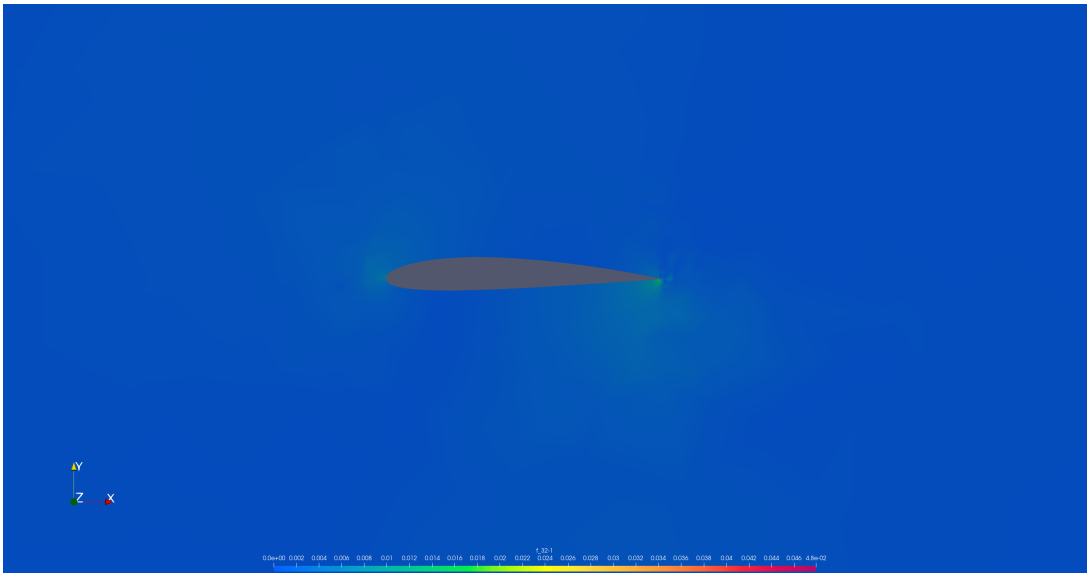

(c) $Re = 10^6$

Figure A.10: Standard deviation of pressure contour plot for a NACA 2412 airfoil

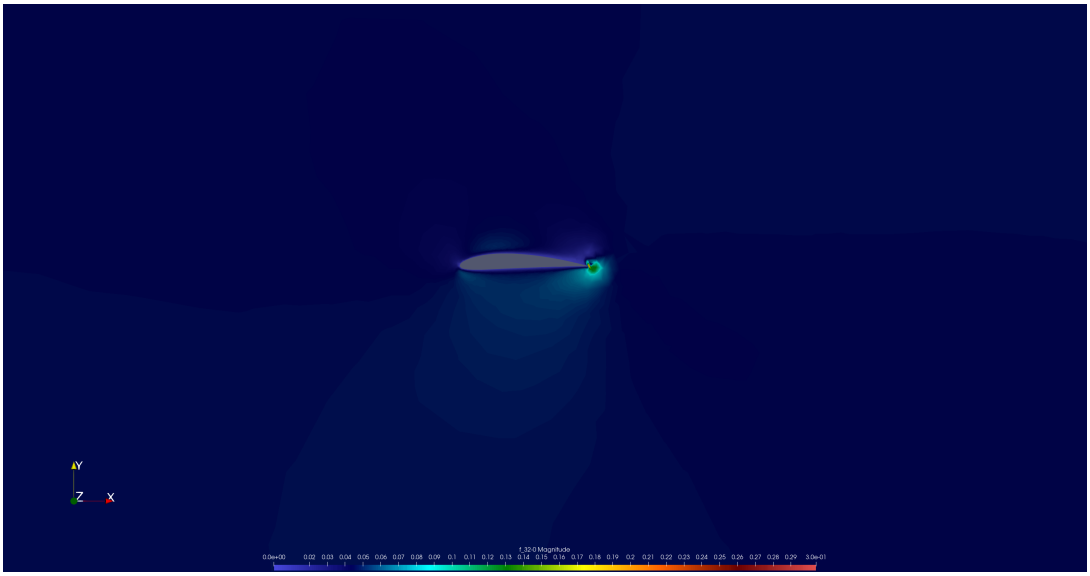

(a) $Re = 10^4$

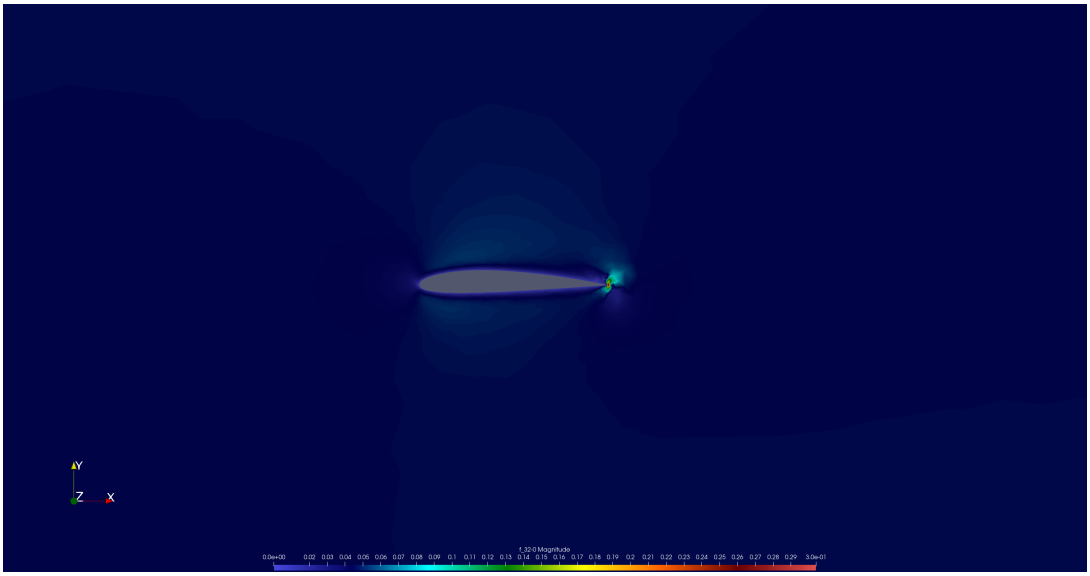

(b) $Re = 10^5$

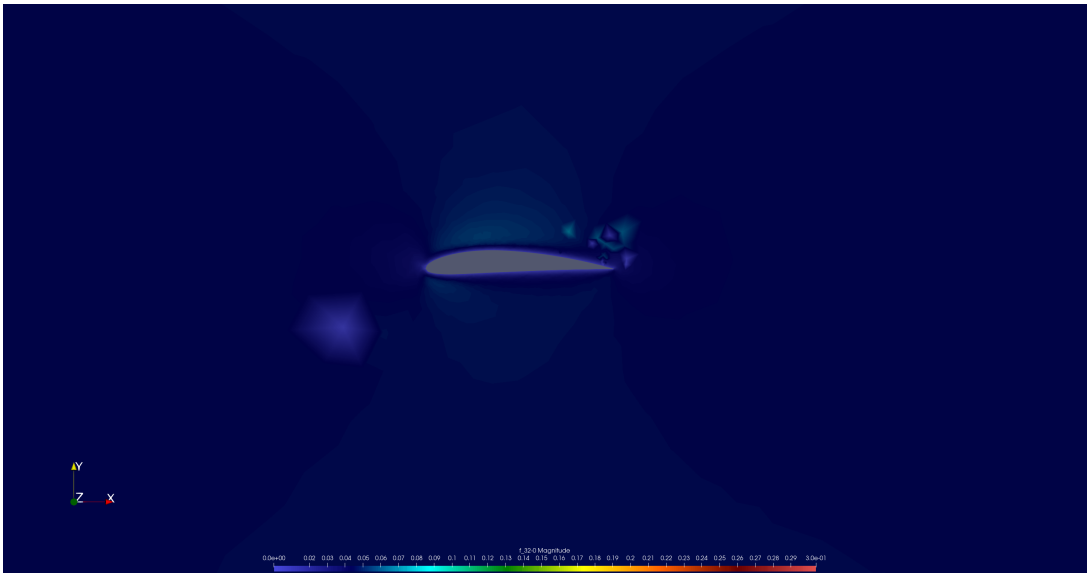

(c) $Re = 10^6$

Figure A.11: Standard deviation of velocity contour plot for a NACA 4412 airfoil

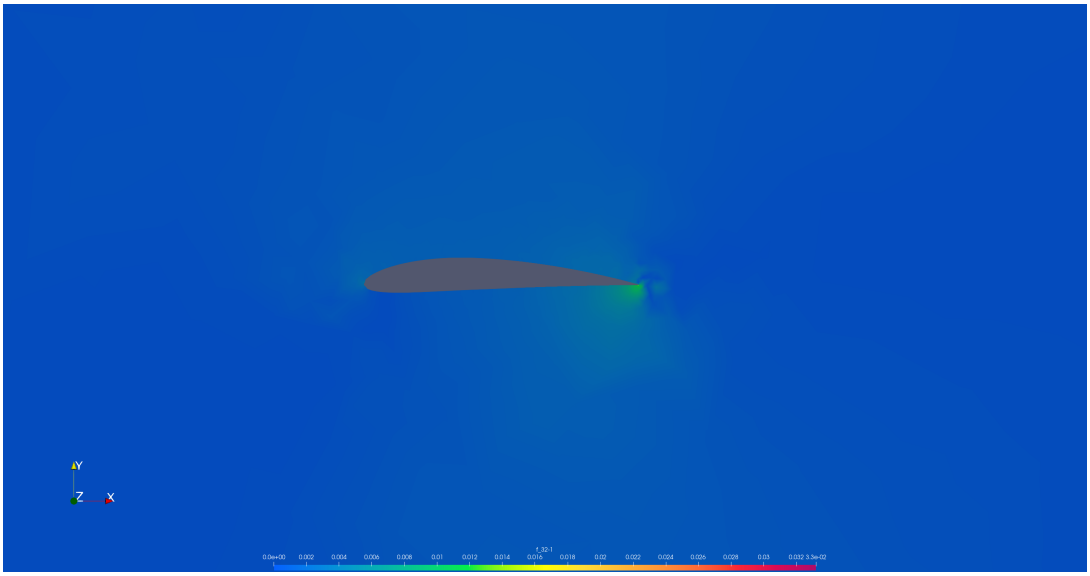

(a) $Re = 10^4$

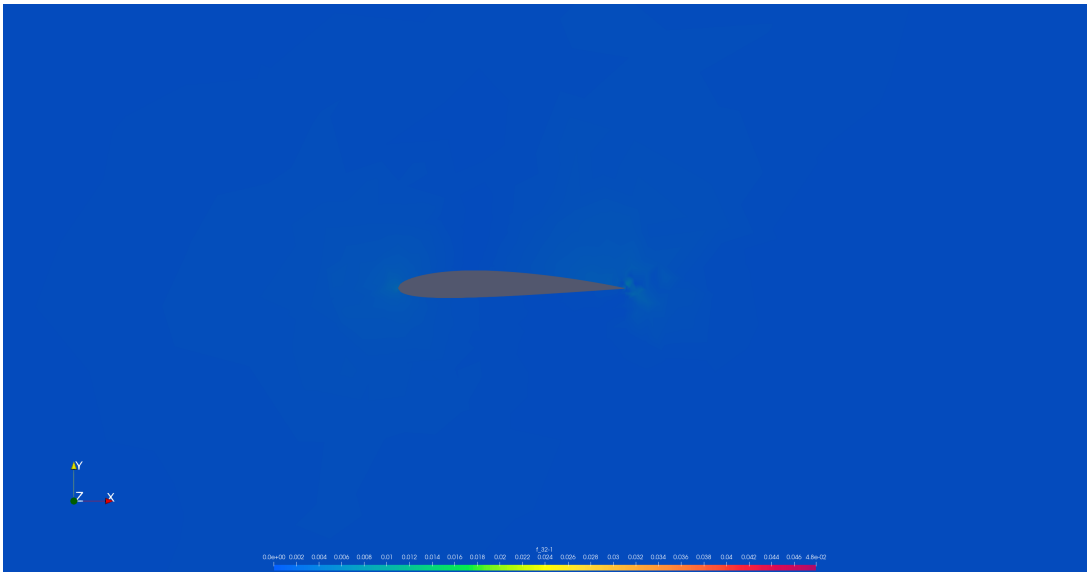

(b) $Re = 10^5$

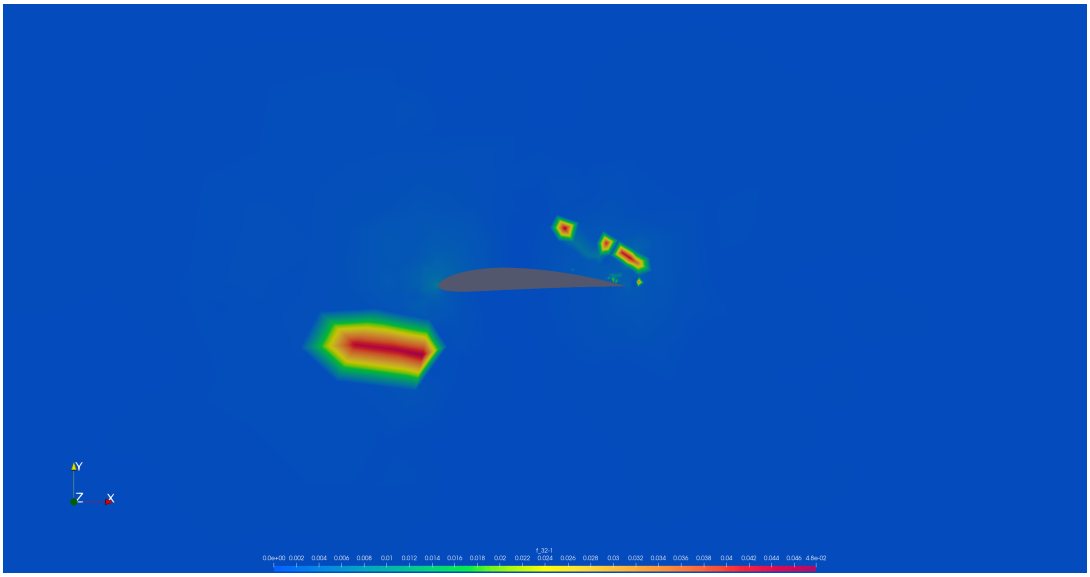

(c) $Re = 10^6$

Figure A.12: Standard deviation of pressure contour plot for a NACA 4412 airfoil